VILNIUS UNIVERSITY

VYTAUTAS BALEVIČIUS

QUANTUM COHERENCE IN MOLECULAR EXCITATION ENERGY TRANSFER AND RELAXATION

Doctoral dissertation

Physical sciences, physics (02P)

Vilnius, 2013

Doctoral dissertation was prepared at Vilnius University in 2009 – 2013, Vilnius, Lithuania

Scientific supervisor:
prof. habil. dr. Leonas Valkūnas (Vilnius University, Physical sciences, physics – 02P)

VILNIAUS UNIVERSITETAS

VYTAUTAS BALEVIČIUS

KVANTINIS KOHERENTIŠKUMAS MOLEKULIŲ SUŽADINIMO ENERGIJOS PERNAŠOS IR RELAKSACIJOS VYKSMUOSE

Daktaro disertacija

Fiziniai mokslai, fizika (02P)

Vilnius, 2013 metai

Disertacija rengta 2009 – 2013 metais Vilniaus universitete

Mokslinis vadovas:
prof. habil. dr. Leonas Valkūnas (Vilniaus universitetas, fiziniai mokslai, fizika – 02P)

Acknowledgments

I would like to thank a number of people, who were with me all these years and who directly or indirectly contributed to the work presented in this dissertation.

First of all, I would like to express my gratitude to my supervisor prof. Leonas Valkūnas, who brought me into this field, who shared his knowledge with great patience and care, and who gave a new meaning to the words "enthusiasm" and "optimism". I would also like to express my gratitude to prof. Tomáš Mančal, whose support and advice during my early steps in the theory of open quantum systems can hardly be overestimated, and who made my time spent in Prague unforgettable. I also wish to thank prof. Darius Abramavičius for valuable discussions and a fruitful collaboration. I am especially grateful to Vytautas Balevičius Sr. for being an example and for my discovery of Physics.

Many thanks go to the people in the Department of Theoretical Physics. I would like to thank all the fellow students in our group for all the helpfulness, assistance or simply great time, so big thanks to Andrius, Vytautas, Julius, Jevgenij, Sveta, Stepas. Thanks go with an apology to those, whom I have not mentioned personally.

Lastly, I would like to express my gratitude and love to all my family, who supported me in each and every way, especially my wife Eglė.

Vytautas Balevičius Jr.

Abbreviations and Common Notations

DOF – degrees of freedom

RDO – reduced density operator

ADO – auxiliary density operator

QME – Quantum Master Equation

FRET – Förster resonance energy transfer

HEOM – Hierarchical equations of motion

TR – thermal relaxation

RGS – relaxation to the ground state

Chl – chlorophyll

Car – carotenoid

Pc – phthalocyanine

PSII – photosystem II

NPQ – non-photochemical quenching

TRF – time-resolved fluorescence

2D PE – two-dimensional photon echo (spectroscopy)

EADS – evolution-associated decay spectra

Tr{} – trace operation

δ_{ij} – Kronecker delta

Re /Im – real / imaginary part

Contents

1 Introduction **9**

2 Quantum description of energy transfer in molecular aggregates **15**
2.1 The concept of Frenkel excitons 16
2.2 Coupling the excitons to the bath 19
2.3 Propagation of the density matrix 21
2.4 Density matrix in the modelling of spectroscopic experiments 31

3 Energy transfer in the weak resonance coupling limit **35**
3.1 Equations of motion in the weak coupling limit 35
3.2 Main features of the weak resonance coupling model 39
3.3 Time-resolved fluorescence in weakly coupled dimer 44

4 The intermediate resonance coupling regime **59**
4.1 Influence of the asymmetric reorganization energies on the excitation dynamics 59
4.2 Breakdown of the exciton concept 63
4.3 Optimal energy gap in the non-Markovian regime 65
4.4 Comparison of propagation schemes in the intermediate coupling regime 69

5 Relaxation to the ground state in an excitonic system **71**
5.1 Non-photochemical quenching in plant photosynthesis 71
5.2 Energy transfer and quenching in an excitonic heterodimer . 73
5.3 Carbonyl-linked carotenoid–phthalocyanine dyads 78
5.4 Phenylamino-linked carotenoid–phthalocyanine dyads 81

6 Summary of the results and conclusions **85**

Bibliography **86**

1. Introduction

The research of molecular complexes and aggregates has a long and rich history. It can be dated back to the 1930's, when Frenkel formulated the concept of a non-conductive electronic excitation, now known as the zero-radius or simply Frenkel exciton [1]. The excitonic features where soon discovered not only in molecular crystals, but also in highly concentrated solutions of pseudoisocyanine dye, which was the first example of molecules forming the so-called J-aggregates [2]. Today it is an active field that attracts a lot of attention from both experimentalists and theoreticians. The main reason for that is the extraordinary optical properties of molecular aggregates, which differ strongly from single molecules or pure crystals. The exciton theory of molecular complexes found a particularly important and fruitful application in describing the photosynthetic pigment–protein complexes [3, 4]. The boost in the field began with the precise molecular structure of photosynthetic aggregates, starting with the reaction centre of purple bacteria in 1984 [3]. The photosynthetic antennae of plants and bacteria involve only a limited number of different types of small molecules as building blocks. Nonetheless, the antenna aggregates appear in great variety, differing in the spectral and energy transfer properties. The variability is largely due to the influence of inter-chromophore interactions within these closely packed protein–chromophore complexes.

Excitation energy transfer, or exciton dynamics, is a very active area of the molecular aggregate research. The early attempts to describe the excitation transport was by Förster and Dexter in terms of the rate equations. The expression obtained by Förster in the 1940s [5] gave the the transfer rate in terms of intuitive concepts, such as the Coulomb coupling strength and the overlap of donor fluorescence spectrum with the absorption spectrum of the acceptor. It has successfully described the excitation dynamics in many cases. Moreover the Förster rate expression found various interesting applications, such as the "molecular ruler" for determining distances between chromophores. However, such an approach treats the exciton transport as an incoherent process, i.e., as a diffusive motion (also termed "hopping") of localized excitations. Such localized excitations are sometimes termed incoherent excitons. The given description is well justified under the condition of

weak inter-chromophore coupling, but in the opposite case we have a different physical picture. Namely, depending on the chromophore–bath coupling, an excitation can be shared by several or even all the chromophores within the aggregate. The excited state of the aggregate is a coherent superposition of the excited states of its constituents, and in terms of wave-functions, the excitation is delocalized. The degree of delocalization and the character of the coherent exciton transfer are largely determined by the coupling of the chromophores to the bath, e.g., the nuclear intra-molecular motion. The two extreme regimes can be identified by comparing the time scales of intramolecular relaxation and intermolecular transitions. In the case of strong coupling to the bath and fast intramolecular relaxation, the excitation is localized and the energy transfer is incoherent. Whereas in the opposite case, the excitation remains delocalized and the transfer is coherent.

Recent development of non-linear spectroscopies, such as the two-dimensional photon echo (2D PE) spectroscopy [6–9], triggered active studies of exciton coherence in photosynthetic pigment–protein complexes [10, 11]. 2D PE spectroscopy was a key tool demonstrating a complex pathway network of the energy transfer in the peripheral light-harvesting complexes from the purple bacteria, LH2 [12] and LH3 [13], also the long-lasting coherence in Fenna–Matthews–Olson (FMO) complexes [7, 14] and in LHCII, the major light-harvesting complex from photosystem II (PSII) of plants [15]. Recently the 2D PE spectra were also recorded for the photosynthetic reaction centres from bacteria [16] and for other molecular aggregates, for instance, polymer chains [17] or cylindrical (bi-tubular) J-aggregates [18]. Apart from the clear identification of exciton transfer between pigment molecules or their clusters, quantum coherence and population oscillations were also observed. All the new data gave rise to the currently active research area sometimes referred to as "quantum biology", which aims to evaluate the importance of coherence, entanglement and noise in the energy transport in biological molecular complexes [19–24].

Theoretical description of the exciton evolution in molecular aggregates is usually formulated in terms of perturbative dynamics. The peculiarity of such systems arises from the characteristic size which is intermediate between that of a single chromophore and a molecular crystal. One is no longer able to take the advantage of the periodicity and "rigidness" associated with the crystalline phase, nor the relative simplicity of a single molecule. Within the perturbative approach, the interaction of electronic excitations with intra- and inter-molecular vibrations causes a disruption of the phase relationship between the excited states of the molecules. Such

type of interaction makes a distinct influence on the coherence in the exciton dynamics and plays the dominant role in determining the exciton relaxation pathways. As pointed out earlier, the actual details of the excitation evolution depend on the competition between the inter-chromophore and the system–bath interactions. These two types of interaction are of similar order in photosynthetic aggregates, therefore the question of the applicability of some specific perturbative theory goes hand in hand with the study of a concrete system. For instance, the Redfield theory [25], which is a popular tool for the description of exciton dynamics in photosynthetic complexes, imposes a natural restriction for the possibility of obtaining the long-lasting coherent oscillations, as demonstrated for molecular dimers [26–28]. Regardless of the exact nature of the oscillations in 2D PE experiments, which is a topic of lively debate, the influence of quantum coherence in the energy flow within an excited molecular complex is an important question. This question is approached here by studying the simplest molecular aggregate — a molecular dimer — which is a good model system already displaying effects caused by the excitonic quantum coherence [29, 30].

Main goal and tasks of the research work

The **main goal** of this research work is to asses the influence of quantum coherence on the energy transfer in molecular complexes, concentrating on the hierarchy of the relaxation processes within a molecular dimer: vibrational relaxation, energy redistribution within the single exciton manifold and the relaxation to the ground state. In order to achieve this goal the following tasks are to be performed:

- Derive equations of motion for the reduced density operator and analytical expressions for the third-order response function in the limit of weak resonance inter-chromophore coupling.
- Investigate the excitation evolution, as a function of the asymmetry in model parameters, in an excitonic heterodimer in the intermediate inter-chromophore coupling and strong system–bath coupling regimes.
- Analyse the relaxation to the ground state in the resonantly coupled dimer in the coherent and incoherent regimes, when one of the constituent monomers has an intrinsically short excited state lifetime.

Novelty and relevance of the results

A molecular homodimer, which is a pair of resonantly coupled identical molecules, is the usual system to be employed for consideration of various aspects of the exciton dynamics and relaxation [27, 28, 31, 32]. In the case of a *hetero*dimer, the distinctness of the constituent monomers is often limited to excitation energies [11, 29]. Although some aspects which could be attributed to the heterodimer were also disclosed by analysing the mixing of excitons with charge-transfer states [33, 34], a systematic investigation of the asymmetry of the dimer parameters in various resonance interaction and system–bath coupling regimes employing various widely accepted methods have not been performed. Additionally, the derivation of equations of motion in the limit of weak resonance coupling and the expansion of the evolution operators in powers of the resonance coupling are novel techniques to study the coherent phenomena.

The obtained results and conclusions can be extended to larger systems since the excitonic dimer is the simplest system having all ingredients inherent in larger systems. It has to be emphasized that the photosynthetic molecular aggregates are often disordered assemblies of molecules and the exciton delocalization length is of the order of a few molecules. Thus, the excitonic properties of a dimer must be quite close to the realistic properties of photosynthetic excitons. Moreover, the heterodimers have been proposed as possible candidates for the quenching centres in the protective mechanism of energy dissipation during photosynthesis, know as the non-photochemical quenching (NPQ). The presented results provide insights into the possible role of a special pigment dimer in the NPQ and explain the experimental results in artificial dyad molecules [35–37].

Statements presented for the defence

1. The developed method of perturbative treatment of the resonance interaction, in the form of equations of motion and the direct calculation of time-resolved fluorescence, captures all significant excitonic effects while staying in the basis of monomeric states.

2. In the coherent excitation transfer regime, under certain combinations of reorganization energies, two excitonically coupled states can become energetically swapped with respect to the uncoupled ones, which is in stark contrast to the incoherent regime.

3. The unified treatment of incoherent and coherent regimes of energy transfer with relaxation to the ground state allows to demonstrate that in the asymptotic dynamics of excitonically mixed states no qualitatively new features arise. Although the formation of excitonic states is sometimes distinguished as a separate regime of excitation quenching, due to the exciton–phonon coupling the long-time evolution of the excitation is in principle equivalent to that within an incoherent donor–quencher system.

Author's contribution and approbation of the results

The author of this dissertation has derived all the analytical expressions in Sections 3.3 and 5.2, numerically implemented and performed calculations for Chapter 3, performed data analysis and formulated the final results in Chapters 4 and 5.

The results are presented in 5 scientific papers:

1. V. Balevičius Jr., D. Abramavicius, L. Valkunas. *Ultrafast time-resolved fluorescence in weakly coupled aggregates* (in preparation).

2. V. Balevičius Jr., L. Valkunas, D. Abramavicius. *Exciton dynamics in photosynthesis* Proceedings of the ICMAT 2013 symposium (in press).

3. V. Balevičius Jr., A. Gelzinis, D. Abramavicius, L. Valkunas. *Excitation energy transfer and quenching in a heterodimer: applications to the carotenoid–phthalocyanine dyads* J. Phys. Chem. B **117**, 11031–11041 (2013).

4. V. Balevičius Jr., A. Gelzinis, D. Abramavicius, T. Mančal, L. Valkunas. *Excitation dynamics and relaxation in a molecular heterodimer* Chem. Phys. **404**, 94–120 (2012).

5. T. Mančal, V. Balevičius Jr., L. Valkunas. *Decoherence in weakly coupled excitonic complexes* J. Phys. Chem. A **115**, 3845–3858 (2011).

The results have been presented at the conferences:

1. V. Balevičius (jaun.), D. Abramavicius, L. Valkunas (2013). "Laikinės skyros fluorescencijos spektroskopija silpnos rezonansinės sąveikos artiniu" 40-osios Lietuvos nacionalinės fizikos konferencijos programa ir pranešimų tezės, p. 220. Vilnius.

2. V. Balevičius Jr., A. Gelzinis, D. Abramavicius, L. Valkunas (2012). "Excitation energy transfer and quenching in phthalocyanine-carotenoid dyads" Abstracts of Vilnius Workshop on Non-Linear Spectroscopy and Open Quantum Systems, p. 12 Vilnius.

3. V. Balevičius Jr., A. Gelzinis, D. Abramavicius, L. Valkunas (2012). "Excitonic dimer as a quenching centre in photosynthetic pigment-protein complexes" Abstracts of the tenth International Conference on Excitonic Processes in Condensed Matter, Nanostructured and Molecular Materials, p. 28. Groningen.

4. V. Balevičius Jr., A. Gelzinis, D. Abramavicius, T. Mančal, L. Valkunas (2011). "Exciton Dynamics and Relaxation in Heterodimer" Abstracts of Vilnius Workshop on Non-Linear Spectroscopy and Open Quantum Systems, p. 9. Vilnius.

5. V. Balevičius (jaun.), A. Gelžinis, D. Abramavičius, L. Valkūnas (2011). "Eksitonų dinamika ir relaksacija heterodimere" 39-osios Lietuvos nacionalinės fizikos konferencijos programa ir pranešimų tezės, p. 220. Vilnius.

6. V. Balevičius Jr., A. Gelzinis, D. Abramavicius, L. Valkunas (2011). "Exciton Dynamics and Relaxation in a Heterodimer" Abstracts of the 12th International Conference on Electronic and Related Properties of Organic Systems, p. 77. Vilnius.

7. V. Balevičius Jr., T. Mančal and L. Valkunas (2010). "Decoherence in Weakly Coupled Excitonic Complexes" Abstracts of the 14th International Symposium on Ultrafast Phenomena in Semiconductors, p. 29. Vilnius.

2. Quantum description of energy transfer in molecular aggregates

In this chapter the theoretical concepts and models used throughout the dissertation are reviewed. At the heart of this overview is the density operator theory, which is one of the most elaborated ways to treat the non-stationary dissipative dynamics of open quantum systems. In principle, one could also solve the Schrödinger equation in a larger Hilbert space by including the environment degrees of freedom (DOF), or use the stochastic Schrödinger equations like the Haken–Strobl model [4]. However, the density operator (matrix in a specific representation) characterizes state populations (diagonal elements of the matrix) and interstate phase relations — coherences (off-diagonal elements of the matrix) in a unified way and, thus, makes a direct relation with the dynamics of observables. The dynamics of the joint system–environment density operator $\hat{W}$ are governed by the *quantum Liouville equation* (or *von Neuman equation*):

$$\frac{\mathrm{d}}{\mathrm{d}t}\hat{W} = -\mathrm{i}\left[\hat{H}, \hat{W}\right]. \tag{2.1}$$

Here and in the following, we take $\hbar = 1$, so that energy and frequency are used equivalently.

In the total Hamiltonian we distinguish three terms:

$$\hat{H} = \hat{H}_{\mathrm{S}} + \hat{H}_{\mathrm{B}} + \hat{H}_{\mathrm{SB}}. \tag{2.2}$$

The system (first term) is directly observable and is described by the Frenkel exciton Hamiltonian. The system is in contact with the environment that constitutes a thermal bath (second term), which is not directly observed and is considered to be in the thermal equilibrium. The system–bath coupling is represented by $\hat{H}_{\mathrm{SB}}$, which is a system operator parametrically dependent on the bath coordinates. In the following, we discuss each term of the total Hamiltonian, Eq. 2.2, the strategies of dealing with the Liouville equation, Eq. 2.1, and the connection between the density matrix and spectroscopic experiments.

2.1. The concept of Frenkel excitons

The quantum-mechanical description of molecules and their complexes embedded in various environments, e.g., solvents or matrices, is the starting point in molecular aggregate theory. Solving the stationary Schrödinger equation directly would pose an insoluble problem because of the large number of all the stationary states relevant to such a composite system. Thus, let us consider molecular aggregates consisting of electronically neutral molecules interacting with each other through electrostatic dipole–dipole type couplings, which are weak compared to the molecular excitation energies; in this limit we assume that we can solve the Schrödinger equation of the isolated molecules.

The general Hamiltonian for the aggregate of N molecules in the Born–Oppenheimer approximation is given by

$$\begin{aligned}\hat{H}_{\mathrm{agg}}(R) &= \sum_{i}^{N}\sum_{\alpha}^{M}\left(\frac{\hat{\boldsymbol{p}}_{i\alpha}^{2}}{2m}+\sum_{k}^{K}V\left(\hat{\boldsymbol{x}}_{i\alpha},\boldsymbol{R}_{ik}\right)\right)\\ &\quad+\frac{1}{2}\sum_{i\neq j}^{N}\sum_{\alpha\beta}^{M}\frac{\eta}{|\hat{\boldsymbol{x}}_{i\alpha}-\hat{\boldsymbol{x}}_{j\beta}|}+\sum_{i\neq j}^{N}\sum_{\alpha k}^{K}\frac{\eta Z_{k}}{|\hat{\boldsymbol{x}}_{i\alpha}-\boldsymbol{R}_{jk}|},\end{aligned}\tag{2.3}$$

where the indices i and j label different molecules, α and β — different electrons and k — nuclei. There are M electrons and K nuclei in each molecule. $\hat{\boldsymbol{x}}_{i\alpha}$ and $\hat{\boldsymbol{p}}_{i\alpha}$ denote the coordinate and momentum operators of the α-th electron of the i-th molecule, $\boldsymbol{R}_{ik}$ is the position of the k-th nucleus. The other parameters are the charge of the k-th nucleus, Z_k, and $\eta{=}e^2\left(4\pi\epsilon\epsilon_0\right)^{-1}$. The first double sum in the Hamiltonian denotes molecules isolated from each other, while the remaining two terms denote the inter-molecular interactions. Note that the nuclear coordinates in this Hamiltonian are parameters, thus, the molecular geometry is assumed to be known.

Since an optical excitation is resonant with one particular electronic transition, we are not interested in the whole spectrum of each molecule but only in the characteristics of two electronic states — the electronic ground and excited states. Let us denote the corresponding state vectors of the j-th molecule by $|\psi_j^{(g)}\rangle$ and $|\psi_j^{(e)}\rangle$, accordingly. These vectors are taken as the basis set for the problem formulation: the state vector of an aggregate is constructed as a direct product of sate vectors of the isolated molecules

(the Heitler–London approximation):

$$|g\rangle = \prod_{j}^{N} |\psi_j^{(g)}\rangle \tag{2.4}$$

for the ground state and

$$|i\rangle = |\psi_i^{(e)}\rangle \prod_{j\neq i}^{N} |\psi_j^{(g)}\rangle \tag{2.5}$$

for the excited state.

In the space of single- and double-excitations — the so-called site representation — the Frenkel exciton Hamiltonian for an aggregate, the system Hamiltonian in the current case, is given by

$$\hat{H}_{\mathrm{S}} = \sum_{i}^{N} \varepsilon_i |i\rangle\langle i| + \sum_{i\neq j}^{N} J_{ij} |i\rangle\langle j|, \tag{2.6}$$

where

$$\varepsilon_i = \varepsilon_i^0 + \eta \sum_{j\neq i}^{N} \int \mathrm{d}\boldsymbol{r}_1 \int \mathrm{d}\boldsymbol{r}_2 \frac{\left[\rho_i^{(ee)}(\boldsymbol{r}_1) - \rho_i^{(gg)}(\boldsymbol{r}_1)\right] \rho_j^{(gg)}(\boldsymbol{r}_2)}{|\boldsymbol{r}_1 - \boldsymbol{r}_2|} \tag{2.7}$$

is the transition energy of a molecular excitation in the presence of other molecules in their ground states. The parameters are as follows: ε_i^0 is the transition energy of the molecule isolated from the rest of the aggregate, $\rho_i^{(gg)}(\boldsymbol{r})$ is the total charge density of the i-th molecule in its ground state and $\rho_i^{(ee)}(\boldsymbol{r})$ is the charge density of the electronic excited state of the i-th molecule. For neutral molecules we have

$$\int \mathrm{d}\boldsymbol{r} \rho_i^{(ss)}(\boldsymbol{r}) = 0, \tag{2.8}$$

where (ss) is either (gg) or (ee). The inter-molecular coupling

$$J_{ij} = \eta \int \mathrm{d}\boldsymbol{r}_1 \int \mathrm{d}\boldsymbol{r}_2 \frac{\rho_i^{(eg)}(\boldsymbol{r}_1) \rho_j^{(eg)}(\boldsymbol{r}_2)}{|\boldsymbol{r}_1 - \boldsymbol{r}_2|} \tag{2.9}$$

is the Coulomb interaction between transition charge densities $\rho_i^{(eg)}(\boldsymbol{r})$ [38].

When intermolecular distances are larger than the molecular dimensions, a dipole approximation for charge densities is often assumed [4]. It approx-

imately represents all charge densities by simple dipole vectors: transition dipoles $\boldsymbol{\mu}_{ig}$ represent the transition charge densities $\rho_i^{(eg)}(\boldsymbol{r})$ and permanent dipoles $\boldsymbol{d}_i$ represent the difference densities $\left(\rho_i^{(ee)}(\boldsymbol{r}) - \rho_i^{(gg)}(\boldsymbol{r})\right)$. The dipole vectors can be obtained from charge densities by calculating their first moments. Alternatively, they are given by the dipole operator expectation values: $\boldsymbol{\mu}_{ig} = \langle i|\hat{\boldsymbol{\mu}}|g\rangle$ and $\boldsymbol{d}_i = \langle i|\hat{\boldsymbol{\mu}}|i\rangle - \langle g|\hat{\boldsymbol{\mu}}|g\rangle$; they are both given in terms of the dipole operator in the coordinate representation

$$\hat{\boldsymbol{\mu}} = \sum_{m\alpha} q_{m\alpha} \left(\hat{\boldsymbol{x}}_{m\alpha} - \boldsymbol{R}_m\right), \tag{2.10}$$

where the sum is over all charges α of the molecule m, denoted by $q_{\alpha m}$; $\boldsymbol{R}_m$ is the molecular centre. Under these condition we obtain the dipole–dipole coupling expression:

$$J_{ij} = \frac{1}{4\pi\epsilon\epsilon_0} \left(\frac{(\boldsymbol{\mu}_{ig} \cdot \boldsymbol{\mu}_{jg})}{|\boldsymbol{R}_{ij}|^3} - 3\frac{(\boldsymbol{R}_{ij} \cdot \boldsymbol{\mu}_{ig})(\boldsymbol{R}_{ij} \cdot \boldsymbol{\mu}_{jg})}{|\boldsymbol{R}_{ij}|^5} \right). \tag{2.11}$$

According to the Heitler–London approximation, an aggregate containing N chromophores has a single ground state and N singly-excited states. Additionally, there are $N(N-1)/2$ doubly-excited states, however, they are disregarded in this dissertation, although they should be taken into account if certain experimental techniques, such as the 2D PE, are considered. The exciton eigenstate properties are obtained by diagonalizing the Hamiltonian defined by Eq. (2.6). The N single-excitons $|\alpha\rangle$ are related to the molecular excitations $|i\rangle$ by a unitary transformation matrix S:

$$|\alpha\rangle = \sum_{i}^{N} S_{\alpha i}^{\dagger} |i\rangle. \tag{2.12}$$

Here and further, the Latin indices are reserved for the electronic (site) states, while the Greek indices denote the excitonic states. The exciton energies (eigenvalues) ε_α form a diagonal matrix:

$$\varepsilon = S^{\dagger} h S, \tag{2.13}$$

where $h_{ij} = J_{ij} + \delta_{ij}\varepsilon_i$ and δ_{ij} is the Kronecker delta. The exciton states defined this way determine the basic properties of a molecular aggregate. The relation between the site and the excitonic representations is shown graphically in Fig. 2.1.

A special case of molecular aggregates is a molecular dimer. From the

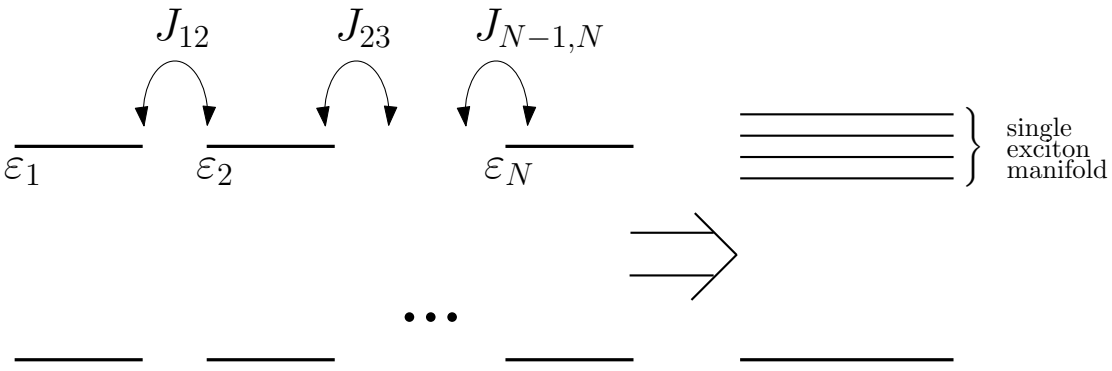

Figure 2.1 Assembly of interacting chromophores in the site and the excitonic representations.

theoretical point of view, a dimer is an interesting object because it is the simplest system, where the excitonic effects can be observed and studied. The simplicity allows us to obtain the analytical expression for the transformation matrix S, which reads

$$S = \begin{pmatrix} \cos\theta & -\sin\theta \\ \sin\theta & \cos\theta \end{pmatrix}, \tag{2.14}$$

where the so-called mixing angle is defined as

$$\theta \equiv \frac{1}{2}\arctan\frac{2J_{12}}{\varepsilon_1 - \varepsilon_2} \tag{2.15}$$

and has values $\theta \in [-\pi/4; \pi/4]$. The mixing angle describes the degree of delocalization of excitation over the monomeric states.

2.2. Coupling the excitons to the bath

In the realistic molecular aggregate the electronic DOF are coupled to the nuclear DOF constituting the environment. The latter include both the intramolecular vibrational DOF and the intermolecular ones, e.g., the fluctuations of the protein scaffold in the case of light-harvesting complexes. The coupling of the system DOF to the environmental ones induces damping and relaxation. To include this effect we additionally couple the aggregate to the harmonic bath. The Hamiltonians of the bath and the system–bath interaction are then given respectively by [39]:

$$\hat{H}_{\mathrm{B}} = \hat{T}(\hat{p}) + \hat{V}_g(\hat{q}), \tag{2.16}$$

$$\hat{H}_{\mathrm{SB}} = \sum_{i}^{N} \hat{Q}_i \Delta\hat{V}_i(\hat{q}). \tag{2.17}$$

Operators $\hat{T}(\hat{p})$ and $\hat{V}_i(\hat{q})$ denote the kinetic energy of the nuclei and the nuclear potential energy surface of the i-th site, accordingly, $\hat{p}$ and $\hat{q}$ are the generalized momenta and coordinates of the bath. $\hat{Q}_i = |i\rangle\langle i|$ is the projector onto the i-th site. The energy gap operator given by

$$\Delta\hat{V}_i(\hat{q}) = \hat{V}_i(\hat{q}) - \hat{V}_g(\hat{q}) - \langle \hat{V}_i(\hat{q}) - \hat{V}_g(\hat{q})\rangle_{\mathrm{eq}} \tag{2.18}$$

describes the thermal fluctuations of the energy gap between the ground and the excited state potential energy surfaces. The angular brackets $\langle \ldots \rangle_{\mathrm{eq}}$ denote the averaging over the equilibrium bath. In this notation we define the reorganization energy as

$$\lambda_i = \langle \hat{V}_i(\hat{q}) - \hat{V}_g(\hat{q})\rangle_{\mathrm{eq}}, \tag{2.19}$$

which is a twofold parameter. On the one hand, the reorganization energy renormalizes the transition energies of the bare system as

$$\hat{H}_{\mathrm{S}} = \sum_{i}^{N} (\varepsilon_i^0 + \lambda_i)|i\rangle\langle i| + \sum_{i\neq j}^{N} J_{ij}|i\rangle\langle j|, \tag{2.20}$$

and, thus, defines the Stokes shift. On the other hand, it describes the system–bath coupling strength.

In terms of the DOF the bath is usually considered to be much larger than the system, thus, it is described using thermodynamical or statistical concepts, and its thermodynamic state is not affected by the system. The main characteristic of the bath is the temperature $k_{\mathrm{B}}T \equiv \beta^{-1}$, where k_{B} is the Boltzmann constant. According to statistical physics the bath at a fixed temperature performs equilibrium fluctuations, which in turn induce the fluctuations of chromophore transition energies, conf. Eq. (2.17). These fluctuations can be characterized by the correlation functions of the bath:

$$C_{ij}(t) = \langle \Delta\hat{V}_i(t)\Delta\hat{V}_j(0)\rangle_{\mathrm{eq}}, \tag{2.21}$$

were, $\Delta\hat{V}_i(t)$ is the energy gap operator in the interaction picture: $\Delta\hat{V}_i(t) = \mathrm{e}^{\mathrm{i}\hat{H}_{\mathrm{B}}t}\Delta\hat{V}_i(\hat{q})\mathrm{e}^{-\mathrm{i}\hat{H}_{\mathrm{B}}t}$. These functions fully determine the effect of the bath on the system.

In practice a correlation function is usually obtained from the spectral

density of the bath $C''_{ij}(\omega)$, which is the odd part of the Fourier transform of the correlation function. Due to the fluctuation–dissipation relation [40] the correlation function can then be given by

$$C_{ij}(t) = \int_{-\infty}^{\infty} \frac{\mathrm{d}\omega}{2\pi} C''_{ij}(\omega) \left[\cos(\omega t)\coth(\beta\omega/2) - \mathrm{i}\sin(\omega t)\right], \tag{2.22}$$

or

$$C_{ij}(t) = \frac{1}{\pi}\int_{-\infty}^{\infty} \mathrm{d}\omega \mathrm{e}^{-\mathrm{i}\omega t}\frac{1}{1-\mathrm{e}^{-\beta\omega}} C''_{ij}(\omega). \tag{2.23}$$

The advantage of the spectral density is that it can be determined directly from fluorescence line-narrowing measurements [41,42] or molecular dynamics simulations [43], and it does not depend on temperature and therefore encompasses the spectral content of the bath alone.

It is usually assumed that the bath modes at different sites are not correlated, $C''_{ij}(\omega) = \delta_{ij} C''_i(\omega)$, and some specific model for the spectral density is used. Throughout this dissertation the overdamped Brownian oscillator spectral density [40, 44] is employed:

$$C''_i(\omega) = 2\lambda_i \frac{\omega\gamma_i}{\omega^2 + \gamma_i^2}, \tag{2.24}$$

where the parameter γ_i^{-1} corresponds to the correlation time of the i-th monomer site energy fluctuations.

2.3. Propagation of the density matrix

We start by looking at the quantum Liouville equation, Eq. (2.1), in the Liouville space [40], where all $N \times N$ operator matrices become $N \times N$ length vectors and operations on these vectors are denoted by superoperators. The Liouville superoperator (the Liouvillian) is defined as

$$\mathcal{L}\hat{W} \Leftrightarrow \left[\hat{H}, \hat{W}\right], \tag{2.25}$$

hence, we rewrite Eq. (2.1) as

$$\frac{\mathrm{d}}{\mathrm{d}t}\hat{W} = -\mathrm{i}\mathcal{L}\hat{W}. \tag{2.26}$$

The solution of Eq. (2.26) can formally be written as

$$\hat{W}(t) = \mathcal{U}(t_0, t)\hat{W}(t_0) \tag{2.27}$$

where we introduce the evolution superoperator (the Liouville space Green's function) $\mathcal{U}(t_0, t)$. For a time-independent Liouvillian it reads

$$\mathcal{U}(t_0, t) = \exp(-\mathrm{i}\mathcal{L}(t - t_0)). \tag{2.28}$$

However, in physically relevant situations, such as an aggregate perturbed by its environment and/or by the probing electromagnetic fields, the solution for $\mathcal{U}(t_0, t)$ is too difficult or impossible. In that case we partition the Liouvillian $\mathcal{L}$ into the reference and the perturbation parts as

$$\mathcal{L} = \mathcal{L}_0 + \mathcal{L}'. \tag{2.29}$$

The reference part is usually simpler than the total Liouvillian and results in an evolution $\mathcal{U}_0(t_0, t)$, given by

$$\mathcal{U}_0(t_0, t) = \exp(-\mathrm{i}\mathcal{L}_0(t - t_0)), \tag{2.30}$$

which can be calculated exactly. We next introduce the interaction picture using this evolution superoperator

$$\hat{W}_\mathrm{I}(t) = \mathcal{U}_0^\dagger(t_0, t)\hat{W}(t). \tag{2.31}$$

In the interaction picture we can write down the equation of motion that describes only the dynamics generated by the perturbation part:

$$\frac{\mathrm{d}}{\mathrm{d}t}\hat{W}_\mathrm{I}(t) = -\mathrm{i}\mathcal{L}'_\mathrm{I}(t)\hat{W}_\mathrm{I}(t), \tag{2.32}$$

where we define the perturbation term in the interaction representation

$$\mathcal{L}'_\mathrm{I}(t) = \mathcal{U}_0^\dagger(t_0, t)\mathcal{L}'\mathcal{U}_0(t_0, t). \tag{2.33}$$

Note that $\mathcal{L}'$ might be explicitly time dependent, hence the time dependence of $\mathcal{L}'_\mathrm{I}(t)$ comes from both the original time dependence (if present), and the transformation to the interaction picture.

The solution of Eq. (2.32) is given by

$$\hat{W}_\mathrm{I}(t) = \mathcal{U}_\mathrm{I}(t_0, t)\hat{W}_\mathrm{I}(t_0), \tag{2.34}$$

where the evolution superoperator in the interaction picture reads

$$\mathcal{U}_{\mathrm{I}}(t_0,t) = \exp_+\left(-\mathrm{i}\int_{t_0}^{t}\mathrm{d}\tau\mathcal{L}'_{\mathrm{I}}(\tau)\right), \tag{2.35}$$

as can be demonstrated by the iterative solution of Eq. (2.32). Here, we have introduced the time ordered exponential $\exp_+$, defined by

$$\exp_+\left(-\mathrm{i}\int_{t_0}^{t}\mathrm{d}\tau\mathcal{L}'_{\mathrm{I}}(t)\right) \equiv 1+\sum_{n=1}^{\infty}(-\mathrm{i})^n\int_{t_0}^{t}\mathrm{d}\tau_n\int_{t_0}^{\tau_n}\mathrm{d}\tau_{n-1}\ldots \times\int_{t_0}^{\tau_2}\mathrm{d}\tau_1\mathcal{L}'_{\mathrm{I}}(\tau_n)\mathcal{L}'_{\mathrm{I}}(\tau_{n-1})\ldots\mathcal{L}'_{\mathrm{I}}(\tau_1). \tag{2.36}$$

Comparing Eq. (2.31) with Eq. (2.34) and bearing in mind that $\hat{W}_{\mathrm{I}}(t_0) = \hat{W}(t_0)$, we conclude, that the full evolution superoperator can be partitioned as

$$\mathcal{U}(t_0,t) = \mathcal{U}_0(t_0,t)\mathcal{U}_{\mathrm{I}}(t_0,t). \tag{2.37}$$

The quantum Liouville equation, Eq. (2.1), is not being solved for the full density operator $\hat{W}$ as given, since we are usually interested only in a limited number of DOF rather than the full density operator. Those few DOF that constitute the observable system are called relevant, while others that affect the system, but are not directly observed, are in this sense called irrelevant. To describe the relevant DOF the *reduced density operator* (RDO) of the system is introduced as

$$\hat{\rho} = \mathrm{Tr}_{\mathrm{B}}\left\{\hat{W}\right\}, \tag{2.38}$$

where $\mathrm{Tr}_{\mathrm{B}}\{\}$ denotes the trace over the bath (irrelevant) DOF.

In order to obtain the time evolution of the RDO, we need to generate a closed set of equations in the state space of the relevant system. Several methods are used in this dissertation. The most straightforward method to describe the density matrix dynamics is the FRET theory for weakly coupled chromophores. In this case, a rate equation for the populations of the RDO in the site representation is given, which describes the incoherent hopping of localized excitation from one chromophore to another. In the case of strong interchromophore interactions, the coherent exciton transfer must be described by including the coherence dynamics, i.e., the evolution of phase relationships between different states. An example could be the well known *Quantum Master Equation* (QME), including the deriv-

ative forms, such as the multilevel Redfield equations [25]. Alternatively, *Hierarchical equations of motion* (HEOM) have been presented as an exact non-perturbative theory, which interpolates between the two regimes described above [29, 45, 46].

Förster theory for energy transfer

The probability of finding molecule i in its excited state at time t is given by the corresponding diagonal element of the density matrix, the population, in the site representation: $\rho_{ii}(t)$. Under the conditions that apply to the FRET theory, the population evolution is given by the rate equations:

$$\frac{\mathrm{d}}{\mathrm{d}t}\rho_{ii}(t) = -\sum_{j\neq i} k_{ij}\rho_{ii}(t) + \sum_{j\neq i} k_{ji}\rho_{jj}(t), \tag{2.39}$$

where k_{ij} are the rates of the excitation transfer from the molecule i to the molecule j. According to FRET, the rates are given by the expression

$$k_{ij} = \frac{|J_{ij}|^2}{2\pi}\int_{-\infty}^{\infty} \mathrm{d}\omega \tilde{F}_i(\omega)\tilde{A}_j(\omega), \tag{2.40}$$

where $\tilde{F}_i(\omega)$ and $\tilde{A}_j(\omega)$ are the fluorescence and absorption profiles of molecule i (in FRET terms, the donor) and molecule j (the acceptor), accordingly. Tilde denotes the Fourier transform, and the profile functions in the time domain read:

$$\begin{cases} F_i(t) = & \exp\left(-\mathrm{i}(\varepsilon_i^0 - \lambda_i)t - g_i^*(t)\right), \\ A_j(t) = & \exp\left(-\mathrm{i}(\varepsilon_j^0 + \lambda_j)t - g_j(t)\right); \end{cases} \tag{2.41}$$

here, $g(t)$ is the so-called line shape function [40] defined as

$$g_i(t) = \int_0^t \mathrm{d}t_1 \int_0^{t_1} \mathrm{d}t_2 C_i(t_2), \tag{2.42}$$

and $C_i(t)$ is the energy gap correlation function of the monomer, Eq. (2.21). Here, we have neglected the cross-correlations, i.e., assumed $C_{ij}(t) = \delta_{ij}C_i(t)$.

Quantum Master Equation

In the case of strong excitonic coupling, we need a description of exciton dynamics, which treats both the populations and the coherences on equal grounding. Such a description can be obtained by carrying out a perturbation theory with respect to the system–bath interaction. One of the results

of such an approach is the QME. Here, the outline of the derivation of the equations is given in greater detail, because the equations of motion for the RDO presented in the following chapter are derived in close analogy to the derivation of QME.

Following Eq. (2.29), we split the total Liouvillian into the reference and the interaction parts as

$$\mathcal{L} = \mathcal{L}_0 + \mathcal{L}_{\mathrm{SB}}. \tag{2.43}$$

The free evolution is described by the first term $\mathcal{L}_0\hat{W} \Leftrightarrow \left[\hat{H}_{\mathrm{S}} + \hat{H}_{\mathrm{B}}(\hat{p},\hat{q}), \hat{W}\right]$, and is given by the free-evolution superoperator $\mathcal{U}_0(t_0,t)$, Eq. (2.30),which is time-reversible due to the block-diagonal structure of the Hamiltonians comprising the free-evolution Liouvillian,

$$\mathcal{U}_0(t_0,t)\mathcal{U}_0(t_0,-t) = \mathcal{U}_0(t_0,t)\mathcal{U}_0^{\dagger}(t_0,t) = \mathcal{I}, \tag{2.44}$$

where $\mathcal{I}$ is the identity (super)operator.

The equation of motion in the interaction picture then reads:

$$\frac{\mathrm{d}}{\mathrm{d}t}\hat{W}_{\mathrm{I}}(t) = -\mathrm{i}\mathcal{L}_{\mathrm{SB}}(t)\hat{W}_{\mathrm{I}}(t), \tag{2.45}$$

where the system–bath interaction Liouvillian $\mathcal{L}_{\mathrm{SB}}\hat{W} \Leftrightarrow \left[\hat{H}_{\mathrm{SB}}(\hat{q}), \hat{W}\right]$ is given in the interaction picture with respect to $\mathcal{L}_0$ by

$$\mathcal{L}_{\mathrm{SB}}(t) = \mathcal{U}_0^{\dagger}(t_0,t)\mathcal{L}_{\mathrm{SB}}\mathcal{U}_0(t_0,t). \tag{2.46}$$

We derive an approximate closed equation for the RDO by applying the projection operator technique [9, 39] to Eq. (2.45). Let us consider an operator $\mathcal{P}^2 = \mathcal{P}$ and its orthogonal complement $\mathcal{Q} = \mathcal{I} - \mathcal{P}$ acting on the full density operator $\hat{W}$, separating it into the relevant and irrelevant parts accordingly: $\mathcal{P}\hat{W}$, $\mathcal{Q}\hat{W}$. Using the identity $\hat{W}_{\mathrm{I}}(t) = \mathcal{P}\hat{W}_{\mathrm{I}}(t) + \mathcal{Q}\hat{W}_{\mathrm{I}}(t)$ we can split the Eq. (2.45) into two coupled equations. The first one reads:

$$\frac{\mathrm{d}}{\mathrm{d}t}\mathcal{P}\hat{W}_{\mathrm{I}}(t) = -\mathrm{i}\mathcal{P}\mathcal{L}_{\mathrm{SB}}(t)\left(\mathcal{P}\hat{W}_{\mathrm{I}}(t) + \mathcal{Q}\hat{W}_{\mathrm{I}}(t)\right). \tag{2.47}$$

Similarly, an equation for $\mathcal{Q}\hat{W}_{\mathrm{I}}(t)$ is obtained. Iterative solution of these coupled equations generates a perturbation expansion of $\mathcal{P}\hat{W}_{\mathrm{I}}(t)$ in powers of $\mathcal{L}_{\mathrm{SB}}(t)$ on the r.h.s. of Eq. (2.47). Truncating the expansion at the second order and omitting the so-called initial term $\mathcal{Q}\hat{W}_{\mathrm{I}}(t_0)$ yields

$$\frac{\mathrm{d}}{\mathrm{d}t}\mathcal{P}\hat{W}_{\mathrm{I}}(t) = -\mathrm{i}\mathcal{P}\mathcal{L}_{\mathrm{SB}}(t)\mathcal{P}\hat{W}_{\mathrm{I}}(t) - \int_{t_0}^{t}\mathrm{d}\tau\mathcal{P}\mathcal{L}_{\mathrm{SB}}(t)(\mathcal{I}-\mathcal{P})\mathcal{L}_{\mathrm{SB}}(\tau)\mathcal{P}\hat{W}_{\mathrm{I}}(\tau). \tag{2.48}$$

Although Eq. (2.48) is valid for an arbitrary projector $\mathcal{P}$, to justify this omission as well as to ensure the maximum quality of the second order approximation, the choice of the operator $\mathcal{P}$ is essential, and it is best dictated by the physical situation in question. For instance, in the case of optical excitation, we can assume that the system is initially in the ground state, $\hat{\rho}(t_0) = |g\rangle\langle g|$, and the bath is in the canonical equilibrium, so that the total density matrix is factorized as $\hat{W}(t_0) = |g\rangle\langle g|\hat{W}_{\mathrm{eq}}$, where $\hat{W}_{\mathrm{eq}}$ is defined by

$$\hat{W}_{\mathrm{eq}} = \mathrm{e}^{-\beta\hat{H}_{\mathrm{B}}}/\mathrm{Tr}_{\mathrm{B}}\left\{\mathrm{e}^{-\beta\hat{H}_{\mathrm{B}}}\right\}. \tag{2.49}$$

Then, according to the Franck–Condon principle, upon the photoexcitation the bath part remains unchanged and the system–bath state remains factorized. This way the appropriate projection operator reads

$$\mathcal{P}\bullet = \mathrm{Tr}_{\mathrm{B}}\{\bullet\}\hat{W}_{\mathrm{eq}}, \tag{2.50}$$

and therefore, $\mathcal{Q}\hat{W}_{\mathrm{I}}(t_0) = 0$, which eliminates the initial term. This amounts to saying, that the projection of type Eq. (2.50) does not lead to the loss of information about the system at time t_0. In specific setups other forms of the projector are also applicable [47].

The last step is to perform the trace operation over the equilibrium bath variables. This gives the QME for the RDO in the interaction representation, which is of the second-order with respect to $\mathcal{L}_{\mathrm{SB}}$:

$$\frac{\mathrm{d}}{\mathrm{d}t}\hat{\rho}_{\mathrm{I}}(t) = -\int_{t_0}^{t}\mathrm{d}\tau\mathrm{Tr}_{\mathrm{B}}\left\{\mathcal{L}_{\mathrm{SB}}(t)(\mathcal{I}-\mathcal{P})\mathcal{L}_{\mathrm{SB}}(\tau)\hat{\rho}_{\mathrm{I}}(\tau)\hat{W}_{\mathrm{eq}}\right\}, \tag{2.51}$$

with the condition

$$\mathrm{Tr}_{\mathrm{B}}\left\{\mathcal{L}_{\mathrm{SB}}(t)\hat{\rho}_{\mathrm{I}}(t)\hat{W}_{\mathrm{eq}}\right\} = 0. \tag{2.52}$$

Eq. (2.52) is satisfied for the harmonic bath and the linear system–bath interaction, where $\mathcal{L}_{\mathrm{SB}} \propto \hat{q}$. That can be easily checked by noting that $\mathrm{Tr}_{\mathrm{B}}\left\{\hat{q}\hat{W}_{\mathrm{eq}}\right\} = 0$. Additionally, the Green's function of the free evolution can be factorized into the system and the bath Green's functions since the Hamiltonian of free evolution is block-diagonal in these spaces.

The RDO and the density operator of the bath in Eq. (2.51) are fac-

torised. This is in analogy to the Born approximation, which assumes that due to small coupling the influence of the system on the bath is negligible. This also explains the condition that the bath maintains its equilibrium at all times. Any type of system–bath interaction introduces the system–bath coherences in the total density matrix $\hat{W}$. These coherences are thus introduced perturbatively in the integral kernel. However, the perturbations are included up to infinite order through the integral over the relaxation kernel. Only the initial time t_0 is the time where the system–bath coherences are never included. Thus we have to understand Eq. (2.51) as follows: at time $t < t_0$ the system and the bath are uncoupled. Their dynamics are uncorrelated and the total density matrix is block-diagonal with respect to the system and the bath. At $t = t_0$ the interaction is switched on and the dynamics become correlated. If the bath is not in equilibrium at time t_0 or if it is correlated with the system, then the system has to be extended to include these correlation effects.

We next rewrite the QME in the Schrödinger picture in Hilbert space. Using the system–bath interaction defined in Eq. (2.17), after some rearrangements we obtain

$$\frac{\mathrm{d}}{\mathrm{d}t}\hat{\rho}(t) = -\mathrm{i}\left[\hat{H}_\mathrm{S}, \hat{\rho}(t)\right] - \sum_{i,j}\int_0^{t-t_0} \mathrm{d}\tau (C_{ij}(\tau)\left[\hat{Q}_i, \hat{U}_\mathrm{S}(\tau)\hat{Q}_j\hat{\rho}(t-\tau)\hat{U}_\mathrm{S}^\dagger(\tau)\right] - C_{ji}(-\tau)\left[\hat{Q}_i, \hat{U}_\mathrm{S}(\tau)\hat{\rho}(t-\tau)\hat{Q}_j\hat{U}_\mathrm{S}^\dagger(\tau)\right]). \quad (2.53)$$

$\hat{U}_\mathrm{S}(\tau)$ are the Hilbert space evolution operators corresponding to the system Hamiltonian. Eq. (2.53) is an integro-differential equation for the RDO due to the retarded time argument $t - \tau$. The latter means that the evolution of the system depends not only on its actual state at time t but also on its history at times $t - \tau$. Such processes are known from the probabilistic theory as non-Markovian. Thus, the reduction of the full quantum Liouville equation (which is Markovian) to the QME resulted in dynamics which include "memory effects". However, under certain circumstances these effects can be neglected to recover Markovian dynamics. Namely, if the RDO does not change substantially on the time scale of the memory effects, we can perform the so-called Markovian approximation by setting $\hat{\rho}(t-\tau) \approx \hat{\rho}(t)$ in Eq. (2.53), which yields an effectively (i.e., not physically) Markovian QME.

Notice that the form of the Markovian QME in the Liouville space can

be generalized as

$$\frac{\mathrm{d}}{\mathrm{d}t}\hat{\rho}(t) = -\mathrm{i}\mathcal{L}_{\mathrm{S}}\hat{\rho}(t) + \mathcal{D}\hat{\rho}(t). \tag{2.54}$$

The first term governs the unitary coherent evolution of the system, while the second term introduces irreversible processes, i.e. damping and relaxation. The dissipation superoperator denoted by $\mathcal{D}$ is an abstract object, the form of which is determined depending on the specific description of the dissipative dynamics. In the case of QME, the action of $\mathcal{D}$ is defined by the second term in Eq. (2.53) after replacing $\hat{\rho}(t-\tau)$ with $\hat{\rho}(t)$.

The well known Redfield equations are obtained by evaluating the Markovian QME in the energy (i.e., excitonic) representation. In this case, the first term on the r.h.s. of Eq. (2.54) for an element $\hat{\rho}_{\alpha\beta}(t)$ is $-\mathrm{i}\omega_{\alpha\beta}\hat{\rho}_{\alpha\beta}(t)$,where $\omega_{\alpha\beta} = \varepsilon_\alpha - \varepsilon_\beta$. The dissipative part reads

$$\left(\mathcal{D}\hat{\rho}(t)\right)_{\alpha\beta} = -\sum_{\alpha'\beta'} \mathcal{R}_{\alpha\beta,\alpha'\beta'}(t)\rho_{\alpha'\beta'}(t). \tag{2.55}$$

The tetradic relaxation matrix $\mathcal{R}_{\alpha\beta,\alpha'\beta'}(t)$ is the Redfield tensor given as follows:

$$\begin{aligned}\mathcal{R}_{\alpha\beta,\alpha'\beta'}(t) \equiv& \delta_{\beta\beta'}\sum_{\mu}\Gamma_{\alpha\mu,\mu\alpha'}(t) + \delta_{\alpha\alpha'}\sum_{\beta}\Gamma^*_{\beta\mu,\mu\beta'}(t) \\ &- \Gamma_{\beta'\beta,\alpha\alpha'}(t) - \Gamma^*_{\alpha'\alpha,\beta\beta'}(t).\end{aligned} \tag{2.56}$$

Here, Γ's are certain damping matrices defined as

$$\Gamma_{\alpha\beta,\alpha'\beta'}(t) \equiv \sum_{ij}\langle\alpha|\hat{Q}_i|\beta\rangle\langle\alpha'|\hat{Q}_j|\beta'\rangle\int_0^t \mathrm{d}\tau C_{ij}(\tau)\mathrm{e}^{\mathrm{i}\omega_{\beta'\alpha'}\tau}. \tag{2.57}$$

The matrix elements $\langle\alpha|\hat{Q}_i|\beta\rangle$ represent the basis transformation from molecular states to the delocalized eigenstates, and $C_{ij}(t)$ is the energy gap correlation function in the site basis Eq. (2.21).

At this stage the Redfield equations can already be used in calculations, however, assuming the electronic dynamics are much slower than the decay of the bath correlation function, the scheme can be further simplified by shifting the integration limit in Eq. (2.57) to $t \to \infty$. This yields a time-independent Redfield tensor. The so-called secular approximation [39], which decouples the evolution of populations from that of the coherences,

can be additionally applied. Formally, this approximation is realized by keeping only the tensor elements $\mathcal{R}_{\alpha\beta,\alpha\beta}$ and $\mathcal{R}_{\alpha\alpha,\beta\beta}$ while setting the others to zero.

Hierarchical equations of motion

Both FRET and QME are perturbative methods, based on either weak or strong — in comparison to the system–bath interaction — resonance coupling, accordingly. In order to describe the dynamics in situations where both interactions are of comparable strength, recently the so-called HEOM scheme has been developed. HEOM is a non-perturbative approach based on the assumption of Gaussian bath fluctuations [45, 46]. It attracts a lot of attention after demonstrating its benefits in the description of the electronic excitation dynamics in pigment–protein complexes [29]. While computationally expensive, HEOM has been applied to systems as large as $\sim$ 50 chromophores [48] — this is possible due to extensive parallelization and time-adaptive integration. Other methods to optimize HEOM include on-the-fly filtering [49] and utilization of graphical processing units for calculations [50].

The actual form of HEOM depends on the approximation of the integral in Eq. (2.23) in the form of exponential series

$$C_i(t) = \sum_{k=0}^{K} c_{ik} \mathrm{e}^{-\gamma_{ik} t} + \delta C_{iK}(t), \tag{2.58}$$

which is based on a certain sum-over-poles scheme and the residue theorem of contour integration. Term $\delta C_{iK}(t)$ takes into account the difference between the exact correlation function and the approximation. Index $k = 0$ corresponds to the pole of the spectral density defined by Eq. (2.24), while the remaining indices $k = 1, \ldots, K$ correspond to the poles from the Bose–Einstein distribution function. The conventional form of the expansion given by Eq. (2.58) is the summation over the terms with $\gamma_{ik\geq 1} = 2\pi k/\beta$, the well known Matsubara frequencies [51], however, this scheme suffers from slow convergence. Another option is the recently proposed Padé spectrum decomposition of the Bose–Einstein function [52]. We employ here the scheme that uses the $[K/K]$ Padé approximant, which was shown to provide the optimal expansion in the case of the Brownian oscillator spectral density [53]. The coefficients c_{ik} and γ_{ik} are given in terms of system characteristics, e.g., in the Appendix of Ref. [54]. We split the coefficients c_{ik} into the real and imaginary parts as $c_{ik} = c_{ik}^{\Re} + \mathrm{i} c_{ik}^{\Im}$ for later convenience. Term $\delta C_{iK}(t)$ is

approximated by a Markovian-white-noise residue ansatz [55]:

$$\delta C_{iK}(t) \approx 4R_K\lambda_i\gamma_i\beta\delta(t) \equiv \Delta_{iK}\delta(t), \tag{2.59}$$

where $\delta(t)$ is the Dirac delta function and

$$R_K = \frac{1}{4(K+1)(2K+3)}. \tag{2.60}$$

The general form of the equations is obtained after replacing the RDO in Eq. (2.54) by a set of auxiliary density operators (ADOs) $\hat{\rho}(t) \to \hat{\rho}_{\mathbf{n}}(t)$, where we define a matrix $\mathbf{n} = (n_{10}, \ldots, n_{1K}; \ldots; n_{N0}, \ldots, n_{NK})$ of non-negative integers n_{ik} for an aggregate of N chromophores. The ADO with index $\mathbf{0} = (0, \ldots, 0; \ldots; 0, \ldots, 0)$ is the RDO itself, while the remaining ones take into account the development of the system-bath correlations. The second term on the r.h.s. of Eq. (2.54) then reads:

$$\mathcal{D}\hat{\rho}_{\mathbf{n}}(t) = -\sum_{i=1}^{N}\left(\sum_{k=0}^{K}\gamma_{ik}n_{ik} + \delta\mathcal{R}_{iK}\right)\hat{\rho}_{\mathbf{n}}(t) + \sum_{i=1}^{N}\sum_{k=0}^{K}\left(\mathcal{B}_{ik}n_{ik}\hat{\rho}_{\mathbf{n}_{ik}^{-}} + \mathcal{A}_i\hat{\rho}_{\mathbf{n}_{ik}^{+}}\right), \tag{2.61}$$

where $\mathbf{n}_{ik}^{\pm} = (n_{10}, \ldots, n_{1K}; \ldots; n_{i0}, \ldots, n_{ik} \pm 1, \ldots, n_{iK}; \ldots; n_{N0}, \ldots, n_{NK})$. The auxiliary superoperators are:

$$\delta\mathcal{R}_{iK}\bullet \Leftrightarrow \frac{\Delta_{iK}}{2}[\hat{Q}_i, [\hat{Q}_i, \bullet]], \tag{2.62}$$

$$\mathcal{B}_{ik}\bullet \Leftrightarrow \mathrm{i}\left(c_{ik}^{\Re}[\hat{Q}_i, \bullet] - \mathrm{i}c_{ik}^{\Im}\{\hat{Q}_i, \bullet\}\right), \tag{2.63}$$

$$\mathcal{A}_i\bullet \Leftrightarrow \mathrm{i}[\hat{Q}_i, \bullet]. \tag{2.64}$$

The curly brackets denote the anticommutator.

The sum of indices $L = \sum_i \sum_k n_{ik}$ defines a *tier* of ADOs, and as can be seen, the superoperators $\mathcal{A}$ and $\mathcal{B}$ connect ADOs from the tier L to those from the tiers $L \pm 1$. Thus, formally the hierarchy continues to infinity. Of course, in practical calculations the hierarchy must be truncated at some finite length. Various truncation schemes are possible [56], but the choice of the scheme is of no consequence if the converged results have been reached. In this dissertation, the most simple truncation scheme is adopted, where all the ADOs with the tier $L > L_{trunc}$ are simply discarded. L_{trunc} is chosen to guarantee converged results. Note that HEOM, as given above,

propagate the ADOs in the site basis, yet the results can be presented in any other basis, e.g., the excitonic one. As far as the measurable quantities are concerned, such as the absorption spectra, they are basis-independent, and HEOM intrinsically ensure that the delocalization effects are properly taken into account.

2.4. Density matrix in the modelling of spectroscopic experiments

In the presence of an electric field, e.g., the one probing molecules in the spectroscopic experiments, the total Hamiltonian Eq. (2.2) needs to be expanded to include the coupling of the system to the field:

$$\hat{H}_{\mathrm{SF}}(t) = -\hat{\boldsymbol{\mu}}\boldsymbol{\mathcal{E}}(t) \equiv -\sum_i \boldsymbol{\mathcal{E}}(t)\left(\boldsymbol{\mu}_{ig}|i\rangle\langle g| + h.c.\right), \tag{2.65}$$

where $\hat{\boldsymbol{\mu}}$ is the dipole operator Eq. (2.10) (*h.c.* stands for Hermitian conjugate) and $\boldsymbol{\mathcal{E}}(t)$ is the electric field. The matter–light interaction Hamiltonian, Eq. (2.65), is called "semi-classical" due to the classical treatment of the field $\boldsymbol{\mathcal{E}}(t)$ while retaining the quantum description of the system. The current form of $\hat{H}_{\mathrm{SF}}$ also assumes the so-called dipole or long-wave approximation, which means that the wavelength is much larger than the physical size of the system, thus, the particles are represented by point dipoles with respect to the field. This approximation is well justified for molecular aggregates probed by visible light.

We apply the partitioning of the total Liouvillian in the manner of Eq. (2.29) by setting the perturbation part as $\mathcal{L}_{\mathrm{SF}}(t) \equiv -\boldsymbol{\mathcal{E}}(t)\mathcal{V}$, where $\mathcal{V} \Leftrightarrow [\hat{\boldsymbol{\mu}}, \bullet]$, while the reference part $\mathcal{L}_0$ corresponds to the total Hamiltonian of the system and the bath, Eq. (2.2). Then using Eqs. (2.27) and (2.37) we can write the solution for the density operator as

$$\hat{W}(t) = \mathcal{U}_0(t_0, t)\exp_+\left(\mathrm{i}\int_{t_0}^{t} \mathrm{d}\tau \boldsymbol{\mathcal{E}}(\tau)\mathcal{V}_{\mathrm{I}}(\tau)\right)\hat{W}(t_0). \tag{2.66}$$

The time ordered exponential now yields an expansion of the density operator in powers of the electric field $\boldsymbol{\mathcal{E}}(t)$,

$$\hat{W}(t) \equiv \hat{W}^{(0)}(t) + \hat{W}^{(1)}(t) + \hat{W}^{(2)}(t) + \dots, \tag{2.67}$$

where $\hat{W}^{(0)}(t) = \hat{W}(t_0)$, and we assume that the whole system is initially in the thermal equilibrium. The n-th term of the expansion reads

$$\hat{W}^{(n)}(t) = (\mathrm{i})^n \int_{t_0}^{t} \mathrm{d}\tau_n \int_{t_0}^{\tau_n} \mathrm{d}\tau_{n-1} \ldots \int_{t_0}^{\tau_2} \mathrm{d}\tau_1 \boldsymbol{\mathcal{E}}(\tau_n)\boldsymbol{\mathcal{E}}(\tau_{n-1})\ldots\boldsymbol{\mathcal{E}}(\tau_1) \times \mathcal{U}_0(\tau_n, t)\mathcal{V}\mathcal{U}_0(\tau_{n-1}, \tau_n)\mathcal{V}\ldots\mathcal{U}_0(\tau_1, \tau_2)\mathcal{V}\hat{W}(t_0). \quad (2.68)$$

We have returned to the Schrödinger picture of the dipole superoperator $\mathcal{V} = \mathcal{U}_0(t_0, t)\mathcal{V}_\mathrm{I}(t)\mathcal{U}_0^\dagger(t_0, t)$, and used the fact, that $\mathcal{U}_0(t_0, \tau_1)\hat{W}(t_0) = \hat{W}(t_0)$, which means that in the absence of the field the system does not evolve in time, but rather stays in the canonical equilibrium. Here, τ_j with $t \geqslant \tau_n \geqslant \ldots \geqslant \tau_1 \geqslant t_0$, represent the actual times of system–field interactions.

From the unitarity it follows that $\mathcal{U}_0(\tau_{n-1}, \tau_n) = \mathcal{U}_0(0, \tau_n - \tau_{n-1})$, thus, we can change the time variables from the actual interaction times τ_j into the intervals between the interactions as

$$t_1 = \tau_2 - \tau_1, \ \ldots, \ t_n = t - \tau_n \quad (2.69)$$

and then send $t_0 \to -\infty$, which results in

$$\hat{W}^{(n)}(t) = (\mathrm{i})^n \int_0^\infty \mathrm{d}t_n \int_0^\infty \mathrm{d}t_{n-1} \ldots \int_0^\infty \mathrm{d}t_1 \mathcal{U}_0(0, t_n)\mathcal{V}\mathcal{U}_0(0, t_{n-1})\mathcal{V}\ldots\mathcal{U}_0(0, t_1)\mathcal{V}\hat{W}(t_0) \times \boldsymbol{\mathcal{E}}(t - t_n)\boldsymbol{\mathcal{E}}(t - t_n - t_{n-1})\ldots\boldsymbol{\mathcal{E}}(t - t_n - t_{n-1} \ldots - t_1). \quad (2.70)$$

The physical quantity relevant in the spectroscopic experiments is the time-dependent polarization of the material, which is given by the expectation value of the dipole operator $\hat{\boldsymbol{\mu}}$:

$$\boldsymbol{P}(t) = \mathrm{Tr}\left(\hat{\boldsymbol{\mu}}\hat{W}(t)\right). \quad (2.71)$$

By substituting Eq. (2.67) into Eq. (2.71) we obtain the expansion of the polarization in powers of the field $\boldsymbol{\mathcal{E}}(t)$. In analogy to Eq. (2.67),

$$\boldsymbol{P}(t) = \boldsymbol{P}^{(1)}(t) + \boldsymbol{P}^{(2)}(t) + \boldsymbol{P}^{(3)}(t) + \ldots, \quad (2.72)$$

where

$$\boldsymbol{P}^{(n)}(t) \equiv \mathrm{Tr}\left(\hat{\boldsymbol{\mu}}\hat{W}^{(n)}(t)\right). \quad (2.73)$$

It is assumed, that in the absence of the radiation field the polarization

vanishes, thus, $\boldsymbol{P}^{(0)} = 0$. Each other term in the expansion Eq. (2.72) is related to a certain class of optical measurements. For instance, the linear polarization $\boldsymbol{P}^{(1)}$ is responsible for the linear absorption spectroscopy, while $\boldsymbol{P}^{(3)}$ describes such techniques as the pump-probe spectroscopy and various four wave mixing setups.

By combining Eqs. (2.70) and (2.72) we notice that the nth-order polarization can be given by a multiple time-convolution of the incoming fields with a field-independent function, which describes the material response:

$$\begin{aligned}\boldsymbol{P}^{(n)}(t) = \int_0^\infty \mathrm{d}t_n \int_0^\infty \mathrm{d}t_{n-1} \ldots \int_0^\infty \mathrm{d}t_1 S^{(n)}\left(t_n, t_{n-1}, \ldots, t_1\right) \\ \times \boldsymbol{\mathcal{E}}(t-t_n)\boldsymbol{\mathcal{E}}(t-t_n-t_{n-1}) \ldots \boldsymbol{\mathcal{E}}(t-t_n-t_{n-1}\ldots-t_1), \end{aligned} \tag{2.74}$$

where we define the nth-order *non-linear response function* $S^{(n)}$ [40] as

$$S^{(n)}\left(t_n, t_{n-1}, ..., t_1\right) \equiv (\mathrm{i})^n \,\mathrm{Tr}\left(\hat{\boldsymbol{\mu}}\mathcal{U}_0(0,t_n)\mathcal{V}\mathcal{U}_0(0,t_{n-1})\mathcal{V}...\mathcal{U}_0(0,t_1)\mathcal{V}\hat{W}(t_0)\right). \tag{2.75}$$

The non-linear response function, which is formally a multipoint dipole–dipole correlation function times $(\mathrm{i})^n$, carries the complete microscopic information about the system that is necessary for the calculation of an optical measurement. It can be uniformly applied to a broad range of non-linear optical measurements, which differ by the temporal sequences of pulses, their frequencies and wave-vectors.

In this dissertation two types of spectroscopic experiments are of interest: the linear absorption and the time-resolved fluorescence (TRF) spectroscopy. Both methods have a common grounding based on the response function formalism. For instance, the linear absorption is described by the absorption coefficient $\kappa_\mathrm{a}(\omega)$, which is given in terms of the linear response function by [40]

$$\kappa_\mathrm{a}(\omega) = \frac{4\pi\omega}{n(\omega)c}\mathrm{Im}\int_0^\infty \mathrm{d}t \mathrm{e}^{\mathrm{i}\omega t} S^{(1)}(t), \tag{2.76}$$

where $n(\omega)$ is the refractive index and c denotes the speed of light.

From this perspective, the TRF is characterized by four system–radiation interactions and, thus, falls into the category of third-order non-linear experiments. The first two interactions are with the incoming pump pulse, while the third and the fourth interactions are with the vacuum fluctuations of the scattered field. We approximate the envelope of the pumping

field as the delta function and treat the first two interactions as instantaneous. We denote the interval between the second and the third interaction by t. We call this time interval the waiting (or delay) time in analogy to the pump–probe experiments, however unlike in the pump-probe experiment, we do not have control over this interval. The time interval between the last two interactions is denoted by τ and is called the coherence time as will be clear from the further considerations. The "ideal" TRF spectrum, $S_{\mathrm{TRF}}(\omega, \tilde{t})$, at time $\tilde{t} = t + \tau$ is given by the expectation value of the photon emission rate [40]. In the limit of impulsive excitation, the spectrum reads

$$S_{\mathrm{TRF}}(\omega, \tilde{t}) \propto \mathrm{Re} \int_0^\infty \mathrm{d}\tau \mathrm{e}^{\mathrm{i}\omega\tau} R_{\mathrm{TRF}}(\tau, \tilde{t} - \tau), \tag{2.77}$$

where the third-order response function $R_{\mathrm{TRF}}(\tau, t)$ is given by [30]

$$R_{\mathrm{TRF}}(\tau, t) = \mathrm{Tr_B Tr_S} \left\{ \hat{\boldsymbol{\mu}} \hat{U}(t; t+\tau) \hat{U}(0; t) \hat{W}_0 \hat{U}^\dagger(0; t) \hat{\boldsymbol{\mu}} \hat{U}^\dagger(t; t+\tau) \right\}. \tag{2.78}$$

Here, $U(t_0; t)$ are the Hilbert space evolution operators, which correspond to the total Hamiltonian, Eq. (2.2), $\hat{\boldsymbol{\mu}}$ are the dipole operators and $\hat{W}_0$ is the initial density operator of the joint system. $\mathrm{Tr_{B/S}}\{\}$ denotes the trace operation over the nuclear/electronic DOF.

As can be seen, the calculation of $S_{\mathrm{TRF}}(\omega, \tilde{t})$ requires sweeping along all the values of t, over which we do not have control, as mentioned previously. However, the maximum information content about the system is enclosed within the response function, Eq. (2.78). Therefore we define another, auxiliary, form of the TRF spectrum

$$F(\omega, t) = \mathrm{Re} \int_0^\infty \mathrm{d}\tau \mathrm{e}^{\mathrm{i}\omega\tau} R_{\mathrm{TRF}}(\tau, t). \tag{2.79}$$

In this dissertation, Eq. (2.79), rather than $S_{\mathrm{TRF}}(\omega, \tilde{t})$, will be referred to as the TRF spectrum.

3. Energy transfer in the weak resonance coupling limit

In this chapter we formulate and develop a theoretical model, which allows us to describe exciton dynamics in weakly coupled molecular aggregates in terms of the RDO in the basis of the site representation of the chromophores. The excitonic coupling is treated as a perturbation and equations of motion for the RDO are derived in the second order. This enables us to retain the main excitonic effects such as transition dipole moment redistribution and transition energy shift, while simultaneously working within the basis of localized states [47]. Although FRET is the usual tool for the treatment of weakly coupled chromophores, it describes the energy transfer at longer times, after the transient coherent dynamics are suppressed by dephasing. Hence, FRET completely disregards the coherence effects, which can be important at early times of the excitation evolution. The method presented in this chapter takes such effects into account. In addition to the mentioned excitonic effects, a "dynamic localization" in the long-time limit is anticipated due to the perturbative treatment of the resonance coupling.

A proper description of initial coherent dynamics is necessary for certain dynamic spectroscopic techniques, such as 2D PE, or TRF spectroscopy. Therefore, in the second part of the chapter, a perturbative treatment of the TRF is formulated. It is based on the direct calculation of the response function by expanding it in powers of the resonance coupling up to the second order. The TRF spectra are calculated, showing both the excitonic effects and their decay, which is apparently intrinsic to the proposed scheme.

3.1. Equations of motion in the weak coupling limit

The efficient development of a certain master equation for the RDO from the Quantum Liouville equation depends on the right partitioning of the full Hamiltonian into the reference part and the perturbation. It is essentially expected that the dynamics of the RDO generated by the reference part is known (at least in principle). This is the case with the QME, where the partitioning of the Liouvillian, Eq. (2.43), ensures that in the limit of

negligible system–bath interaction, the excitonic system experiences unitary coherent evolution, which is solvable exactly. However, an analytical solution of a monomer interacting with a Gaussian bath is also known [40], which opens a possibility for an alternative approach.

The derivation of a dynamical description of the RDO in the weak resonance coupling limit is similar to that of the QME, except that this time the resonance coupling instead of the system–bath interaction is treated as a perturbation. Therefore we split the system Hamiltonian in the following way:

$$\hat{H}_{\mathrm{S}} = \hat{H}_{\varepsilon} + \hat{H}_{\mathrm{J}}. \tag{3.1}$$

Here, $\hat{H}_{\varepsilon}$ and $\hat{H}_{\mathrm{J}}$ denote accordingly the diagonal and the off-diagonal parts of the Frenkel exciton Hamiltonian, Eq. (2.6). We next define the reference part of the total Hamiltonian Eq. (2.2):

$$\hat{H}_0 = \hat{H}_{\varepsilon} + \hat{H}_{\mathrm{SB}} + \hat{H}_{\mathrm{B}}. \tag{3.2}$$

This leaves out the resonance coupling part $\hat{H}_{\mathrm{J}}$ as a perturbation. Switching into the Liouville space notation, we split the total Liouvillian in analogy to Eq. (2.43) as

$$\mathcal{L} = \mathcal{L}_0 + \mathcal{L}_{\mathrm{J}}, \tag{3.3}$$

where $\mathcal{L}_{\mathrm{J}}\hat{W} \Leftrightarrow \left[\hat{H}_{\mathrm{J}}, \hat{W}\right]$.

All the other steps are identical to those given in Sec. 2.3 and lead to the following equation for the relevant part of the density operator

$$\frac{\mathrm{d}}{\mathrm{d}t}\mathcal{P}\hat{W}_{\mathrm{I}}(t) = -\mathrm{i}\mathcal{P}\mathcal{L}_{\mathrm{J}}(t)\mathcal{P}\hat{W}_{\mathrm{I}}(t) - \int_{t_0}^{t} \mathrm{d}\tau \mathcal{P}\mathcal{L}_{\mathrm{J}}(t)(\mathcal{I}-\mathcal{P})\mathcal{L}_{\mathrm{J}}(\tau)\mathcal{P}\hat{W}_{\mathrm{I}}(\tau), \tag{3.4}$$

which is of the second-order now with respect to $\hat{H}_{\mathrm{J}}$.

Denoting $\hat{\bar{\rho}}(t) = \mathrm{Tr}_{\mathrm{B}}\left\{\hat{W}_{\mathrm{I}}(t)\right\}$ and resolving the projectors and commutators (thus, returning to the Hilbert space), we can rewrite Eq. (3.4) in terms of $\hat{\bar{\rho}}(t)$:

$$\frac{\mathrm{d}}{\mathrm{d}t}\hat{\bar{\rho}}(t)\hat{W}_{\mathrm{eq}} = -\mathrm{i}\mathrm{Tr}_{\mathrm{B}}\left\{\hat{H}_{\mathrm{J}}(t)\hat{W}_{\mathrm{eq}}\right\}\hat{\bar{\rho}}(t)\hat{W}_{\mathrm{eq}} + \mathrm{i}\hat{\bar{\rho}}(t)\mathrm{Tr}_{\mathrm{B}}\left\{\hat{W}_{\mathrm{eq}}\hat{H}_{\mathrm{J}}(t)\right\}\hat{W}_{\mathrm{eq}} - R(J^2), \tag{3.5}$$

where $\hat{H}_{\mathrm{J}}(t)$ denotes the resonance coupling term in the interaction picture,

$$\hat{H}_{\rm J}(t) \equiv \hat{U}_0^\dagger(t_0;t)\hat{H}_{\rm J}\hat{U}_0(t_0;t), \tag{3.6}$$

and

$$\begin{aligned} R(J^2) = &\int_{t_0}^{t} {\rm d}\tau \\ \Big[&{\rm Tr}_{\rm B}\left\{\hat{H}_{\rm J}(t)\hat{H}_{\rm J}(\tau)\hat{W}_{\rm eq}\right\}\hat{\bar{\rho}}(\tau) - {\rm Tr}_{\rm B}\left\{\hat{H}_{\rm J}(t)\hat{W}_{\rm eq}\right\}{\rm Tr}_{\rm B}\left\{\hat{H}_{\rm J}(\tau)\hat{W}_{\rm eq}\right\}\hat{\bar{\rho}}(\tau) \\ &-{\rm Tr}_{\rm B}\left\{\hat{H}_{\rm J}(t)\hat{\bar{\rho}}(\tau)\hat{W}_{\rm eq}\hat{H}_{\rm J}(\tau)\right\} + {\rm Tr}_{\rm B}\left\{\hat{H}_{\rm J}(t)\hat{W}_{\rm eq}\right\}\hat{\bar{\rho}}(\tau){\rm Tr}_{\rm B}\left\{\hat{W}_{\rm eq}\hat{H}_{\rm J}(\tau)\right\} \\ &-{\rm Tr}_{\rm B}\left\{\hat{H}_{\rm J}(\tau)\hat{\bar{\rho}}(\tau)\hat{W}_{\rm eq}\hat{H}_{\rm J}(t)\right\} + {\rm Tr}_{\rm B}\left\{\hat{H}_{\rm J}(\tau)\hat{W}_{\rm eq}\right\}\hat{\bar{\rho}}(\tau){\rm Tr}_{\rm B}\left\{\hat{W}_{\rm eq}\hat{H}_{\rm J}(t)\right\} \\ &+\hat{\bar{\rho}}(\tau){\rm Tr}_{\rm B}\left\{\hat{W}_{\rm eq}\hat{H}_{\rm J}(\tau)\hat{H}_{\rm J}(t)\right\} - \hat{\bar{\rho}}(\tau){\rm Tr}_{\rm B}\left\{\hat{W}_{\rm eq}\hat{H}_{\rm J}(\tau)\right\}{\rm Tr}_{\rm B}\left\{\hat{W}_{\rm eq}\hat{H}_{\rm J}(t)\right\}\Big]. \end{aligned} \tag{3.7}$$

The traces can be evaluated as follows. Taking the matrix element of ${\rm Tr}_{\rm B}\left\{\hat{H}_{\rm J}(t)\hat{W}_{\rm eq}\right\}$ we obtain the expression

$$J_{ab}(t) \equiv \langle a|{\rm Tr}_{\rm B}\left\{\hat{H}_{\rm J}(t)\hat{W}_{\rm eq}\right\}|b\rangle = J_{ab}{\rm e}^{{\rm i}\omega_{ab}t}{\rm Tr}_{\rm B}\left\{\hat{U}_a^\dagger(t)\hat{U}_b(t)\hat{W}_{\rm eq}\right\}, \tag{3.8}$$

where $\hat{U}(t)$ is the evolution operator corresponding to the Hamiltonians involving the nuclear coordinates $\hat{q}$: $\hat{H}_{\rm SB}(\hat{q}) + \hat{H}_{\rm B}(\hat{q},\hat{p})$; i.e., $\hat{U}_i(t)$ is still an operator in the bath sub-space. The trace can now be evaluated employing the second order cumulant approximation:

$${\rm Tr}_{\rm B}\left\{\hat{U}_a^\dagger(t)\hat{U}_b(t)\hat{W}_{\rm eq}\right\} = \exp\left[-(1-\delta_{ab})(g_a^*(t)+g_b(t))\right], \tag{3.9}$$

where $g_a(t)$ is the line shape function, Eq. (2.42). And thus, the resonance coupling appears effectively dressed in the line shape functions, which represent the action of the bath upon the system:

$$J_{ab}(t) = J_{ab}{\rm e}^{{\rm i}\omega_{ab}t-(1-\delta_{ab})(g_a^*(t)+g_b(t))}. \tag{3.10}$$

Similarly, the larger traces in Eq. (3.7) can be evaluated. Then changing the integration variable in Eq. (3.7) to $\tau' = t - \tau$ we can employ the Markov approximation $\hat{\bar{\rho}}(t-\tau) \approx \hat{\bar{\rho}}(t)$. Setting $t_0 = 0$ (e.g., the optical excitation giving the time reference) we obtain the equations of motion in the final form:

$$\frac{\mathrm{d}}{\mathrm{d}t}\bar{\rho}_{ab}(t) = -\mathrm{i}\sum_c J_{ac}(t)\bar{\rho}_{cb}(t) + \mathrm{i}\sum_c \bar{\rho}_{ac}(t)J_{cb}(t) - \sum_{cd}[R_{accd}(t)\bar{\rho}_{db}(t) - R^*_{cabd}(t)\bar{\rho}_{cd}(t) - R_{dbac}(t)\bar{\rho}_{cd}(t) + R^*_{bddc}(t)\bar{\rho}_{ac}(t)]. \tag{3.11}$$

The relaxation tensor reads:

$$R_{abcd}(t) = \int_0^t \mathrm{d}\tau[J_{ab}J_{cd}M_{abcd}(t, t-\tau) - J_{ab}(t)J_{cd}(t-\tau)], \tag{3.12}$$

where the auxiliary function is given as:

$$M_{abcd}(t,\tau) = \mathrm{e}^{F_{abcd}(t,\tau)+\mathrm{i}\omega_{ab}t+\mathrm{i}\omega_{cd}\tau}, \tag{3.13}$$

and

$$\begin{aligned} F_{abcd}(t,\tau) = &-g^*_a(t) - g_b(t) - g^*_c(\tau) - g_d(\tau) \\ &- \delta_{ac}(g_a(t) - g_a(t-\tau) + g^*_a(\tau)) + \delta_{ad}(g_a(t) - g_a(t-\tau) + g^*_a(\tau)) \\ &+ \delta_{bc}(g_b(t) - g_b(t-\tau) + g^*_b(\tau)) - \delta_{bd}(g_b(t) - g_b(t-\tau) + g^*_b(\tau)). \end{aligned} \tag{3.14}$$

Once we choose a specific form of the spectral density, the relaxation tensor Eq. (3.12) can be evaluated. We then solve the equations of motion for the RDO in the interaction picture, Eq. (3.11). Finally, the connection between the RDO in the interaction picture $\hat{\bar{\rho}}(t) = \mathrm{Tr}_\mathrm{B}\left\{\hat{W}_\mathrm{I}(t)\right\}$ and in the Schrödinger picture $\hat{\rho}(t) = \mathrm{Tr}_\mathrm{B}\left\{\hat{W}(t)\right\}$ is given by the equation:

$$\bar{\rho}_{ab}(t) = \mathrm{e}^{\mathrm{i}\omega_{ab}t+(1-\delta_{ab})[g_a(t)+g^*_b(t)]}\rho_{ab}(t). \tag{3.15}$$

To calculate the response functions needed for the evaluations of the optical spectra in general (conf., Eq. (2.76)), one needs to calculate the Liouville space evolution operators $\mathcal{U}(t)$ which fulfil the relation

$$\rho_{ab}(t) = \sum_{cd}\mathcal{U}_{abcd}(t)\rho_{cd}(0). \tag{3.16}$$

We use a simple consequence of this equation, namely

$$\mathcal{U}_{abcd}(t) = \rho_{ab}^{(cd)}(t), \tag{3.17}$$

where $\rho_{ab}^{(cd)}(t)$ is calculated using equations of motion, Eq. (3.11), with the initial condition $\rho_{ab}^{(cd)}(0) = \delta_{ac}\delta_{bd}$. If any of the indices a, b, c, d equals g, we have $R_{abcd} = 0$. For the optical coherences involving the ground state we therefore obtain the following equations of motion:

$$\frac{\mathrm{d}}{\mathrm{d}t}\bar{\rho}_{ag}(t) = -\mathrm{i}\sum_{c} J_{ac}(t)\bar{\rho}_{cg}(t) + \sum_{c}\sum_{d\neq a,c} R_{addc}(t)\bar{\rho}_{cg}(t). \tag{3.18}$$

The absorption spectrum, Eq. (2.76), is then given by the expression

$$\kappa_{\mathrm{a}}(\omega) \approx \frac{\omega}{n(\omega)}\mathrm{Re}\int_0^\infty \mathrm{d}t\mathrm{e}^{\mathrm{i}\omega t}\left\langle \sum_{ab}\mu_{ga}\mathcal{U}_{agbg}(t)\mu_{bg}\rho_{gg}\right\rangle, \tag{3.19}$$

where $\langle \dots \rangle$ represents the averaging the over isotropic distribution of orientations of the molecular transitions with respect to the light polarization. The transition dipole moments μ_{ag} have to be understood as projections of the transition dipole moments on the light polarization vector $\mathbf{e}$, that is, $\mu_{ag} = \boldsymbol{\mu}_{ag}\cdot\mathbf{e}$. The averaging is done over the product of two such quantities. We have the orientational factor

$$\Omega_{ab} \equiv \frac{\langle(\boldsymbol{\mu}_{ag}\cdot\mathbf{e})(\boldsymbol{\mu}_{bg}\cdot\mathbf{e})\rangle_{\mathrm{orient.}}}{|\boldsymbol{\mu}_{ag}||\boldsymbol{\mu}_{bg}|} = \frac{1}{3}\frac{\boldsymbol{\mu}_{ag}\cdot\boldsymbol{\mu}_{bg}}{|\boldsymbol{\mu}_{ag}||\boldsymbol{\mu}_{bg}|}. \tag{3.20}$$

If one now defines $\bar{\mu}_{ag}$ as $\bar{\mu}_{ag} \equiv |\boldsymbol{\mu}_{ag}|$, one can write

$$\kappa_{\mathrm{a}}(\omega) \approx \frac{\omega}{n(\omega)}\mathrm{Re}\int_0^\infty \mathrm{d}t\mathrm{e}^{\mathrm{i}\omega t}\sum_{ab}\Omega_{ab}\bar{\mu}_{ga}\bar{\mu}_{bg}\mathcal{U}_{agbg}(t)\rho_{gg}. \tag{3.21}$$

We use Eq. (3.21) in subsequent simulations of the absorption spectra. It is important to note that because we do not work with electronic eigenstates one cannot assume the secular approximation ($\mathcal{U}_{abcd}(t) = \delta_{ac}\delta_{bd}\mathcal{U}_{abab}(t)$) to be valid, and the orientational factor does not reduce to simple 1/3.

3.2. Main features of the weak resonance coupling model

To demonstrate the main features of the theory given above, we model a molecular dimer, which is the simplest system, where the effects of a weak excitonic coupling can be observed. Namely, the resonance interac-

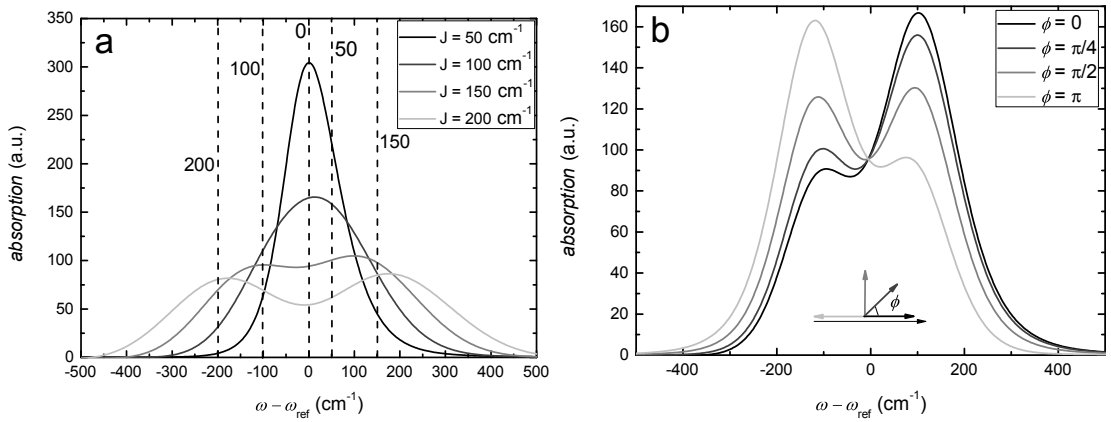

Figure 3.1 Absorption spectra of an excitonic dimer. The spectra display the splitting of the levels (a), as well as the transition dipole moment redistribution (b). The dashed vertical lines in (a) denote the position of the peak, corresponding to certain resonance coupling J, as expected from the excitonic theory. In (b), ϕ is the angle between the dipole moment vectors $\boldsymbol{\mu}_{ag}$ and $\boldsymbol{\mu}_{bg}$ lying in one plane.

tion should lead to the splitting of the excited states, redistribution of the transition dipole moments and a shift of excited state absorption. The first two effects will be demonstrated in the absorption spectrum. In addition, one can also expect energy transfer between the two split excitonic levels, formation of a coherence between excitonic levels upon excitation by light and its dephasing. This class of effects is associated with the evolution of the system in the excited state band, which we will show afterwards.

The absorption spectra of a dimer are shown in Fig. 3.1. The energies of the monomers are defined as $\varepsilon_{a,b} = \omega_{\text{ref}} \pm \delta\varepsilon$, where ω_{ref} is some reference energy and $2\delta\varepsilon$ is the energy difference. Coupling to the bath is parametrized by identical reorganization energies $\lambda = 20\,\text{cm}^{-1}$ and vibrational relaxation times $\gamma = 100\,\text{fs}^{-1}$; the temperature is 300 K.

Fig. 3.1(a) presents the absorption spectra of a model homodimer ($\delta\varepsilon = 0$) with resonance coupling J varying from $50\,\text{cm}^{-1}$ to $200\,\text{cm}^{-1}$. Because the monomeric transition energies of the two levels are the same, excitonic mixing of the two levels is maximal at any resonance coupling value. We have artificially chosen the dipole moments perpendicular to each other to eliminate the effect of the transition dipole moment redistribution. We can see from Fig. 3.1(a) that the prediction of the absorption maxima agrees rather well with the prediction of the excitonic model (splitting of $2J$). It can also be noticed that the splitting is smaller than predicted by the excitonic theory when resonance coupling is small, most likely due to the bath changing the excitonic coupling term in Eq. (3.10).

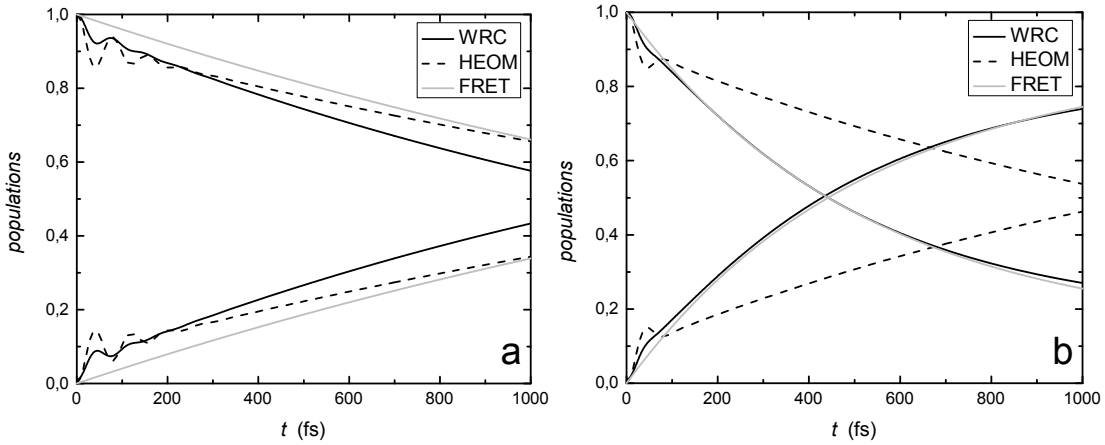

Figure 3.2 Evolutions of the populations of an excitonic dimer. The evolutions are calculated by the weak resonance coupling (WRC) method (full black lines), the HEOM (dashed black lines) and the FRET method (grey lines): (a) $T = 70\,\mathrm{K}$; (b) $T = 300\,\mathrm{K}$.

The effect of the transition dipole moment redistribution is illustrated in Fig. 3.1(b). A heterodimer with a gap of $2\delta\varepsilon = 200\,\mathrm{cm}^{-1}$ between the transition energies of the two monomers was chosen, and the absorption spectrum was calculated for a fixed resonance coupling value of $J = 50\,\mathrm{cm}^{-1}$. Different mutual orientations of the dipole moments lead to enhancement of the absorption of one or the other split level, depending on the mutual orientation of the molecules.

To study the dynamical properties of the method for the weak resonance coupling, we look at the population evolutions within a molecular dimer. Fig. 3.2 shows the evolutions calculated by three methods: the current (weak resonance coupling) method, the HEOM, which is exact in various coupling regimes, and the FRET, which is the central method for the treatment of energy transfer between weakly coupled chromophores. The dimer parameters are: $2\delta\varepsilon = 400\,\mathrm{cm}^{-1}$ and $J = 80\,\mathrm{cm}^{-1}$; the system–bath coupling parameters are: $\lambda = 20\,\mathrm{cm}^{-1}$ and $\gamma = 100\,\mathrm{fs}^{-1}$. The evolutions were calculated for the low and high temperatures: (a) 70 K and (b) 300 K, accordingly. Initially the population of the upper state is unity, while the lower state is not populated, and we observe the relaxation to equilibrium.

In the case of low temperature, Fig. 3.2(a), the HEOM initially show short-living coherent oscillations, which are to some extent reproduced by the current method: the temporal parameters (frequency, lifetime) are in good agreement, but the amplitude is smaller. At longer times the HEOM solutions approach the FRET ones, while the weak resonance coupling scheme shows faster population transfer. At high temperatures, Fig. 3.2(b),

the initial oscillations are significantly shorter, but still present in both the HEOM and the weak resonance coupling scheme evolutions. The latter afterwards closely follows the FRET results, which considerably diverge from the HEOM at long times. On the one hand, these results demonstrate that the results of the weak resonance coupling scheme are trustworthy at the initial times only, which is of course expected for a method based on the perturbative expansion. On the other hand, the evolutions given by the current scheme correlate well with the FRET and at the same time add the correct initial behaviour, e.g., the coherent oscillations.

To additionally assess the validity of the current method in the long-time limit, we look at the stationary population values. The detailed balance condition ensures, that in the thermodynamical equilibrium the relation $\rho_{aa}/\rho_{bb} = \exp(-2\delta\varepsilon/k_{\mathrm{B}}T)$, $\varepsilon_b < \varepsilon_a$, holds. Whether this condition applies to the current method or not, one can check by plotting the logarithm of the ratio of the stationary populations against the energy gap between the states. This is shown in Fig. 3.3. The resonance coupling was set to $J = 80\,\mathrm{cm}^{-1}$, while the system–bath coupling parameters are the same as in Fig. 3.2. As can be seen, for energy gaps $2\delta\varepsilon \leq k_{\mathrm{B}}T$ the equilibrium population obey the detailed balance that corresponds to the monomeric (i.e., not excitonically split) energy gap. For larger energy gaps, the equilibrium population values deviate appreciably from the detailed balance condition. Two conclusions can be drawn from the observations. Firstly, it can be concluded that the equations of motion, Eq. (3.11), largely obey the detailed balance condition with respect to the monomeric energy gap. Secondly, it must be noted, that the method describes the thermodynamics well only for energy gap comparable to $k_{\mathrm{B}}T$, and by the same token, the long-time behaviour of the equations Eq. (3.11) is in a better agreement with the detailed balance condition at higher temperatures.

Generalizing the results of this Section, we can conclude that the equations of motion, based on the perturbative treatment of the resonance coupling, capture the excitonic effects, which can be either static (e.g., the energy level splitting, redistribution of the dipole moments) or dynamic (such as the coherent oscillations). In addition to that, as follows from the equilibrium population values, the excitations initially displaying signs of excitonic delocalization tend to be localized during the course of time. Thus, we are able to describe an effect of dynamic localization, where the bath destroys not only a wavepacket created in the complex by ultrafast excitation, but also the coherence established by the weak resonance coupling.

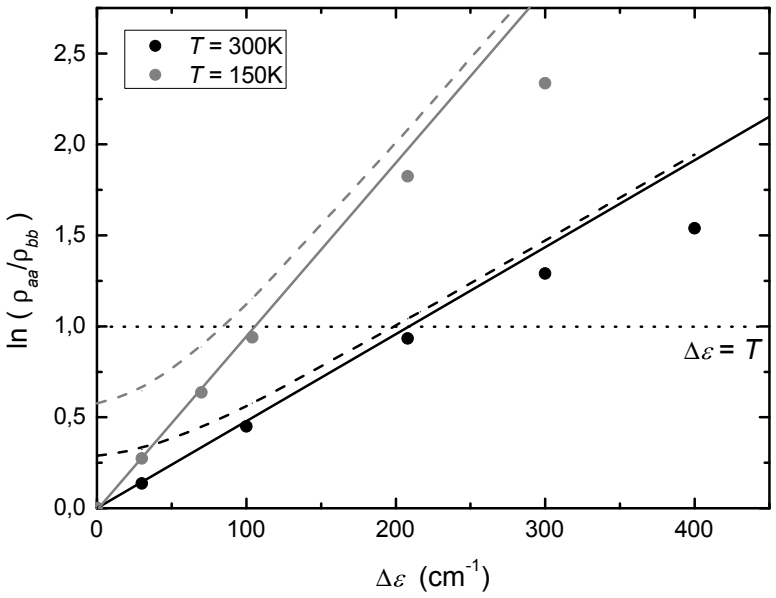

Figure 3.3 Equilibrium population values of the weak resonance coupling model. The full lines shown the detailed balance condition for the monomeric energy gap, $\Delta\varepsilon = 2\delta\varepsilon$, while the dashed lines show the same dependence for the excitonic energy gap, $\Delta_{\mathrm{e}}\varepsilon = \Delta\varepsilon\sqrt{1 + J/\delta\varepsilon}$. The dots represent the values calculated within the current model. The high temperature (300 K) results are shown in black, while the low temperature (150 K) results are in grey. The dotted horizontal line corresponds to energy gap $\Delta\varepsilon = k_{\mathrm{B}}T$.

3.3. Time-resolved fluorescence in weakly coupled dimer

Although the evolution of the density operator reveals certain features of coherent dynamics, such as the oscillatory populations, the density operator itself is not an observable quantity. Therefore, in order to investigate the coherence in energy transfer and the dynamical excitation localization, apparently intrinsic to the method developed here, we look at the time-resolved fluorescence, which allows us to follow the evolution of the excited state. To that end we need to evaluate the corresponding third-order response function, Eq. (2.78). One way to do that would be by calculating the evolution operators in the manner of Eq. (3.17). However, this would not give the expected result, because the evolution operators would be calculated with the wrong initial condition. Namely, the evolution during the second interval need not start with the bath being in the equilibrium with respect to the ground state, as implied by the projector of the type Eq. (2.50). Therefore, we provide an alternative treatment of the problem. The main idea is to expand the evolution operators in powers of the resonance coupling, performing the trace over the nuclear DOF as the last operation, which allows for a continuous evolution of the bath.

Evaluating the trace in Eq. (2.78) only over the electronic DOF, $\mathrm{Tr_S}\{\}$, we can write R_{TRF} as

$$R_{\mathrm{TRF}}(\tau,t) = \sum_{a,b,c,e} \mu_{ga}\mu_{cg} \times \mathrm{Tr_B}\left\{\hat{U}_{ab}(t;t+\tau)\hat{U}_{be}(0;t)\rho_{ee}\hat{W}_{\mathrm{eq}}\hat{U}^{\dagger}_{ec}(0;t)\hat{U}^{\dagger}_{gg}(t;t+\tau)\right\}. \tag{3.22}$$

We have made an assumption, that initially the density operator can be partitioned into the diagonal reduced density operator of the system and the equilibrium density operator of the bath. The structure $\mathrm{Tr_B}\left\{\ldots\,\hat{W}_{\mathrm{eq}}\right\}$ has the meaning of averaging over the nuclear DOF, and again we note that $\hat{U}_{ij}(t_0;t)$ are still operators in the bath sub-space. The expression within the trace is the evolution of the reduced density matrix, which can be represented by means of the double-sided Feynman diagram [40], Fig. 3.4. The vertical arrows correspond to the evolution of the ket and the bra of the density operator, while the wiggly arrows indicate the interaction of the system with the radiation field of either the laser pulse or the vacuum. As shown, initially the system is in the population state $|e\rangle\langle e|$, which in the

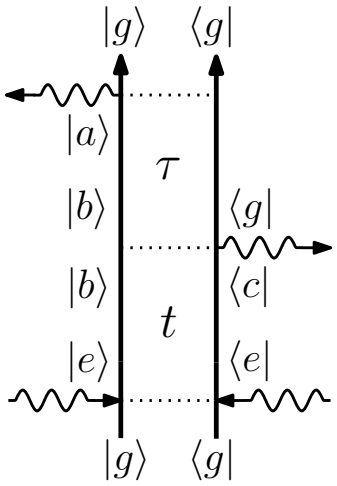

Figure 3.4 Double-sided Feynman diagram corresponding to the TRF.

general case evolves into a coherence $|b\rangle\langle c|$ during the waiting time t. An optical coherence, $|b\rangle\langle g|$, is then created, which evolves during the coherence time τ (possibly, into some other optical coherence $|a\rangle\langle g|$), thus, emitting the signal. The TRF spectrum, Eq. (2.79), thus allows us to study the dynamics of the excited state by the parametric dependence on the waiting time t.

In order to evaluate the Eq. (3.22), we need to calculate the elements of the evolution operators $\hat{U}_{ij}(t_0;t)$. To this end we first split the evolution operator in the following manner:

$$\hat{U}(t_0;t) = \hat{U}_0(t_0;t)\hat{\tilde{U}}(t_0;t), \tag{3.23}$$

here, $\hat{U}_0(t_0;t)$ represents the individual evolution of monomers interacting with the environment and independent from each other, while $\hat{\tilde{U}}(t_0;t)$ describes the evolution induced by the resonance interaction. We can write down $\hat{\tilde{U}}(t_0;t)$ in terms of time-ordered exponential:

$$\hat{\tilde{U}}(t_0;t) = \exp_+\left[-\mathrm{i}\int_{t_0}^{t}\mathrm{d}\tau\hat{H}_\mathrm{J}(\tau)\right], \tag{3.24}$$

where $\hat{H}_\mathrm{J}(t)$ is the resonance coupling in the interaction picture, Eq. (3.6).

Given these definitions, an operator $\hat{U}_{ab}(t_0;t)$ reads:

$$\hat{U}_{ab}(t_0;t) = \mathrm{e}^{-\mathrm{i}\varepsilon_a(t-t_0)}\hat{U}_a(t_0;t)\hat{\tilde{U}}_{ab}(t_0;t), \tag{3.25}$$

where $\hat{U}_a(t_0;t)$ denotes the evolution of the bath associated with the state $|a\rangle$, and $\hat{\tilde{U}}_{ab}(t_0;t)$ is given as the following expansion:

$$\hat{\tilde{U}}_{ab}(t_0;t) = \delta_{ab} - \mathrm{i}\int_{t_0}^{t} \mathrm{d}\tau J_{ab} \mathrm{e}^{\mathrm{i}\omega_{ab}(\tau-t_0)} \hat{U}_a^{\dagger}(t_0;\tau)\hat{U}_b(t_0;\tau) + \sum_{n=2}^{\infty}(-\mathrm{i})^n \sum_{c_1\ldots c_{n-1}} \int_{t_0}^{t}\mathrm{d}\tau_n \ldots \int_{t_0}^{\tau_2} \mathrm{d}\tau_1 J_{ac_{n-1}}\ldots J_{c_1 b}\mathrm{e}^{\mathrm{i}\omega_{ac_{n-1}}(\tau_n-t_0)}\ldots \mathrm{e}^{\mathrm{i}\omega_{c_1 b}(\tau_1-t_0)} \times \hat{U}_a^{\dagger}(t_0;\tau_n)\hat{U}_{c_{n-1}}(t_0;\tau_n)\ldots\hat{U}_{c_1}^{\dagger}(t_0;\tau_1)\hat{U}_b(t_0;\tau_1). \quad (3.26)$$

We can then rewrite Eq. (3.22) as:

$$R_{\mathrm{TRF}}(\tau,t) = \sum_{a,b,c,e} \mu_{ga}\mu_{cg}\mathrm{e}^{-\mathrm{i}\omega_{ag}\tau-\mathrm{i}\omega_{bc}t} \times \mathrm{Tr}_{\mathrm{B}}\left\{\hat{U}_a(t;t+\tau)\hat{\tilde{U}}_{ab}(t;t+\tau)\hat{U}_b(0;t)\hat{\tilde{U}}_{be}(0;t)\rho_{ee}\hat{W}_{\mathrm{eq}}\hat{\tilde{U}}_{ec}^{\dagger}(0;t)\hat{U}_c^{\dagger}(0;t)\right\}. \quad (3.27)$$

By expanding the elements $\hat{\tilde{U}}(t_0;t)$ in powers of resonance coupling as given in Eq. (3.26) we can write the response function $R_{\mathrm{TRF}}(\tau,t)$ as a perturbation series:

$$R_{\mathrm{TRF}}(\tau,t) = R^{(0)}(\tau,t) + R^{(1)}(\tau,t) + R^{(2)}(\tau,t) + \ldots \quad (3.28)$$

The zeroth-order term $R^{(0)}(\tau,t)$ corresponds to the sum of the TRF of individual (uncoupled) monomers: $R^{(0)}(\tau,t) = \sum_e R_e^{(0)}(\tau,t)$. In this case an exact result can be recovered by means of cumulant expansion of the bath correlations [40, 47], namely

$$\mathrm{Tr}_{\mathrm{B}}\left\{\hat{U}_e^{\dagger}(0;t)\hat{U}_e(0;t+\tau)\hat{W}_{\mathrm{eq}}\right\} = \exp\left(-g_e^*(\tau) + 2\mathrm{i}\mathrm{Im}\left\{g_e(t) - g_e(t-\tau)\right\}\right). \quad (3.29)$$

Any cross-correlations between the sites are again excluded, which is a somewhat artificial limitation set here only for convenience. By setting the initial condition for the electronic sub-system as $\rho_{ee} = |\mu_{eg}|^2$ we get

$$R_e^{(0)}(\tau,t) = \mathrm{i}^3|\mu_{eg}|^4\mathrm{e}^{-\mathrm{i}\omega_{eg}\tau - g_e^*(\tau)+2\mathrm{i}\mathrm{Im}\left\{g_e(t)-g_e(t-\tau)\right\}}. \quad (3.30)$$

Higher-order terms of Eq. (3.27) describe various processes, depending on which of the three $\hat{\tilde{U}}(t_0;t)$ terms or their combinations we expand. This can be also represented pictorially by means of the double-sided Feynman

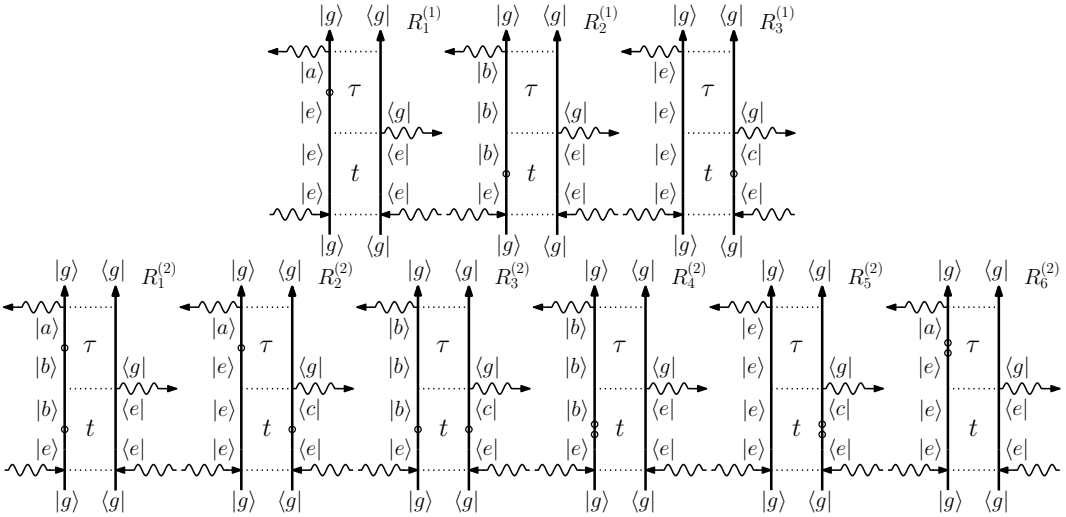

Figure 3.5 Double-sided Feynman diagrams of the first and the second order with respect to the resonance interaction. The dots denote the change of the bra/ket due to the action of the resonance coupling.

diagrams: the three first-order and the six second-order terms (the numbering is arbitrary) are shown in Fig. 3.5. For a dimer a natural restriction $J_{ab}J_{bc} \Leftrightarrow a = c$ applies, which somewhat simplifies the expressions. Hence, the three first-order terms for a dimer read:

$$R_1^{(1)}(\tau,t) = \sum_{e,b} (-\mathrm{i}J_{be})\,\mu_{gb}\mu_{eg}|\mu_{eg}|^2 \mathrm{e}^{-\mathrm{i}\omega_{bg}\tau + 2\mathrm{i}\mathrm{Im}\{g_e(t)\}}$$
$$\times \int_t^{t+\tau} \mathrm{d}\tau_1 \exp\left[\mathrm{i}\omega_{be}(\tau_1 - t) - 2\mathrm{i}\mathrm{Im}\{g_e(\tau_1)\} - g_b(t+\tau-\tau_1) - g_e^*(\tau_1 - t)\right]; \tag{3.31}$$

$$R_2^{(1)}(\tau,t) = \sum_{e,b} (-\mathrm{i}J_{be})\,\mu_{gb}\mu_{eg}|\mu_{eg}|^2 \mathrm{e}^{-\mathrm{i}\omega_{bg}\tau + 2\mathrm{i}\mathrm{Im}\{g_e(t)\} - \mathrm{i}\omega_{be}t}$$
$$\times \int_0^{t} \mathrm{d}\tau_1 \exp\left[\mathrm{i}\omega_{be}(\tau_1) - 2\mathrm{i}\mathrm{Im}\{g_e(\tau_1)\} - g_b(t+\tau-\tau_1) - g_e(t - \tau_1)\right]; \tag{3.32}$$

$$R_3^{(1)}(\tau,t) = \sum_{e,b} (+\mathrm{i}J_{eb})\,\mu_{bg}\mu_{ge}|\mu_{eg}|^2 \mathrm{e}^{-\mathrm{i}\omega_{eg}\tau - 2\mathrm{iIm}\,\{g_e(t+\tau)\} - \mathrm{i}\omega_{eb}t} \times \int_0^t \mathrm{d}\tau_1 \exp\left[\mathrm{i}\omega_{eb}(\tau_1) + 2\mathrm{iIm}\,\{g_e(\tau_1)\} - g_e^*(t+\tau-\tau_1) - g_b^*(t-\tau_1)\right]. \tag{3.33}$$

The six second-order terms for a dimer read:

$$R_1^{(2)}(\tau,t) = -\sum_{e,b} |J_{eb}|^2 R_e^{(0)}(\tau,t) \times \int_t^{t+\tau} \mathrm{d}\tau_2 \exp\left[\mathrm{i}\omega_{eb}\tau_2 + 2\mathrm{iIm}\,\{g_e(\tau_2)\} - g_e(t+\tau-\tau_2) + g_e^*(\tau_2-t)\right] \times \int_0^t \mathrm{d}\tau_1 \exp[\mathrm{i}\omega_{be}\tau_1 - 2\mathrm{iIm}\,\{g_e(\tau_1)\} + g_e(t+\tau-\tau_1) - g_e(t-\tau_1) - g_e(\tau_2-\tau_1) - g_b(\tau_2-\tau_1)]; \tag{3.34}$$

$$R_2^{(2)}(\tau,t) = \sum_{e,b} |J_{eb}|^2 |\mu_{eg}|^2 |\mu_{bg}|^2 \mathrm{e}^{-\mathrm{i}\omega_{bg}\tau - g_b^*(\tau)} \times \int_t^{t+\tau} \mathrm{d}\tau_2 \exp\left[\mathrm{i}\omega_{be}\tau_2 - 2\mathrm{iIm}\,\{g_e(\tau_2)\} - g_b(t+\tau-\tau_2) + g_b(t-\tau_2)\right] \times \int_0^t \mathrm{d}\tau_1 \exp[\mathrm{i}\omega_{eb}\tau_1 + 2\mathrm{iIm}\,\{g_e(\tau_1)\} + g_b^*(t+\tau-\tau_1) - g_b^*(t-\tau_1) - g_e^*(\tau_2-\tau_1) - g_b^*(\tau_2-\tau_1)]; \tag{3.35}$$

$$R_3^{(2)}(\tau,t) = \sum_{e,b} |J_{eb}|^2 |\mu_{eg}|^2 |\mu_{bg}|^2 \mathrm{e}^{-\mathrm{i}\omega_{bg}\tau - g_b^*(\tau)} \times \int_0^t \mathrm{d}\tau_2 \exp\left[\mathrm{i}\omega_{eb}\tau_2 + 2\mathrm{iIm}\,\{g_e(\tau_2)\} + g_b^*(t+\tau-\tau_2) - g_b^*(t-\tau_2)\right] \times \int_0^t \mathrm{d}\tau_1 \exp[\mathrm{i}\omega_{be}\tau_1 - 2\mathrm{iIm}\,\{g_e(\tau_1)\} - g_b(t+\tau-\tau_1) + g_b(t-\tau_1) - g_e(\tau_2-\tau_1) - g_b(\tau_2-\tau_1)]; \tag{3.36}$$

$$R_4^{(2)}(\tau,t) = -\sum_{e,b} |J_{eb}|^2 R_e^{(0)}(\tau,t) \times \int_0^t \mathrm{d}\tau_2 \exp\left[\mathrm{i}\omega_{eb}\tau_2 + 2\mathrm{i}\mathrm{Im}\left\{g_e(\tau_2)\right\} - g_e(t+\tau-\tau_2) + g_e(t-\tau_2)\right] \times \int_0^{\tau_2} \mathrm{d}\tau_1 \exp[\mathrm{i}\omega_{be}\tau_1 - 2\mathrm{i}\mathrm{Im}\left\{g_e(\tau_1)\right\} + g_e(t+\tau-\tau_1) - g_e(t-\tau_1) - g_e(\tau_2-\tau_1) - g_b(\tau_2-\tau_1)]; \quad (3.37)$$

$$R_5^{(2)}(\tau,t) = -\sum_{e,b} |J_{eb}|^2 R_e^{(0)}(\tau,t) \times \int_0^t \mathrm{d}\tau_2 \exp\left[\mathrm{i}\omega_{be}\tau_2 - 2\mathrm{i}\mathrm{Im}\left\{g_e(\tau_2)\right\} + g_e^*(t+\tau-\tau_2) - g_e^*(t-\tau_2)\right] \times \int_0^{\tau_2} \mathrm{d}\tau_1 \exp[\mathrm{i}\omega_{eb}\tau_1 + 2\mathrm{i}\mathrm{Im}\left\{g_e(\tau_1)\right\} - g_e^*(t+\tau-\tau_1) + g_e^*(t-\tau_1) - g_e^*(\tau_2-\tau_1) - g_b^*(\tau_2-\tau_1)]; \quad (3.38)$$

$$R_6^{(2)}(\tau,t) = -\sum_{e,b} |J_{eb}|^2 R_e^{(0)}(\tau,t) \times \int_t^{t+\tau} \mathrm{d}\tau_2 \exp\left[\mathrm{i}\omega_{eb}\tau_2 + 2\mathrm{i}\mathrm{Im}\left\{g_e(\tau_2)\right\} - g_e(t+\tau-\tau_2) + g_e^*(\tau_2-t)\right] \times \int_t^{\tau_2} \mathrm{d}\tau_1 \exp[\mathrm{i}\omega_{be}\tau_1 - 2\mathrm{i}\mathrm{Im}\left\{g_e(\tau_1)\right\} + g_e(t+\tau-\tau_1) - g_e^*(\tau_1-t) - g_e(\tau_2-\tau_1) - g_b(\tau_2-\tau_1)]. \quad (3.39)$$

To demonstrate the main features of the theory presented above, we have modelled the TRF spectra, Eq. (2.79), of an excitonic heterodimer, described by the energy gap $2\delta\varepsilon = 400\,\mathrm{cm}^{-1}$ and resonance coupling $J = 80\,\mathrm{cm}^{-1}$. The reorganization energies are $\lambda = 30\,\mathrm{cm}^{-1}$ and the vibrational relaxation rates are $\gamma^{-1} = 100\,\mathrm{fs}$. The transition dipole moments are chosen $|\mu_{ag}| = |\mu_{bg}| = 0.5$, which leads to equally populated states at $t = 0$; the dipole moments are additionally treated as being parallel (for simplicity we also disregard the orientational averaging). The temperature is 70 K.

We first calculate the TRF signal at waiting time $t = 0$, when the relaxation effects are absent, and the TRF spectrum coincides with the linear

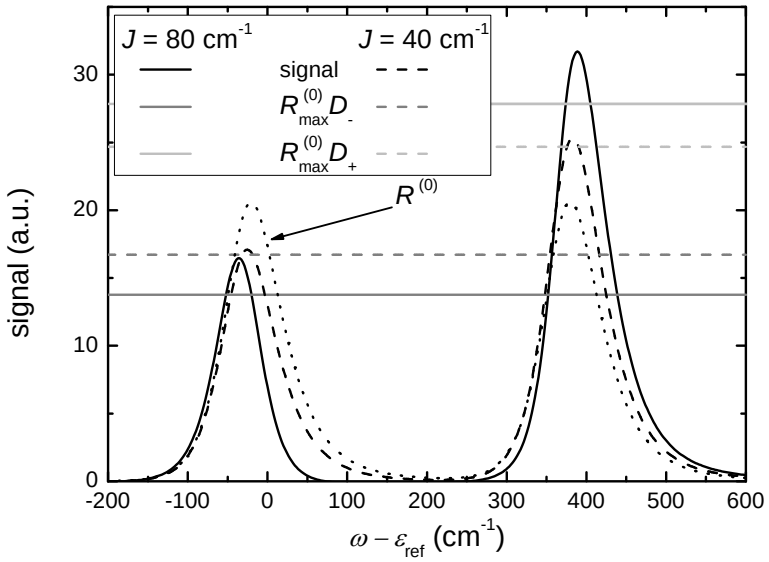

Figure 3.6 TRF signal at early times. The waiting time is $t = 0\,\mathrm{fs}$. Black lines show the signal corresponding to $J = 80\,\mathrm{cm}^{-1}$ (full line) and $J = 40\,\mathrm{cm}^{-1}$ (dashed line). The monomeric signal is shown in dots. The horizontal lines demonstrate the intensity estimates for the stronger (light grey lines) and weaker (dark grey lines) transitions from the exciton theory (see text for details).

absorption. In Fig. 3.6 the TRF signal is shown at $t = 0\,\mathrm{fs}$. Two rather well separated peaks can be seen because of the small reorganization energies, $\lambda \ll 2\delta\varepsilon$, and low temperature. The black dotted line represents the monomeric signal, i.e., it corresponds to $R^{(0)}$, while the two other black lines show the total signal for two values of resonance coupling: $J = 80\,\mathrm{cm}^{-1}$ (full line) and $J = 40\,\mathrm{cm}^{-1}$ (dashed line). The difference in amplitude of the total and the monomeric signals, resembles the effect of the excitonic oscillator strength redistribution. We estimate the latter as given by the exciton theory. Namely, the excitonic dipole strength $D_\pm$ of a dimer of two identical dipoles in a parallel configuration is given by [4]

$$D_\pm = d\left(1 \pm \frac{1}{\sqrt{1 + (\delta\varepsilon/J)^2}}\right), \tag{3.40}$$

where $\pm$ denotes a corresponding exciton state, $d = |\mu_{ag}|^2 = |\mu_{bg}|^2$ is the molecular dipole strength and $\delta\varepsilon/J$ is the excitonic mixing parameter. Multiplying the maximum value of the $R^{(0)}$ signal, $R^{(0)}_{\mathrm{max}}$, by the corresponding dipole strength, we obtain the estimates for the signal, that would follow from the excitonic picture. The predicted levels of the stronger and weaker transitions ($R^{(0)}_{\mathrm{max}} D_+$ and $R^{(0)}_{\mathrm{max}} D_-$) are shown in Fig. 3.6 by the light and dark gray lines accordingly. Evidently, our results correlate well

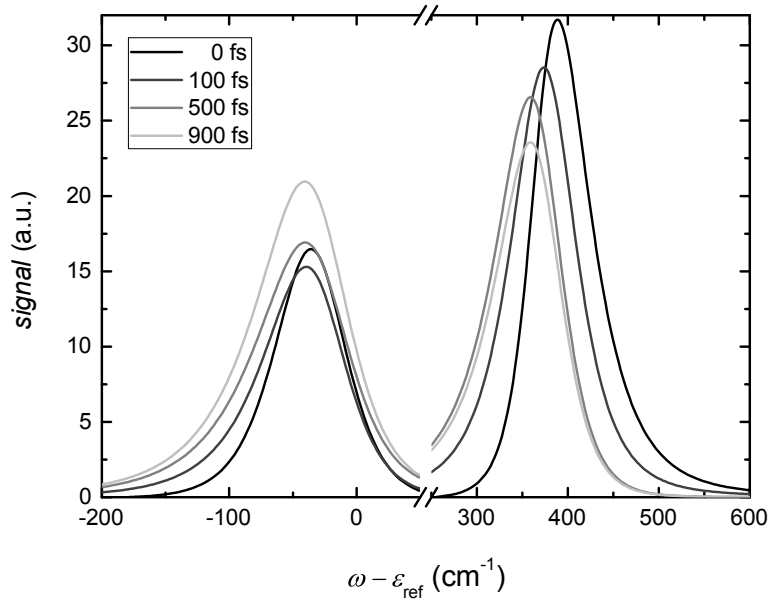

Figure 3.7 Time dependence of the TRF spectra. The spectra are calculated for waiting times $t = 0, \ldots, 900\,\mathrm{fs}$, shown form dark grey to light grey.

with Eq. (3.40), and we note that decreasing the resonance coupling yields a better agreement with the excitonic theory. Thus, the comparison of the two methods can be used to evaluate the limits for the resonance coupling with respect to the energy gap $2\delta\varepsilon$ in the current scheme.

Let us now look at the time evolution of the spectrum, which is shown in Fig. 3.7. Surprisingly, the dynamics of the two peaks are very different. While the fluorescence of the upper peak shows a clearly pronounced time-dependent Stokes shift [40] and a rather steady decrease in amplitude, the lower peak is fairly stationary in frequency, and its amplitude firstly decreases ($0 - 200\,\mathrm{fs}$) and later grows ($300\,\mathrm{fs}$ and up). The evolution in short times (up to $\approx 100\,\mathrm{fs}$) is even more complicated due to the coherent oscillations, therefore we do not show it in the form of spectra. The information content in Fig. 3.7 is too large to analyze directly, therefore we look separately at the time dependence of the amplitudes and positions of the peaks.

Firstly, we plot the frequency of the fluorescence maxima as a function of the waiting time. Figure 3.8 shows the results for the upper (a) and lower (b) peaks (full dots). Additionally, we show the maxima of the $R^{(0)}$ only (open dots), which corresponds to the fluorescence of the monomeric states. As far as the latter is concerned, the curves in both (a) and (b) are identical, only shifted by ω_{ab}, and they demonstrate the time-dependent Stokes shift. Looking at the upper peak, Fig. 3.8(a), we notice, that at short times the peak within the dimer is at higher frequencies than the

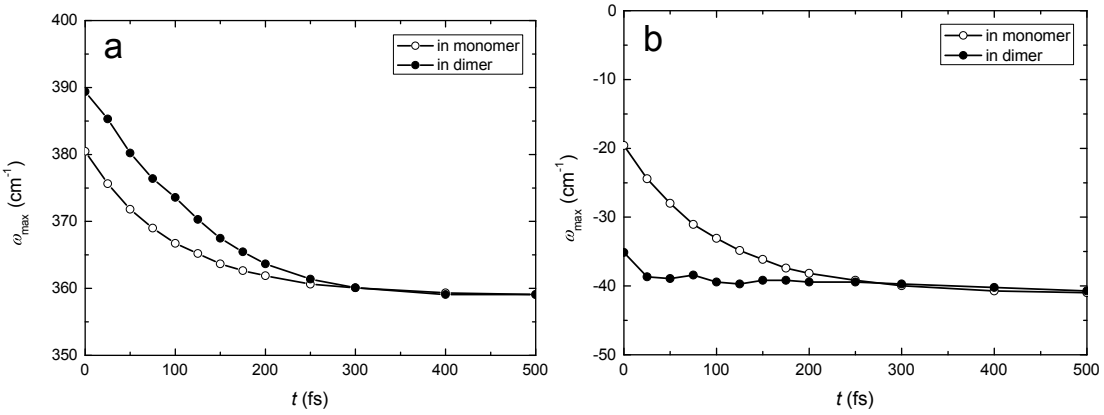

Figure 3.8 Peak analysis of the TRF spectra: frequencies of the maxima. The time dependence of the frequencies for the higher/lower peak (a/b) are shown. The full dots denote the position of the maximum within the dimer, while the empty dots show the position of the fluorescence maximum of the corresponding monomeric state.

monomeric counterpart, while at long times the peak positions coincide. The first effect is the result of the excitonic splitting. The fact that at long times both peaks have the same frequencies points to the suppression of the excitonic splitting. Bearing these results in mind we can see the analogy for the case of the lower peak Fig. 3.8(a). Namely, at short times the peak is "excitonically pushed" away to the lower frequencies, while at longer times the excitonic splitting is suppressed. This seems to be in accord with the suppression of the resonance interaction as given by Eq. (3.10).

Next, we plot the peak intensities against the waiting time in Fig. 3.9. As can be seen, the evolution is relatively "flat" with an initial oscillatory pattern. At later times the oscillations die out and the redistribution of the signal strength among the peaks becomes visible. The long-time behaviour is dictated by the population transfer, and the main reason for the apparently sluggish relaxation is the low temperature and relatively large energy gap. However, at early times the evolution is governed by other processes, two of which can be identified. Firstly, upon comparison with Fig. 3.7 (e.g., looking at the lower peak), we can attribute some loss of the signal intensity to the slight broadening of the peak. Secondly, we notice that both intensities are modulated by an in-phase oscillation with a period of $\approx 80\,\mathrm{fs}$.

In order to understand the evolution of the spectrum and the origin of various processes, we can look at the time evolution of the signal components, originating from different $R_j^{(i)}$ terms, and evaluate their contributions to the total TRF spectrum. The results are shown in Fig. 3.10. Initially, Fig. 3.10(a), apart from the trivial component $R^{(0)}$, only $R_1^{(1)}$ and $R_6^{(2)}$

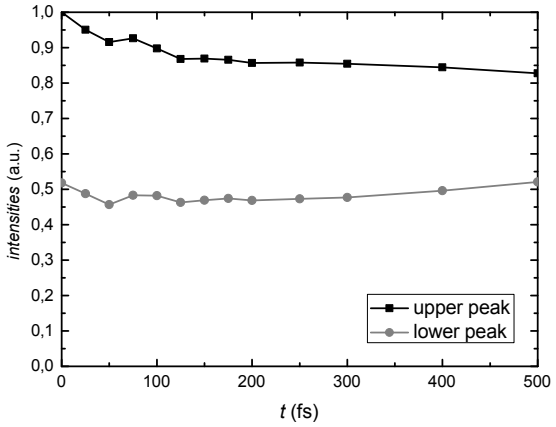

Figure 3.9 Peak analysis of the TRF spectra: amplitudes. The intensities are normalized to the amplitude of the upper peak at zero waiting time.

contribute to the signal. At later times, we can distinguish four types of diagrams: decaying ($R_6^{(2)}$), steady amplitude ($R_1^{(1)}$), growing and saturating ($R_{2,3}^{(1)}$ and $R_{1,2}^{(2)}$), growing indefinitely ($R_{3-5}^{(2)}$). By $t = 500\,\mathrm{fs}$, Fig. 3.7(b), and longer times, the saturating diagrams have attained their final shape and amplitude, and the signal is dominated by $R^{(0)}$, $R_1^{(1)}$ and $R_{3-5}^{(2)}$.

The described components contribute to the spectra in the following way. The $R_1^{(1)}$ and $R_6^{(2)}$ diagrams, as visible from Fig. 3.10(a), yield the oscillator strength redistribution and the excitonic splitting accordingly. The diagrams $R_2^{(1)} + R_3^{(1)}$ create an initially oscillating signal, which modulates the overall amplitude of $R^{(1)}$. The $R_3^{(2)}$ term corresponds to the population transfer *into* the fluorescing state. Therefore it has purely positive values, and the corresponding signal becomes stronger in time at lower frequencies. Similarly, the sum $R_4^{(2)} + R_5^{(2)}$ corresponds to the de-population of the fluorescing state, hence, it has negative values and yields stronger signal at higher frequencies. The diagrams $R_1^{(2)} + R_2^{(2)}$ seem to have a minor effect on the overall signal.

The analysis of the TRF signal in the presented method is greatly simplified by the fact that contributions from various diagrams of any order are simply additive. This has two important implications. Firstly, at time $t = 0$ the comparison of our method with the exciton theory can be used to evaluate the limits for the resonance coupling (with respect to the detuning ω_{ab}), which defines the applicability of the current scheme, conf. Fig. 3.6. Secondly, the additivity allows us to "dissect" the full spectrum into the components, which can be attributed to one or another process manifest in the overall time evolution. The redistribution of signal intensity and the peak-shift in the case of a weakly coupled molecular heterodimer can be

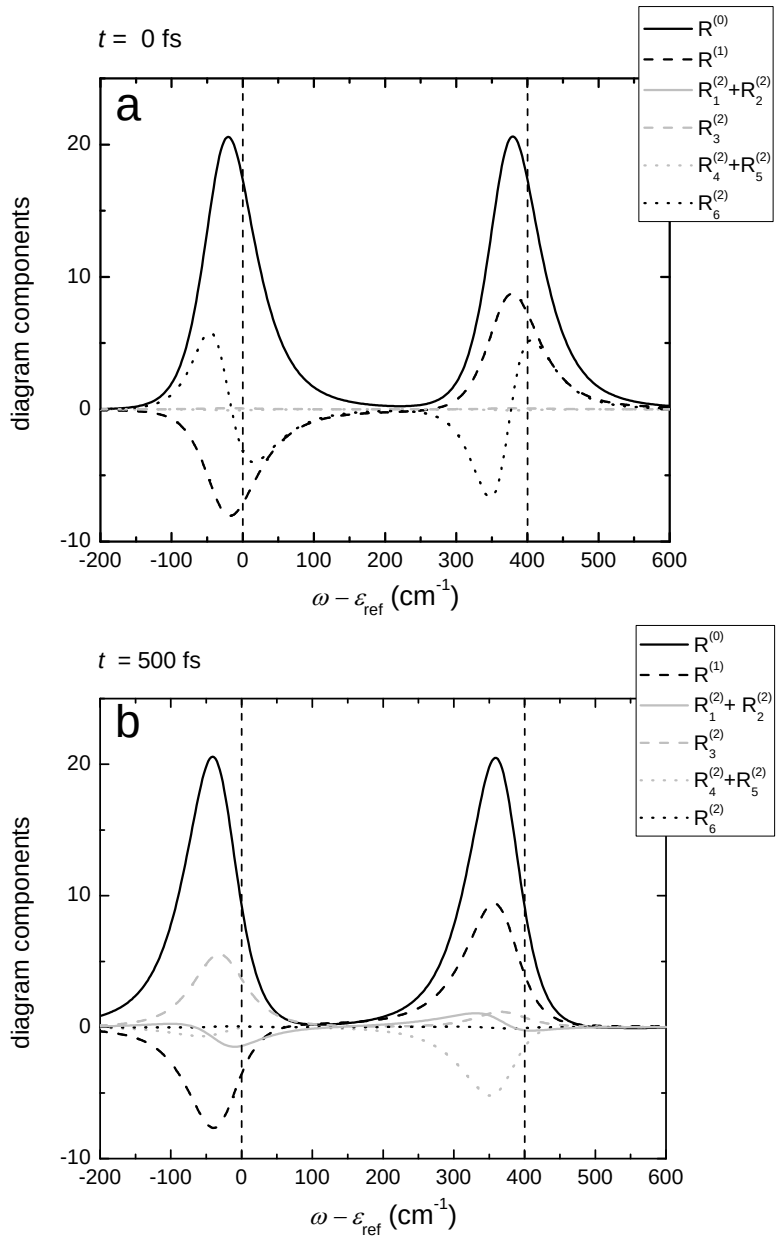

Figure 3.10 Evolution of signal components corresponding to different expansion terms $R_j^{(i)}$ of the response function. The contributing signals are calculated for (a) short times ($t = 0\,\mathrm{fs}$) and (b) long times ($t = 500\,\mathrm{fs}$). The first-order terms are summed for clarity and not shown individually, however, the $R_1^{(1)}$ term is dominant; $R^{(1)}$ in (a) entirely consists of this term. The summation $R_4^{(2)} + R_5^{(2)}$ is performed due to the fact that these diagrams are complex conjugate; the summation $R_1^{(2)} + R_2^{(2)}$ is performed for clarity mostly, because these two diagrams partly compensate each other.

examined as particular examples.

The time evolution of peak intensities, Fig. 3.9, reveals two major processes: the intensity redistribution and the in-phase oscillation of both peaks. We start with the latter effect by looking at the diagrams $R_2^{(1)} + R_3^{(1)}$, which are the apparent cause of the oscillation. Upon the inspection of Fig. 3.5, we notice that the system emits the signal while being in a coherent state. When two coherently excited levels emit to a common final state, the modulation of emission spectrum, the so-called quantum beat, is observed with the frequency equal to the energy difference between the levels. In the current case, the period of the oscillation (80 fs) is in agreement with the detuning $\omega_{ab} = 400\,\mathrm{cm}^{-1}$. The in-phase oscillation of both peaks would result in a modulation of the frequency-integrated signal, which is experimentally employed in the quantum beat spectroscopy [57]. Since the system is coupled to the bath, the coherences subsequently dephase and the oscillations cease.

The intensity redistribution is governed by the energy transfer process, which is in turn represented by the sum of the diagrams $R_3^{(2)} + R_4^{(2)} + R_5^{(2)}$. Bearing in mind, that the presented theory is based on the perturbative expansion in terms of the resonance interaction, one may again wonder about the relation between the current method and the FRET theory. Instead of making a direct comparison, we argue that the two approaches have essentially different starting points. The FRET approach is derived for the vibrationally relaxed donor state incoherently transferring energy to the vibrationally hot excited state of the acceptor. The outcome of such theory is the energy transfer rate, which is of the second order in J. In our case, the donor can be in any vibrational state and the coherent aspects of the transfer process are to some extent taken into account. The price to pay for these advantages is that now the amplitude rather than the rate is proportional to J^2. This introduces the restriction for the waiting time t, and our results should be trustworthy within the constraint $Jt \lesssim 1$. Besides that, it is interesting to mention, there are oscillations in the transfer diagrams as well (not shown). Unlike the oscillations visible in Fig. 3.9, the latter are of opposite phase for both peaks, which suggests the oscillatory evolution of the populations. However, because of their appearance in early times only, their contribution to the total signal is overwhelmed by the "stronger" diagrams.

The interpretation of the difference in the peak frequency evolutions, Fig. 3.8, is twofold. On the one hand, we notice from Fig. 3.10(a) that the diagram component $R_6^{(2)}$ is responsible for the effective excitonic splitting. However, this diagram is decaying in time due to the boundaries of the

integrals within its definition. Hence, from the technical point of view, the decay of $R_6^{(2)}$, and subsequently of the excitonic splitting, increases the red-shift of the upper peak and partly compensates the red-shift of the lower peak. On the other hand, the situation can be interpreted in physical terms by looking at the potential energy surfaces of the excited states, depicted in Fig. 3.11. In the case of slow bath (which is the current case due to $\gamma^{-1} = 100\,\mathrm{fs}$), initially, at $t = 0$, fluorescence and absorption spectra are identical, because there is no time for the reorganization dynamics to take place [40]. Therefore we can depict the fluorescence as the vertical transition from the potential energy surface of the excited state (dashed line), which does not coincide with its monomeric counterpart (full line) due to the resonance interaction. The frequency of the fluorescence in the long-time limit, $\omega_{\max}(t = \infty)$, in the current scheme indicates that the relaxed fluorescence takes place from the minima of the monomeric potential energy surfaces, $\varepsilon^0_{a/b}$. Which means that the current scheme describes two processes taking place at the same time: the vibrational relaxation (wiggly arrows) and the simultaneous renormalization of the potential energy surfaces due to the suppressed resonance interaction. This leads to the larger Stokes shift of the upper state, $\omega^{\mathrm{up}}_{\max}(t)$, and smaller one for the lower state, $\omega^{\mathrm{lo}}_{\max}(t)$.

In summary, as can be seen from the calculated spectra, the proposed theory is capable of reproducing the notable effects that would be anticipated in the TRF of an excitonic system: the excitonic splitting, oscillator strength redistribution and quantum beats. As mentioned previously, the long-time limit should be treated with caution. This includes both the population transfer rates and the complete localization of the excitations, as presented in Fig. 3.11. However, at early times or in the case of really small resonance coupling, the method allows to follow the system dynamics in greater detail and broader initial conditions than, e.g., the FRET theory. We also note, that the the perturbative treatment of the resonance interaction can in principle be extended to calculate the response functions in the case of more sophisticated non-linear spectroscopic experiments, such as the 2D PE spectroscopy.

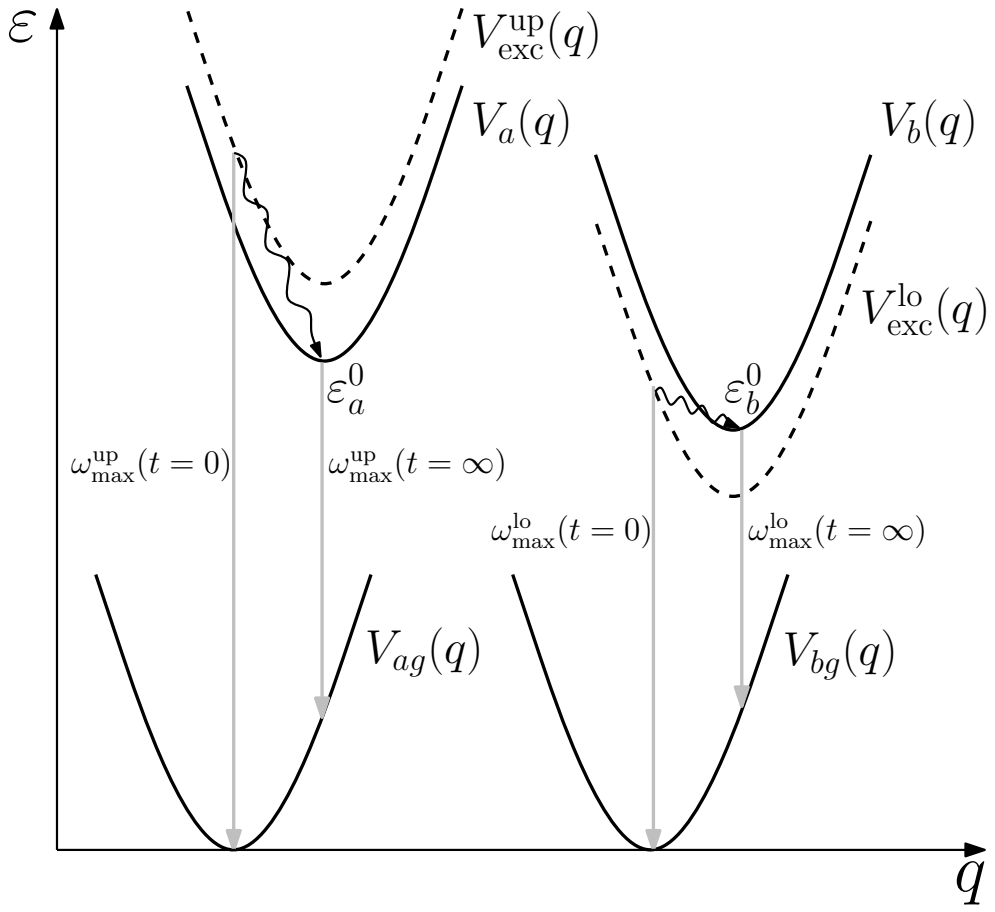

Figure 3.11 Interpretation of the time dependence of the TRF peak position. The potential energy surfaces of the ground and the corresponding excited states are shown in full lines. Due to the resonance coupling the excitonic splitting yields new, excitonic, potential energy surfaces, shown in dashed lines and denoted $V_{\mathrm{exc}}^{\mathrm{up/lo}}$ for the upper and lower excitonic states accordingly. The grey arrows indicate the fluorescence, while the wiggly arrows show the vibrational relaxation.

4. The intermediate resonance coupling regime

In this chapter, the coherent excitation dynamics is investigated in the intermediate resonance coupling regime (as compared to the system–bath interaction). In biological systems, such as the photosynthetic pigment–protein complexes, various interactions, especially the intramolecular couplings and the couplings to the phonon bath are of similar order: $J \approx \lambda$. In addition to that, the bath correlations are not decaying almost instantaneously as presupposed by the Markovian approximation. Under these conditions the usage of all the perturbative methods becomes questionable. Therefore we use the HEOM approach as a reference method in analysing an excitonic heterodimer.

Usually, a homodimer — a pair of identical chromophores — is used for considering various aspects of the coherent exciton dynamics and relaxation [27, 28, 31, 32]. In the discussions of a heterodimer system, the distinctness of constituent monomers is often limited to the excitation energies only [11, 58]. Some aspects which could be attributed to the heterodimer were also disclosed by analyzing the exciton–charge-transfer state mixing problems [33, 34]. Here, we consider the effects originated from the differences in both the excitation and the reorganization energies of the constituent molecules of the heterodimer. Particularly, we examine the effects of the asymmetry in reorganization energies in Section 4.1, then discuss the signs of the breakdown of the exciton concept in Section 4.2. In Section 4.3 we investigate the thermalization dynamics in the case of non-Markovian bath correlation. Finally, in Section 4.4 we make some notes on the RDO propagation schemes based on the given findings.

4.1. Influence of the asymmetric reorganization energies on the excitation dynamics

The main parameter characterizing a heterodimer is the difference of site energies, or simply the energy gap. On the one hand, the energy gap is a crucial parameter in describing the excitonic mixing of states, conf. Eq. (2.15). On the other hand, it determines the asymptotics of the evolution, namely the thermal equilibrium conditions. However, upon the asymmetry in reorgan-

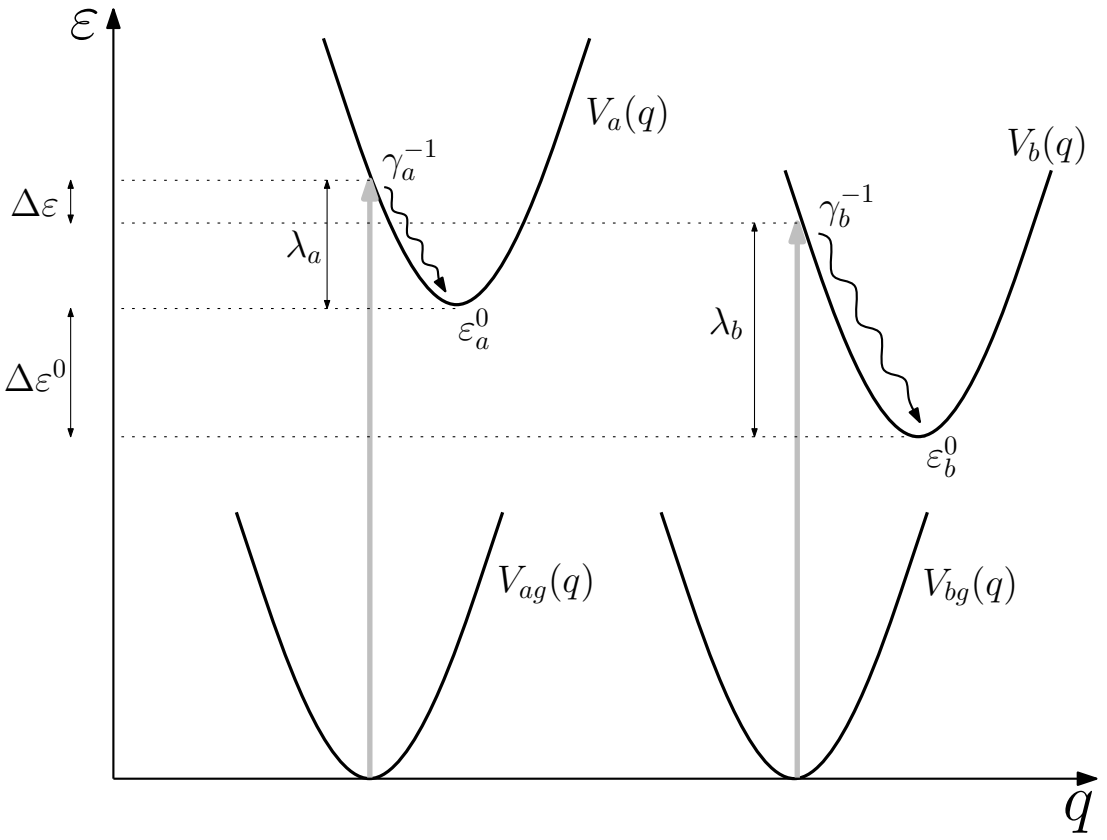

Figure 4.1 Potential energy surfaces of the monomers constituting an excitonic heterodimer. Different displacements of the excited state potential energy surfaces yield different reorganization energies.

ization energies, $\lambda_a \neq \lambda_b$, the energy gap becomes an ambiguous concept. As shown in Fig. 4.1, two non-equivalent definitions of the energy gap in the one-exciton manifold can be given: we can define it either as $\Delta\varepsilon = \varepsilon_a - \varepsilon_b$ or as $\Delta\varepsilon^0 = \varepsilon_a^0 - \varepsilon_b^0$ (even though the relation $\Delta\varepsilon = \Delta\varepsilon^0 + \lambda_a - \lambda_b$ holds). Evidently, these two cases contain different physical meanings.

Since the energy ε_i refers to the Franck–Condon transition region of the i-th potential energy surface (grey vertical arrows in Fig. 4.1), $\Delta\varepsilon$ corresponds to the distance between the peak positions in the absorption spectra. Therefore we can loosely call it the "optical energy gap". This has a perfectly clear meaning in the absorption spectroscopy, however, the thermal equilibrium does not establish itself with respect to this energy gap. Should the resonance coupling be simply perturbative, we could expect the thermalization with respect to $\Delta\varepsilon^0$ as the first approximation. Since this gap enters the FRET theory [4, 39] we shall call it the "Förster energy gap".

We will now study the dynamics of the excitation in the given system by means of the Redfield equations and the HEOM. We consider the excitation of the dimer by a broad-band optical pulse, which is much shorter

than the time scale of the relaxation dynamics. By setting the transition dipole moments μ_{ag}, μ_{bg} appropriately, one of the constituent monomers can be considered a donor for further excitation transfer ($\mu_{ag} = 1$), while the other one is treated as an acceptor ($\mu_{bg} = 0$). Hence, the initial condition for the evolution of the RDO in the site basis is given by $\rho_{ij}(0) = \delta_{ij}|\mu_{ig}|^2$ ($\rho_{aa}(0) = 1$, while other elements are zero). We note that, by switching into the exciton representation, both single-exciton states are initially populated, which weakens the distinction between the donor and the acceptor, yet in the non-degenerate case, $\Delta\varepsilon \neq 0$, the character of a state can still be distinguished. The constant parameters used in the calculations are the following: $T = 300\,\mathrm{K}$ (which corresponds to $k_\mathrm{B}T \approx 208\,\mathrm{cm}^{-1}$), $J = 100\,\mathrm{cm}^{-1}$, $\gamma^{-1} = 100\,\mathrm{fs}$. The tunable parameters are the reorganization energies λ_a, λ_b, given as four combinations of the values $30\,\mathrm{cm}^{-1}$ and $150\,\mathrm{cm}^{-1}$, and the gap between the site excitation energies, either the "optical" or the "Förster", with value $+100\,\mathrm{cm}^{-1}$ ("+" indicates the donor state being above the acceptor).

The results are shown in Fig. 4.2. For now we concentrate on the top row, which represents the HEOM results ((a) and (b)), and the middle row, which represents the Redfield results ((c) and (d)). The left column corresponds to $\Delta\varepsilon = +100\,\mathrm{cm}^{-1}$ as a fixed energy gap, while the right column corresponds to $\Delta\varepsilon^0 = +100\,\mathrm{cm}^{-1}$ being fixed. In the right-hand column the initial values are scattered simply because fixing $\Delta\varepsilon^0$ with different λ's gives us different $\Delta\varepsilon$ used in the definition of the excitonic basis.

First, consider the amount of energy dissipated in each exciton state during the vibrational relaxation. Let us denote this by the exciton reorganization energy. We would expect that for the fixed optical energy gap, in the case of $\lambda_a = \lambda_b$ an equal amount of energy associated with each state will be dissipated, and therefore the equilibrium populations will not depend on λ_a (or λ_b): the exciton levels will shift by the same amount. This coincides exactly with the result of the Redfield equations (full lines, Fig. 4.2(c) and (d)), but not with the HEOM results. The latter point to the action of the bath upon the systems, which is discussed in detail in the following Section 4.2. In the non-trivial case of $\lambda_a \neq \lambda_b$ [34], the vibrational relaxation would shift the exciton levels by a different amount ($\Delta\varepsilon^0 \neq \Delta\varepsilon$), and equilibrium populations will depend on λ_a and λ_b. This effect is apparently captured by both the HEOM and the full Redfield schemes (dashed lines in Figs. 4.2(a) and (c)). The energy gap between the states, as inferred from the equilibrium population values, is effectively decreased (grey-dashed lines) or increased (black-dashed lines). We also note the failure of the Red-

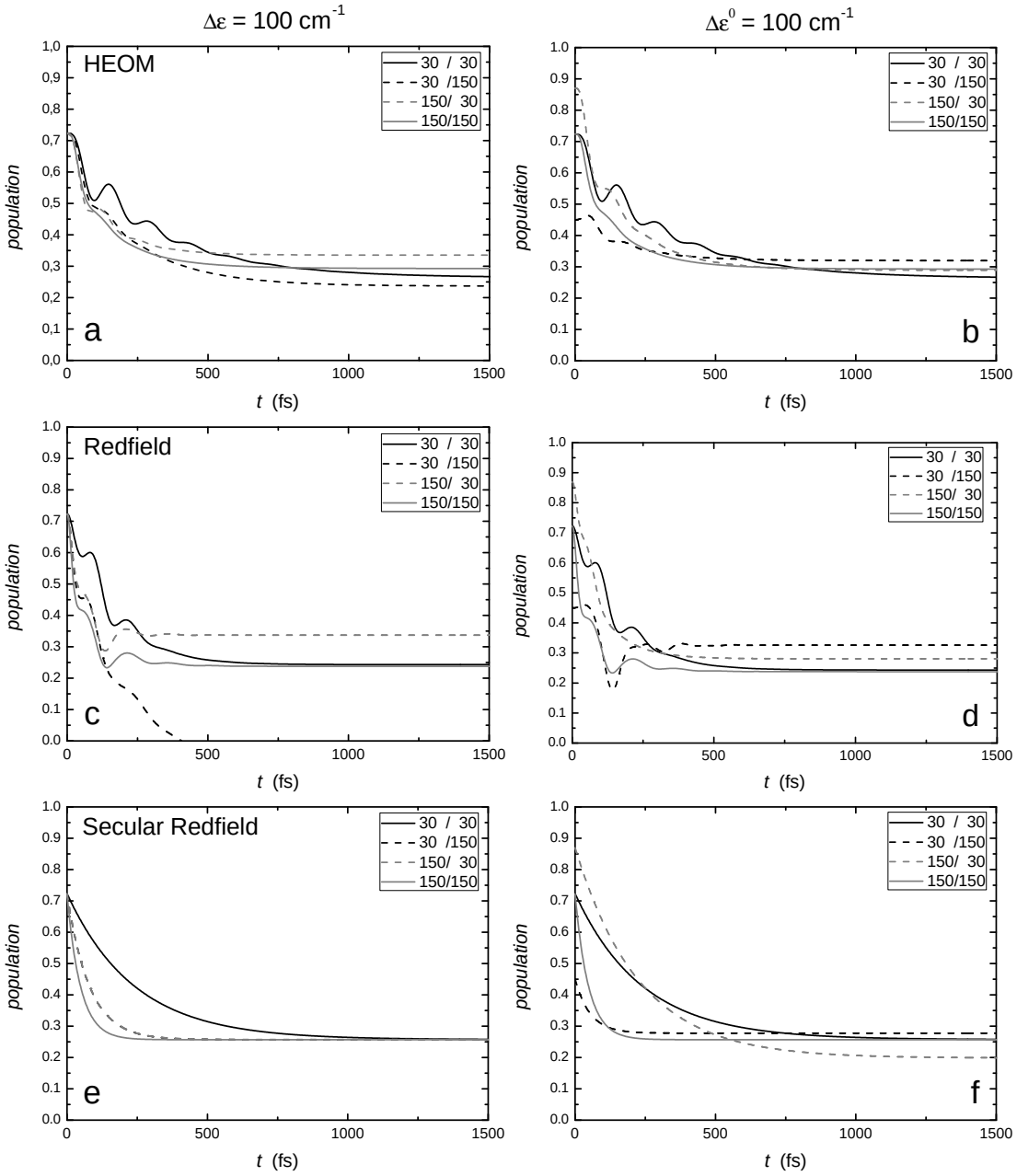

Figure 4.2 Evolutions of the higher excitonic state population. The insets show the combination of reorganization energies given in the form λ_a/λ_b ($\mathrm{cm}^{-1}/\mathrm{cm}^{-1}$). The left column corresponds to $\Delta\varepsilon = +100\,\mathrm{cm}^{-1}$, the right one — to $\Delta\varepsilon^0 = +100\,\mathrm{cm}^{-1}$. (a) and (b), (c) and (d), (e) and (f) correspond to the HEOM, the full and the secular Redfield equations, respectively.

field scheme in Fig. 4.2(c).

Consider now the case of a fixed Förster energy gap. Note that the optical energy gap is now the function of $\lambda_a - \lambda_b$. One would expect that $\Delta\varepsilon^0$ governs the equilibrium populations of excitons. However, the equilibrium populations in both the HEOM and the full Redfield schemes (Fig. 4.2(b) and (d)) are related to neither $\Delta\varepsilon$ nor $\Delta\varepsilon^0$: this shows a complex mixing of the monomeric reorganization energies, which defines an effective counterpart of the Förster gap in the excitonic basis, $\Delta_{\mathrm{e}}\varepsilon^0$. All possible configurations of λ's for the fixed Förster energy gap are schematically shown in Fig. 4.3. When $\lambda_a = \lambda_b$ (top panel), the optical energy gap and the Förster energy gap coincide and the reorganization energies of both excitons are identical, and the energy gap between the relaxed exciton states can be obtained by the transformation to the exciton basis, $\Delta_{\mathrm{e}}\varepsilon^0 = \Delta_{\mathrm{e}}\varepsilon$. The middle panel demonstrates the case $\lambda_a \neq \lambda_b$, where the exciton reorganization energies come from the nontrivial mixing of λ_a, λ_b and $\Delta\varepsilon$. Hence, the Förster energy gap alone can be a poor benchmark for assessing the equilibrium populations. The bottom panel reveals the peculiar situation, where the exciton states are swapped in comparison with the monomeric states (both initially and in the long-time limit). The corresponding population evolution is represented by the black-dashed line in Figs. 4.2(b) and (d): the initial population (< 0.5) indicates that the higher excitonic state originates form the "acceptor" state in the site basis.

4.2. Breakdown of the exciton concept

The HEOM solutions (Fig. 4.2(a) and (b)) and the results that follow from the Redfield equations look qualitatively similar. However, an unexpected feature is the difference between equilibrium population values for the case when $\lambda_a = \lambda_b$, which again tells us about different energy gaps in each case. This points to the action of the bath upon the system. Indeed, we find that the conventional excitonic basis is approximate.

So far we have treated the excitonic states, defined by Eq. (2.12), as the eigenstates of the system. However, HEOM solutions in the excitonic basis, as given above, exhibit non-vanishing steady state coherences. The presence of the steady state coherences can be interpreted as a reflection of renormalization of the system eigenbasis [59] taking place in the course of time. Contrary to the Redfield scheme, HEOM is not subject to any specific predefined basis, even though the equations are originally formulated using the projectors onto the site basis. Therefore, it allows us to identify the

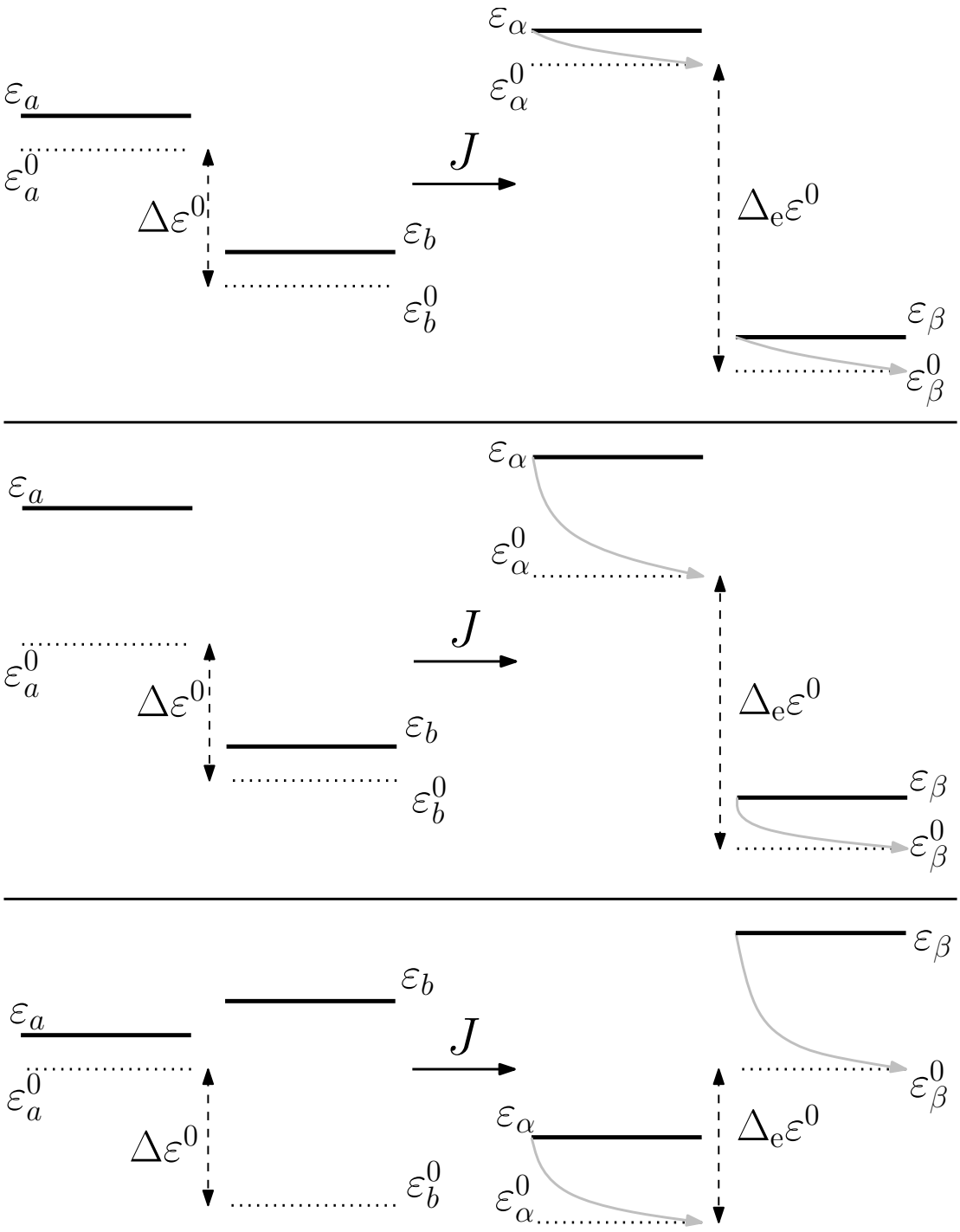

Figure 4.3 Schematic representation of the Förster energy gap in the presence of the resonance coupling. Monomeric units with identical $\Delta\varepsilon^0$ are shown on the left. The grey arrows on the right represent the vibrational relaxation, which defines the effective Förster energy gap in the excitonic basis, $\Delta_e\varepsilon^0$. The top row corresponds to $\lambda_a = \lambda_b$, the middle and the bottom ones — to $\lambda_a > \lambda_b$ and $\lambda_a < \lambda_b$ accordingly.

so-called preferred basis [60], in which the density matrix is diagonal in the long-time limit. This can be obtained by diagonalizing the stationary part of the solution in the excitonic basis. Representing the RDO in the preferred basis for the fixed $\Delta\varepsilon$ configuration has the effect of shifting the equilibrium population values. Their order, however, remains the same as in the excitonic basis. Meanwhile for the fixed $\Delta\varepsilon^0$ configuration, we have not just quantitative but also qualitative changes in comparison with Fig. 4.2(b). Evidently, the solutions for $\lambda_a \neq \lambda_b$ configurations now converge into the same steady state value, which is in-between the ones for equal reorganization energies. This shows that the energy gap determining the equilibrium population values depends on the sum of the reorganization energies rather than their individual values.

Establishing the preferred basis by diagonalising the density matrix after it reaches equilibrium has led to the conclusion, that a good measure of the action of the bath is an effective resonance coupling J_{eff}. It has been used to replace the original J value with to reproduce the effective energy gap defined by the thermal equilibrium in the preferred basis [30]. The effective system properties are a well known concept from the solid state theory [61], and suppressed resonance coupling was already mentioned by considering the manifestation of dynamical exciton localization in the spectral properties of photosynthetic reaction centres [33, 34]. In our case, it appears that the connection between the original resonance coupling and the effective one resembles the so-called small polaron transformation [62]. The empirical form of the effective resonance coupling was found to be [30]

$$J_{\text{eff}} = J \exp\left(-A\frac{\lambda_a + \lambda_b}{k_{\text{B}}T}\right), \tag{4.1}$$

where the constant A was found by the authors to be 0.15.

4.3. Optimal energy gap in the non-Markovian regime

It has been shown that in the region of intermediate and strong reorganization energies, the Redfield equations describe the energy transfer rates inadequately, because these rates become independent of the reorganization energies [58]. This is explained by the fact that the Redfield equations do not capture the reorganization of the phonon modes, which in turn comes from the Markov approximation. To study the approach to the intermediate regime in the case of Markovian and non-Markovian dynamics, we use the HEOM method. Additionally, we use the FRET theory for compar-

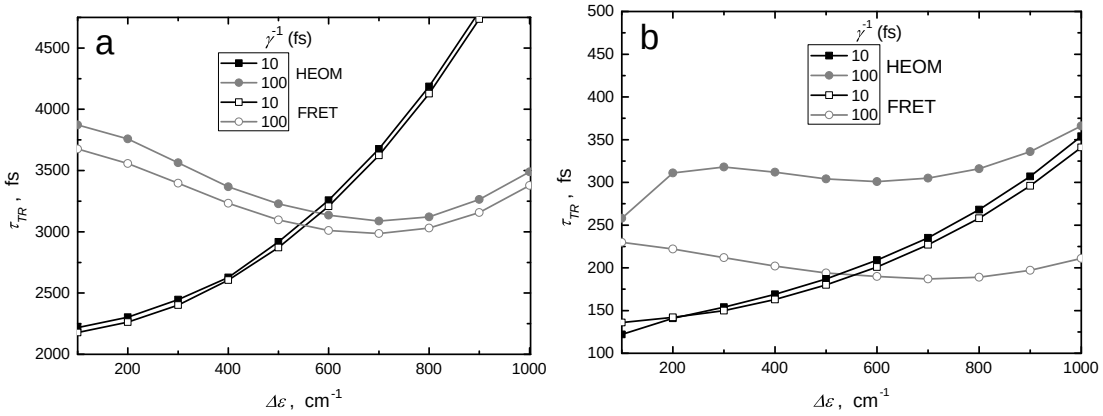

Figure 4.4 Comparison of thermalization times given by HEOM and FRET schemes for different energy gaps. For the sake of consistency, all the rates were extracted from the evolution of RDO by numerical fitting. Two cases of resonance coupling correspond to: (a) $J = 20\,\mathrm{cm}^{-1}$; (b) $J = 80\,\mathrm{cm}^{-1}$.

ison, which provides the upward and downward population transfer rates, k_{ab}, k_{ba}, for the master equation Eq. (2.39), which takes the form

$$\begin{cases} \dot{\rho}_{aa} = - \quad k_{ab}\,\rho_{aa} \;+\; k_{ba}\,\rho_{bb}; \\ \dot{\rho}_{bb} = \qquad k_{ab}\,\rho_{aa} \;-\; k_{ba}\,\rho_{bb}. \end{cases} \tag{4.2}$$

We investigate the time scale of the thermal relaxation (TR), $\tau_{\mathrm{TR}} = (k_{ab}+k_{ba})^{-1}$, which is obtained by solving the HEOM and subsequently performing numerical fitting by means of the least square routine. We examine the cases of parameters mostly relevant for the FRET regime, $\lambda \gg J$. Taking $\lambda_a = \lambda_b = 400\,\mathrm{cm}^{-1}$ let us consider the cases of $\lambda/J = 20$ ($J = 20\,\mathrm{cm}^{-1}$), which is fully consistent with the FRET regime, and $\lambda/J = 5$ ($J = 80\,\mathrm{cm}^{-1}$), which reflects the breaking of the validity of FRET. The calculated dependence of τ_{TR} on the energy gap between the monomers is shown in Fig. 4.4. Calculations at temperature 300 K ($\beta^{-1} \approx 208\,\mathrm{cm}^{-1}$) are performed for two different values of $\gamma^{-1} = \gamma_a^{-1} = \gamma_b^{-1}$: 10 fs and 100 fs. We omit the case when the energy gap is $\Delta\varepsilon = 0\,\mathrm{cm}^{-1}$, because the dynamics in that case are not given by the FRET scheme due to the degeneracy of monomer energies.

In the case of small resonance coupling and fast correlation decay of the bath (black squares, Fig. 4.4(a) the monotonic rise in the TR time is obtained upon the increase of the energy gap. This is an intuitively clear picture of thermalization and corresponds to a Markovian regime of the bath relaxation. In this case the transfer rates predicted by HEOM and FRET almost match each other. When we switch to the slow correlation decay of the bath (grey dots), the dependence changes. Now an optimal system

configuration for the excitation transfer around $\Delta\varepsilon \approx 700\,\mathrm{cm}^{-1}$ is well distinguished. This is a non-Markovian regime of the bath dynamics, and the HEOM and FRET predictions are *qualitatively* identical. The FRET approach thus properly describes the parameter regime $\Delta\varepsilon \gg J$ and $\lambda \gg J$. We note that the dependence $\tau_{\mathrm{TR}}(\Delta\varepsilon)$ is symmetric around $\Delta\varepsilon = 0$ because the TR rate, being the sum of the upward and downward rates $k_{ab} + k_{ba}$, is invariant under the change of the sign of $\Delta\varepsilon$.

In the case of larger resonance coupling, Fig. 4.4(b), the relaxation is substantially faster, as should be expected. Another difference is visible in the HEOM results when energy gaps are $\Delta\varepsilon \leq 300\,\mathrm{cm}^{-1}$. The decrease of τ_{TR} for smaller energy gaps is the manifestation of the excitonic delocalization effects. For larger gaps both HEOM and FRET have an optimal energy gap configuration in the non-Markovian regime. While the absolute difference in τ_{TR} values calculated by HEOM and FRET is similar as in Fig. 4.4(a), the relative difference between them in the non-Markovian regime now becomes significant. However, the FRET approach still gives a reasonable prediction. There are two more points to mention which are not shown here explicitly. The first one is that the rate $k_{ab} + k_{ba}$ does not depend on individual reorganization energies, but rather on their sum $\lambda_a + \lambda_b$. The second one is that the speed-up seen in the non-Markovian regime diminishes upon decreasing $\lambda_a + \lambda_b$.

Our calculations of the thermalization dynamics reveals the existence of an optimal energy gap that depends on the system–bath coupling and the relaxation time scale of the bath correlations. Similar results demonstrating the speed-up of the energy transfer upon increasing the value of $\Delta\varepsilon$ in a certain region have also been previously demonstrated [63, 64]. For better understanding of its origin, let us start the consideration from the case of the small resonance coupling, when the site and the excitonic bases almost coincide and the results of HEOM and FRET are directly comparable. This allows us to follow the details of the energy gap dependence of the excitation transfer in terms of FRET, where the transfer rates have an explicit form. Namely, they are proportional to the overlap of the donor emission and acceptor absorption profiles, Eq. 2.40. The profile functions for the transitions $|g_i\rangle \rightarrow |e_i\rangle$ define the absorption/emission line-shapes in the various bath regimes separated by values of a corresponding dimensionless modulation parameter $\chi = 2\lambda/\beta\gamma^2$ [40]. Fig. 4.5(a) demonstrates absorption (black line) and emission (grey lines) profiles for different displacements $\Delta\varepsilon$ of the donor in the case of $\gamma^{-1} = 10\,\mathrm{fs}$ (fast bath). Parameter $\chi = 0.59$ is close to the fast modulation (homogeneous) limit $\chi \ll 1$, which

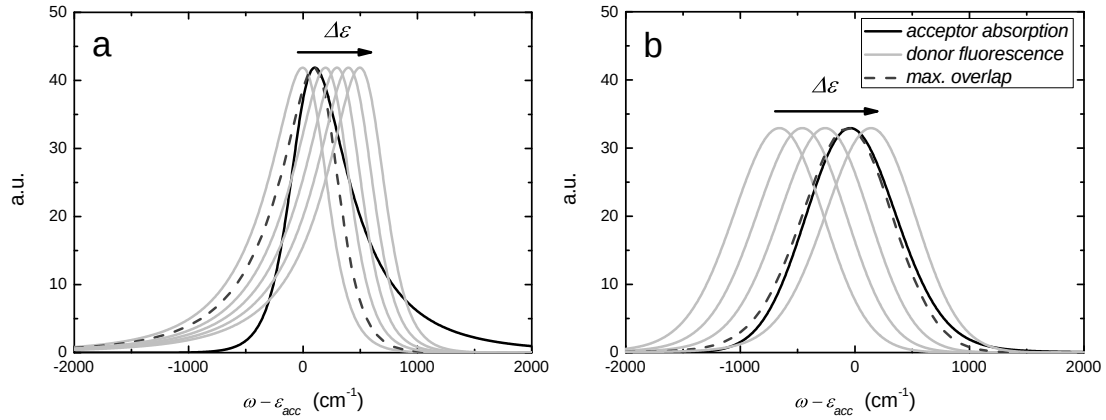

Figure 4.5 Emission/absorption profiles of the donor and the acceptor in the case of: (a) fast bath; (b) slow bath. Absorption of the acceptor (black line) is fixed, while the donor emission profiles (grey) are given for different energy gaps. The donor is above the acceptor, and the values of $\Delta\varepsilon\,(\mathrm{cm}^{-1})$ read (left to right): a) 100, 200, 300, 400, 500, 600; b) 100, 300, 500, 700, 900. The emission profile producing the maximal overlap with the absorption profile is given by dashed lines; note that it does not exactly match the optimal $\Delta\varepsilon$ and is given for the purpose of illustration only. Frequency is centred around the maximum of the acceptor absorption.

manifests in Lorentzian profiles and the absence of the Stokes shift [30]. In Fig. 4.5(b) the same situation is depicted for the case of $\gamma^{-1} = 100\,\mathrm{fs}$, which corresponds to $\chi = 59$. Condition $\chi \gg 1$ is known as the slow modulation (inhomogeneous) limit, and it manifests in Gaussian profiles and a clearly developed Stokes shift [30]. The interpretation of relaxation rates in terms of Fig. 4.5 is the following. In the Markovian bath regime there is little-to-none Stokes shift, and the donor fluorescence yields the best overlap with the acceptor absorption at small $\Delta\varepsilon$. Whereas in the non-Markovian regime, there is a Stokes shift close to its maximum of 2λ that needs to be compensated by displacement $\Delta\varepsilon$ to yield the maximum overlap. This is shown in Fig. 4.4(a), where the energy gap for optimal relaxation in the case of slow bath is close to $\lambda_a + \lambda_b$ [64].

The case of the relatively large resonance coupling, 4.4(b), demonstrates similar dependencies even though the relative difference between HEOM and FRET is considerable in the case of the slow relaxation of the bath correlation. The main difference other than the globally increased rates, is the speed-up in the region of $\Delta\varepsilon$ where the excitonic mixing is significant. It is interesting to note, that the transfer rates actually depend on the energy gap between the relaxed states $\Delta\varepsilon^0$ (conf. Fig. 4.1) as opposed to $\Delta\varepsilon$. In the case of different reorganization energies, $\Delta\lambda = \lambda_a - \lambda_b \neq 0$, the following consequences arise. If the resonance coupling is small, the two energy gaps

are simply mutually shifted by $\Delta\lambda$. The relaxation time should then be plotted as a function of the gap $\Delta\varepsilon^0$, and the decrease in $\tau_{\mathrm{TR}}(\Delta\varepsilon^0)$ that is now centred at $\Delta\varepsilon^0 = 0$, would be centred at $\Delta\varepsilon^0 = \Delta\lambda$. However, if the resonance coupling is large, the relation between $\Delta\varepsilon^0$ and $\Delta\varepsilon$, or rather $\Delta_{\mathrm{e}}\varepsilon^0$ and $\Delta_{\mathrm{e}}\varepsilon$, is no longer that simple, as shown in Section 4.1.

4.4. Comparison of propagation schemes in the intermediate coupling regime

In the light of the results from the previous sections, we can discuss the applicability and validity of various schemes in describing the energy transfer in the intermediate coupling limit. It must be noted that certain drawbacks of the methods applied above have been recognized and documented. For instance, the positivity problems of the Redfield equations is a known issue [59], and the failure of the method in the reorganization dynamics has been discussed [58, 63]. In addition to that, many more methods, such as the Lindblad equations in its original [65] and modified forms [66, 67], the modified Redfield [63] and others [22,68,69], have been suggested. Therefore we would like to point out several additional peculiarities that follow from our study.

Despite being plagued by the positivity problems, the Redfield equations have been one of the standard tools to study excitation dynamics in the pigment-protein complexes for some time, and moreover, they are well documented in textbooks [9, 39, 51]. We can asses the validity of the method by looking at Fig. 4.2, and comparing it to the HEOM. The equal reorganization energies (full lines) serve as a good starting point for comparison of the methods. As we can see, the initial stages of the Redfield and HEOM solutions ($\sim 100\,\mathrm{fs}$) look very similar, while the rates of the thermalization and the frequencies of the coherent oscillations are different (the coherent oscillations are more dramatic but shorter-lived when using the Redfield theory). Moreover, different methods give us different equilibrium population values, and within the HEOM approach the latter do not coincide for two pairs of identical λ's, as discussed above. This tells us that the Redfield equations, even though they are designed for the weak system–bath interaction, provide a fair qualitative description of the dynamics when the inter-chromophore and system–bath coupling strengths are comparable. However, quantitatively the Redfield results are far from conclusive.

The non-trivial case of different reorganization energies (dashed lines)

reveals the well-known problem of the Redfield scheme, namely, that it does not guarantee positivity. The increase of the energy gap is seemingly the reason for the failure of the Redfield scheme. At this point we can take a look at the solutions of the secular Redfield scheme, which was actually introduced in part to avoid the negative populations. Indeed, the solutions do not suffer from this problem, however they are both qualitatively and quantitatively different from both the HEOM and the full Redfield. In this case all four λ combinations give relaxation to the same equilibrium position. The equilibration is fully determined by the optical energy gap $\Delta\varepsilon$ and does not depend on $\lambda_a - \lambda_b$, which shows the failure of this approach when $\lambda_a \neq \lambda_b$. The dynamics modelled by the secular Redfield scheme in the case of a fixed Förster energy gap, Fig. 4.2(f), again follow the optical energy gap. Hence, we are to conclude, that the secular approximation is not a suitable tool for expanding the applicability of the Redfield scheme.

There are several remarks to be made about the HEOM as well. The question is: what price needs to be paid for the method being exact? The answer is twofold, and it starts with the somewhat "technical" aspects. Firstly, similarly to all the exact methods, HEOM is numerically very expensive, as the number of ADOs, required for a converged result, grows rapidly with the number of chromophores, which in turn boosts the memory requirements and the computation time. Setting aside the computational issues, another problem is the intrinsic dependence of the form of the equations on the form of the spectral density. Every model of spectral density requires a (re)derivation of the explicit form of the equations due to a specific decomposition of the correlation function, Eq. (2.58). And last but not least, the interpretation of the results, provided by the HEOM, is somewhat challenging, if an underlying physical mechanism of some process need to be established. Both the Redfield scheme and the FRET have a well understood picture of the underlying physics, while the HEOM lack it. The results of Section 4.3, namely, the ability of the FRET to explain the energy-gap-dependent speed-up in thermal relaxation, which is of course captured by HEOM as well, nicely illustrates the situation. Hence, it seems that the perturbative approaches, even though flawed in some situations, but capable of providing insights into the exact evolution, should not be completely disregarded.

5. Relaxation to the ground state in an excitonic system

The influence of the excitonic effects in the energy transfer is studied mostly within the single-excitation manifold. This is based on the assumption that the time scales of energy transfer and relaxation to the ground state are well separated. This is true in many cases of interest as the typical transfer times are in the range of femto- to picoseconds, while the excited state lifetime can be as long as nanoseconds. In turn this is due to the typical energy gaps to the first excited state being larger than $k_{\mathrm{B}}T$ by orders of magnitude. Therefore it is assumed, that the only coupling channel from the ground state to the excited state (or vice versa) is opened by the action of the electric field, i.e., the transitions from/to the ground state are possible only through optical pumping/emission. However, in certain problems the *relaxation to the ground state* (RGS) is of both interest and importance. One particular case is a process in the plant photosynthesis, known as the non-photochemical quenching, which is briefly introduced in the Section 5.1. To address one of the possible mechanisms of this process, we analyse the RGS in the heterodimer in Section 5.2, using the results from the previous chapter as well. We apply our calculations for experimentally studied model systems, called carotenoid–phthalocyanine dyads, in Sections 5.3 and 5.4.

5.1. Non-photochemical quenching in plant photosynthesis

The photosynthetic light-harvesting complexes are responsible for collection of solar energy and its subsequent delivery to the reaction centre, where this energy is stabilized in the form of a trans-membrane electrochemical potential [3,4]. Chlorophylls (Chls) and carotenoids (Cars) are the most abundant pigment molecules assembled in these complexes, which are responsible for all the light-induced processes in plants. In addition to the principle role of delivering the absorbed light energy to the reaction centre, the light-harvesting complexes from plant photosynthesis, namely from the PSII, are also involved in self-protection and regulation of the excitation density depending on the excitation conditions (see [70] for a recent review). The Car

molecules play the self-protection role against the triplet state formation on Chl molecules. Population of the triplet states on Chl molecules is possible as a result of intersystem crossing from the singlet excited states, which play the major role in the light-harvesting processes. Being in the triplet state Chl molecules contain sufficient energy to convert ground state triplet molecular oxygen to an excited singlet state, known to be destructive to the surrounding medium. Formation of singlet oxygen is inhibited by Car molecules as they accept Chl triplets through triplet energy transfer and the resulting Car triplet excitation is energetically too low to excite singlet oxygen [71]. In addition to such self-protection mechanism caused by the triplet state transfer from Chl to Car molecules, a further mechanism responsible for the excitation density control in oxygen generating PSII is invoked. This regulatory mechanism termed as *non-photochemical quenching* (NPQ), ensures a high efficiency and robustness of plant photosynthesis under fluctuating light, even at very high intensities.

Though the significance of NPQ in green plants is well identified, the exact nature of the underlying mechanism still remains a matter of debate [70]. Of the many proposed NPQ mechanisms several involve Car molecules — xanthophylls. One proposed mechanism is based on the assumption that a radical [72] or a charge-transfer state of a Chl–Car pair [73, 74] may be responsible for NPQ. According to later spectroscopic observations Lutein 1 in LHCII has been identified as a strong candidate to be responsible for the feedback de-exitation, which is the main component of NPQ [75]. More recently [76] a complex charge transfer state involving Lutein 1 and two Chls as an intermediate state in quenching by Lutein 1 has been identified. The notion of lutein (or another Car) as a quencher is attractive in part due to the fact that it possesses a very short ($\sim 10\,\mathrm{ps}$) excited state lifetime. Interestingly, according to recent model simulations, the excitation quenching mechanism at the heart of NPQ should be very fast, possessing a characteristic time of a few ps or even less [77]. Alternatively, the modulation possibility of interactions between Cars and Chls [78] or the energy position of the Car molecule interacting with Chls [79] might be attributed to the quenching ability of Chl dimers due to changes in their mutual interaction driven by an anisotropic polar environment.

Since the possible role of the Car molecule in the NPQ process remains unsettled, additional studies of the excitation dynamics in the artificial dyads composed of covalently linked Car and zinc phthalocyanine (Pc) molecules, Fig. 5.1, have been performed [35–37, 80]. The experimental data provide means to observe the energy transfer pathways in a structure similar

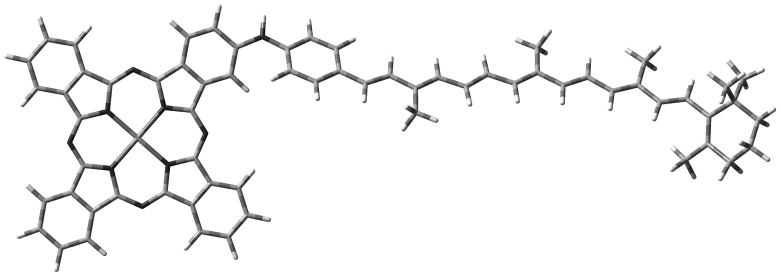

Figure 5.1 Carotenoid–phthalocyanine dyad.

to the Car–Chl dimer without the complementary effects of the surrounding pigments and the protein scaffold. The conclusions drawn from the energy gap dependence of various relaxation time scales serve as an inspiration to perform a rigorous modelling based on the quantum relaxation theory. To describe the excitation evolution of the dyads composed of covalently linked Car and Pc molecules, the evolution of a molecular heterodimer can be considered by assuming that one monomer (Car molecule in this case) is responsible for excitation quenching. Such quality arises when the spontaneous decay time τ_{Q} of the chosen monomer is comparable to the excitation energy transfer time. Indeed, the evolution of the excitation in such systems reveals two characteristic time scales [81]. The first one arises from the thermal relaxation (TR), discussed in the previous chapter, while the second one — from the RGS. In the next section, we examine the two processes and their interplay as a function of the resonance coupling, the interaction with the thermal bath and, most importantly, the energy gap between the monomeric excited states in the weak-to-intermediate resonance coupling regimes, which seem to be appropriate judging by the results obtained for the dyads (especially, [35]). To cover a broad scope of dynamical regimes of the model system under consideration, we use the HEOM method. Since the properties of the constituent monomers can be matched to those of Car S_1 and Chl/Pc Q_{y} electronic states, we are able to give a comprehensive interpretation of excitation dynamics in the dyads and make the conclusions about the possible sensitivity to characteristic parameters of the system and, thus, about the mechanism of energy dissipation.

5.2. Energy transfer and quenching in an excitonic heterodimer

In order to describe the RGS in an aggregate, we must add a corresponding superoperator to the Eq. (2.54):

$$\frac{\mathrm{d}}{\mathrm{d}t}\hat{\rho}(t) = -\mathrm{i}\mathcal{L}_{\mathrm{S}}\hat{\rho}(t) + \mathcal{D}\hat{\rho}(t) + \mathcal{K}\hat{\rho}(t). \tag{5.1}$$

The RGS superoperator is defined as $\mathcal{K}\bullet \Leftrightarrow -\sum_i \frac{\kappa_i}{2}\{\hat{Q}_i, \bullet\}$, where κ_i is the decay rate of the ith excited state. Parameters κ_i can be phenomenologically defined in the site basis [81]. The form of the RGS superoperator guarantees that the diagonal elements of the RDO (the populations) $\rho_{ii}(t)$ decay with the rates κ_i, while the corresponding off-diagonal elements (the coherences) $\rho_{ij}(t)$ decay with rates $\frac{1}{2}(\kappa_i + \kappa_j)$.

In the following we consider the time scales of relaxation in the dimer, which are defined as τ_{TR} (for the thermal relaxation as previously) and as τ_{rgs} for the relaxation to the ground state. As for the monomers, we assume that state $|a\rangle$ is a long-living excited state, and hence $\kappa_a = 0$. The short-living state $|b\rangle$ (lifetime τ_{Q}) decays with the rate $\kappa_b = \tau_{\mathrm{Q}}^{-1} \equiv \kappa$ and, thus, plays the role of the quencher. We will now present a simplified model to describe the long-time evolution in such a system.

We can describe the processes of relaxation within the dimer by the following *effective* Master equation in the excitonic basis:

$$\begin{cases} \dot{\rho}_{11} = - \quad (k_{12} + \kappa\cos^2\theta)\,\rho_{11} \;+\; k_{21}\,\rho_{22}; \\ \dot{\rho}_{22} = \quad k_{12}\,\rho_{11} \;-\; (k_{21} + \kappa\sin^2\theta)\,\rho_{22}. \end{cases} \tag{5.2}$$

Here, k_{12}, k_{21} are the *effective* transfer rates, in analogy to Eq. (2.40), that satisfy the detailed balance condition $k_{12}/k_{21} = \exp(-\beta\Delta_{\mathrm{e}}\varepsilon^0)$, where $\Delta_{\mathrm{e}}\varepsilon^0$ again denotes the energy gap between the relaxed excitonic states. If the reorganization energies are identical, $\Delta_{\mathrm{e}}\varepsilon^0$ coincides with the excitonic splitting $\Delta_{\mathrm{e}}\varepsilon = \sqrt{\Delta\varepsilon^2 + (2J)^2}$, as discussed in the previous chapter. We call Eq. (5.2) *effective* in the sense that the full quantum dissipative dynamics are parametrized by the *effective* rates, which can be extracted from some general equation of motion for the RDO in the absence of RGS (in the current case, the HEOM), by numerical fitting. The sine and cosine in Eq. (5.2) originate from the transformation matrix, Eq. (2.12), which is used to represent the RGS superoperator in the excitonic basis.

The solution of Eq. (5.2) is of the form $\rho_{ii}(t) = A_{i1}\mathrm{e}^{\xi_1 t} + A_{i2}\mathrm{e}^{\xi_2 t}$, where A_{i1}, A_{i2} are the amplitudes, and $\xi_{1;2}$ are the eigenvalues of Eq. (5.2). The latter read:

$$-|\xi_{1;2}| = -\frac{k_{12} + k_{21}}{2} - \frac{\kappa}{2} \pm \frac{1}{2}S, \tag{5.3}$$

where

$$S = \sqrt{(k_{12}+k_{21})^2 - \frac{2\kappa(k_{12}+k_{21})}{\sqrt{(2J/\Delta\varepsilon)^2+1}}\tanh\frac{\beta\Delta_e\varepsilon}{2} + \frac{\kappa^2}{(2J/\Delta\varepsilon)^2+1}}. \quad (5.4)$$

The eigenvalues correspond to the time scales of interest as $\tau_{\mathrm{rgs}} = |\xi_1|^{-1}$ and $\tau_{\mathrm{TR}} = |\xi_2|^{-1}$. Such attribution might look dubious as the origin of the net decay, described by $\xi_{1;2}$, is a mixture of both the exciton thermalization due to the interaction between the monomers and the presence of the quencher within the system. However, a closer inspection of the limiting case $\kappa \to 0$ reveals, that $|\xi_1| \to 0$ and $|\xi_2| \to k_{12}+k_{21}$, which is the classical result for the relaxation to the thermal equilibrium. More generally, when $k_{12}+k_{21} \gg \kappa$ (usually, thermalization is much faster than the spontaneous decay) we can simplify S as follows:

$$S \approx k_{12} + k_{21} - \kappa\Phi(J,\, \Delta\varepsilon), \quad (5.5)$$

where the auxiliary function Φ is defined as

$$\Phi(J,\, \Delta\varepsilon) = \tanh\left(\frac{\beta\Delta\varepsilon}{2}\sqrt{(2J/\Delta\varepsilon)^2+1}\right)/\sqrt{(2J/\Delta\varepsilon)^2+1}. \quad (5.6)$$

The eigenvalues now read:

$$|\xi_1| \approx \frac{\kappa}{2}\left(1+\Phi(J,\, \Delta\varepsilon)\right), \quad (5.7)$$

$$|\xi_2| \approx k_{12} + k_{21}. \quad (5.8)$$

This shows how the effect of the quencher emerges in the dynamics: the first eigenvalue corresponds purely to the RGS, while the second one still gives the rate of thermalization as if the spontaneous decay were absent. We can estimate the time scale for the RGS as:

$$\tau_{\mathrm{rgs}} = \frac{2\tau_{\mathrm{Q}}}{1+\Phi(J,\, \Delta\varepsilon)}. \quad (5.9)$$

Since $\Phi(J,\, \Delta\varepsilon) \in [-1;\, 1]$, RGS takes place on the time scale within the range $[\tau_{\mathrm{Q}};\, 2\tau_{\mathrm{Q}}]$ if the quenching state is below the donor state ($\Phi > 0$), and on the time scale $[2\tau_{\mathrm{Q}};\, \infty)$ otherwise ($\Phi < 0$). Of course, this relation becomes less accurate when $\Delta\varepsilon \gg k_{\mathrm{B}}T$ or the resonance and system–bath couplings are very small, because the condition $k_{12}+k_{21} \gg \kappa$ breaks, yet we

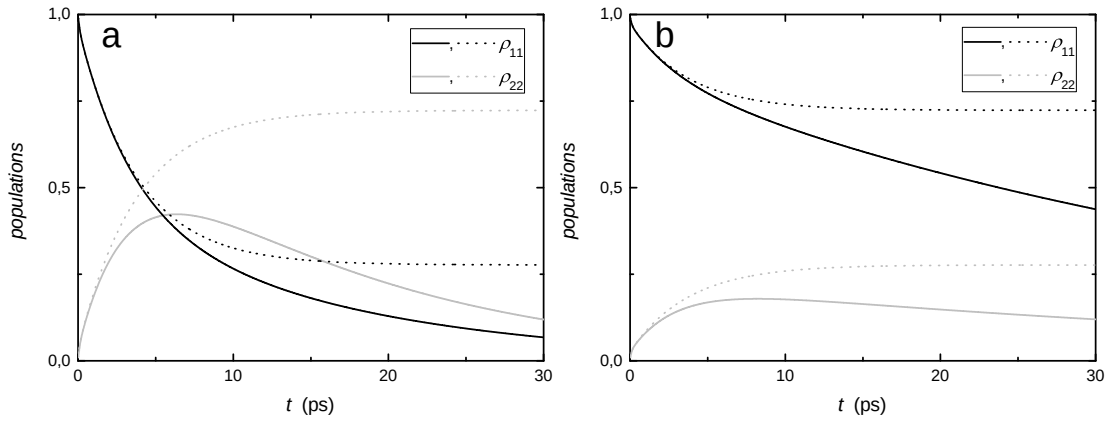

Figure 5.2 Relaxation in the dimer. The dotted lines correspond to thermal relaxation alone, while the full lines correspond to the combined process. The energy gap is: (a) $\Delta\varepsilon = +200\,\mathrm{cm}^{-1}$; (b) $\Delta\varepsilon = -200\,\mathrm{cm}^{-1}$. Temperature and reorganization energies are the same as in Fig. 4.4; $J = 20\,\mathrm{cm}^{-1}$, $\gamma^{-1} = 100\,\mathrm{fs}$.

can use Eq. (5.9) as a lower bound for τ_{rgs}. We will use this analytical result later in the analysis of the results obtained by the numerical simulations.

Let us now take the RGS into account by considering the excitation dynamics in the dimer while assuming $\tau_{\mathrm{Q}} = 10\,\mathrm{ps}$. Fig. 5.2 shows the excitation evolutions both in the presence (full lines) and in the absence (dotted lines) of the RGS in the cases of $\Delta\varepsilon = \pm 200\,\mathrm{cm}^{-1}$ ($J = 20\,\mathrm{cm}^{-1}$). As can be seen, the energetic position of the quencher has an effect on both the rates and the amplitudes of the process. The amplitude dependence largely comes from the unquenched dynamics. The latter gives us the time scale for TR alone as $k_{12} + k_{21} = 1/3.8\,\mathrm{ps}$. By performing a two-exponential fitting we obtain the following time scales for the combined process: (a) $\tau_{\mathrm{TR}} = 3.2\,\mathrm{ps}$, $\tau_{\mathrm{rgs}} = 15.6\,\mathrm{ps}$; (b) $\tau_{\mathrm{TR}} = 2.8\,\mathrm{ps}$, $\tau_{\mathrm{rgs}} = 46.2\,\mathrm{ps}$. Although the condition $k_{12} + k_{21} \gg \kappa$ is not very accurate in this situation, we still can check the time scale τ_{rgs} against the theoretical limit given by Eq. (5.9). For the current parameters it gives: (a) $\tau_{\mathrm{rgs}} = 13.8\,\mathrm{ps}$; (b) $\tau_{\mathrm{rgs}} = 36.1\,\mathrm{ps}$. As we can see, Eq. (5.9) gives the right tendency although the numerical value is appreciably different for $\Delta\varepsilon = -200\,\mathrm{cm}^{-1}$.

To demonstrate the net effect of the RGS and TR in the non-Markovian regime we calculate evolutions for the energy gaps $\Delta\varepsilon = -200\,\mathrm{cm}^{-1}$ and $\Delta\varepsilon = -650\,\mathrm{cm}^{-1}$, as shown in Fig. 5.3. Other parameters are the same as in Fig. 5.2, only the reorganization energies are such that $\lambda_a + \lambda_b = 1000\,\mathrm{cm}^{-1}$. The parameters are chosen to yield a rough fit of the signal decay time scales corresponding to dyads 2 and 3 from Ref. [35]. Energy gap $\Delta\varepsilon = -200\,\mathrm{cm}^{-1}$ (black line) corresponds to the time scales $\tau_{\mathrm{TR}} = 3.7\,\mathrm{ps}$, $\tau_{\mathrm{rgs}} = 49.9\,\mathrm{ps}$,

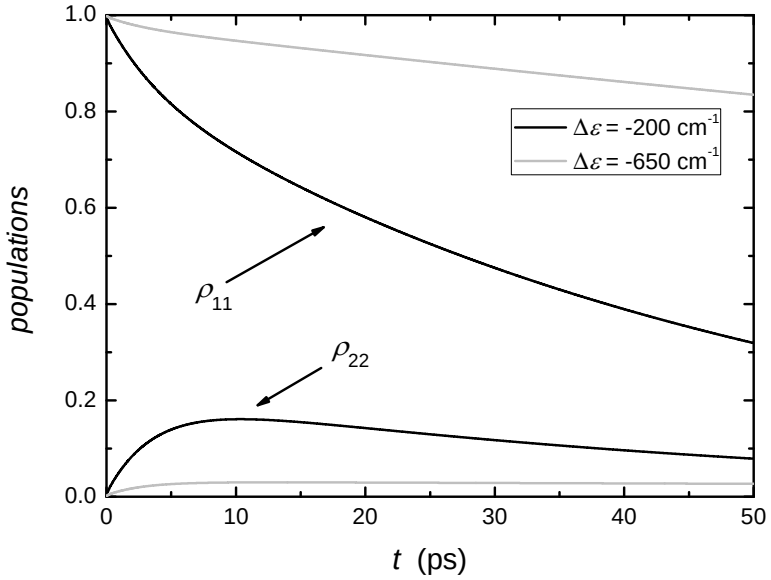

Figure 5.3 Relaxation in the dimer upon the increase of the energy gap. The black lines correspond to the smaller gap ($\Delta\varepsilon = -200\,\mathrm{cm}^{-1}$), the grey ones correspond to the larger gap ($\Delta\varepsilon = -650\,\mathrm{cm}^{-1}$).

whereas for the gap $\Delta\varepsilon = -650\,\mathrm{cm}^{-1}$ (grey line) we get $\tau_{\mathrm{TR}} = 2.7\,\mathrm{ps}$, $\tau_{\mathrm{rgs}} = 311\,\mathrm{ps}$. Note the decrease of the amplitude associated with the TR.

As follows from our analysis presented above, the two time scales of the evolution of the donor-quencher combined dimer have the following origin. One of the rates and the corresponding amplitude is largely determined by details of the relaxation to the thermal equilibrium in the absence of quenching, Fig. 5.2. While this rate is independent of the sign of $\Delta\varepsilon$, the amplitude indicates the sign due to thermodynamic reasoning as follows. State $|1\rangle$ being optically accessible is always initially over-populated with respect to the equilibrium, therefore $\rho_{11}(t)$ is always decreasing. Yet, the amplitude of the decrease is significantly larger for $\Delta\varepsilon > 0$ (state $|1\rangle$ is the upper state) than for $\Delta\varepsilon < 0$ (dark state $|2\rangle$ is the upper state). The second rate is determined by the quencher lifetime and its energy position. Interestingly, if the lifetime and the thermal relaxation time scale are well separated, the RGS time scale does not depend on the system-bath coupling, conf. Eq. (5.9), yet the asymmetry between the situations of $\Delta\varepsilon > 0$ and $\Delta\varepsilon < 0$ again arises from the thermodynamic groundings, conf. the hyperbolic tangent function in Eq. (5.6). In this case, the values of τ_{rgs} for various resonance couplings and energy gaps are shown in Fig. 5.4. We can see that when the excited state of the quencher is below the donor excited state ($\Delta\varepsilon > 0$), the relaxation time τ_{rgs} is less than twice the quencher lifetime and weakly depends on the resonance coupling and the absolute value

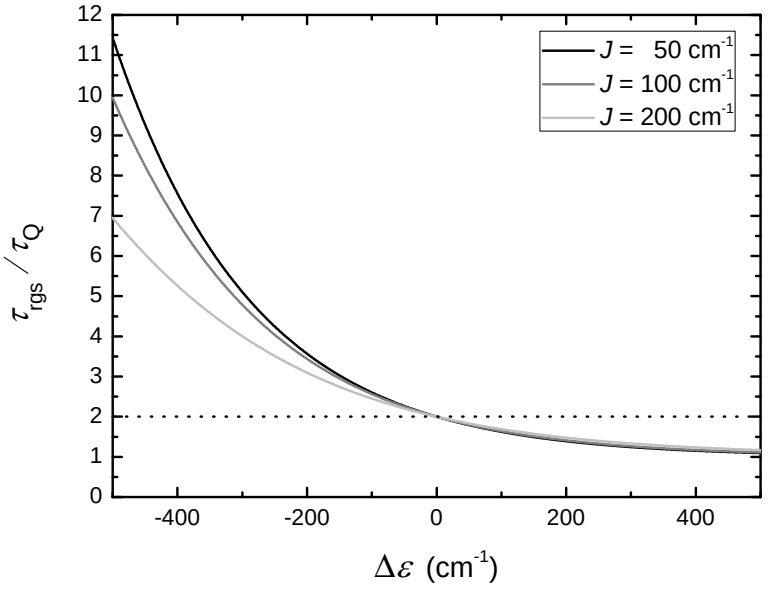

Figure 5.4 Time scale of the relaxation to the ground state τ_{rgs} as a function of the energy gap and the resonance coupling according to Eq. (5.9). The time scale is normalized to the lifetime of the quencher τ_{Q}.

of the energy gap. In the opposite case, $\tau_{\mathrm{rgs}} > 2\tau_{\mathrm{Q}}$ and the dependence on the energy gap is clearly pronounced.

5.3. Carbonyl-linked carotenoid–phthalocyanine dyads

The model of excitonically coupled dimer described above can be used for the analysis of the excitation kinetics in Car-Pc dyads, which consist of a zinc Pc covalently linked to a series of Cars with different number of carbon-carbon conjugated double bonds. The evolution of excitation within such systems has been recently traced by means of transient absorption spectroscopy [35, 37]. The experiments focused on determining the correlation between the lifetime of the Pc excited state and the number of conjugated double bonds within Car moiety. Berera et al. studied carbonyl-linked dyads [35] (the name comes from the terminal group of Car moiety), while Kloz et al. performed identical measurements on phenylamino-linked dyads [37]. After pumping the system into the Q_{y} absorption band of the Pc ($670 - 680\,\mathrm{nm}$), the decay of the Q_{y} signal (ground state bleach and stimulated emission) was observed both in the kinetic traces at the same wavelength and the evolution-associated decay spectra (EADS) obtained by the global analysis of the time-resolved data [82]. Several time components were needed for an adequate fit, however, we take into consideration only the two fastest ones since we find the rest to be in agreement with the in-

terpretation proposed by the authors. The values of the relevant time scales taken from the figures of the EADS in Refs. [35] and [37] are summarized accordingly in Tables 5.1 and 5.2.

We map the dyads onto our model assuming that a dimer is formed due to the coupling of the Car first excited state S_1 to the Pc Q_y state. Car S_1 is an optically dark state, moreover, it is an extremely short-lived state ($\tau_{S_1} \approx 5 - 10\,\mathrm{ps}$) due to the ultrafast internal conversion [71, 83]. Therefore Car S_1 corresponds to the state $|b\rangle$ from our generic model, and the long-lived ($\tau_{Q_y} \sim 3\,\mathrm{ns}$), bright state Q_y corresponds to the state $|a\rangle$. Upon these definitions the condition $\Delta\varepsilon^0 > 0$ corresponds to Q_y being above S_1. We note that ε_{S_1}, and hence $\Delta\varepsilon^0$, as of today is still a debated parameter [83], therefore we use $\Delta\varepsilon^0$ as an adjustable variable in our calculations.

Firstly, let us discuss the carbonyl-linked dyads in tetrahydrofuran (THF) [35]. The experimentally determined decay times for all these dyads are presented in Table 5.1. Starting with dyad 3 (11 double bonds) the first two time scales (3.8 ps and 56 ps) are of the order of correspondingly the energy transfer in weakly coupled molecular aggregates and the lifetime of the S_1 state. If we subsequently assume that these time scales correspond to the rates ξ_2 and ξ_1, Eq. (5.3), the following estimates are to be proposed. Since the longer time scale is more than twice the Car S_1 lifetime τ_{S_1} (which we approximated here and further as $\tau_{S_1} \equiv \tau_Q = 10\,\mathrm{ps}$), we can expect that the S_1 state is actually above the Q_y state. Next, by noting that the sum of the eigenvalues Eq. (5.3) yields $k_{12} + k_{21} = |\xi_1| + |\xi_2| - \kappa$, we can estimate the thermalization time scale to be $(k_{12} + k_{21})^{-1} \approx 5\,\mathrm{ps}$. This indicates that the transfer proceeds within the Förster regime, i.e. the resonance coupling is small ($J \ll \Delta\varepsilon$) and the reorganization energies are large ($\lambda \gg J$), which is plausible in the dyad, since the Car S_1 state, while being close to the Pc, optically carries no transition dipole. To obtain the set of parameters consistent with both time scales we have performed modelling by using the HEOM scheme with the RGS for certain ranges of J, λ and $\Delta\varepsilon$. The results are given in Fig. 5.3 (black line), and the determined parameters yield the time scales $\tau_{\mathrm{TR}} = 3.7\,\mathrm{ps}$, $\tau_{\mathrm{rgs}} = 49.9\,\mathrm{ps}$ when the relaxed Car S_1 is $200\,\mathrm{cm}^{-1}$ above the relaxed Pc Q_y. Such a slow thermalization requires not only a small resonance coupling ($J = 20\,\mathrm{cm}^{-1}$) but also considerably large reorganization energies: $\lambda_a + \lambda_b = 1000\,\mathrm{cm}^{-1}$. This might look surprising bearing in mind that the FWHM of the Q_y absorption, which is proportional to λ_{Q_y}, is roughly $400\,\mathrm{cm}^{-1}$ at most. However, we cannot assess λ_{S_1} in the same way, and the latter might make a significant contribution [84]. To make sure that the obtained time scales are not just coincidental, but are instead indicative

Table 5.1 Comparison of experimentally detected and theoretically obtained time scales for carbonyl-linked dyads in THF. DB denotes the number of conjugated double bonds of Car moiety; τ_{1st} denotes the fastest time scale shown in Fig. 2 from Ref. [35] and τ_{2nd} is the second fastest time scale.

	Experiment		Theory		
DB	τ_{1st} (ps)	τ_{2nd} (ps)	$\Delta\varepsilon^0$ (cm^{-1})	τ_{TR} (ps)	τ_{rgs} (ps)
9	1.25	3000	-1100	2.7	2700
10	$(1-8)^\star$	300	-650	2.7	311
11	3.8	56	-200	3.7	49.9

*these are two individual time scales in Ref. [35]; see text for details.

of a consistent physical mechanism, we varied the energy gap while keeping all the other parameters unchanged. We found that shifting the energy gap to $\Delta\varepsilon^0 = -650\,\mathrm{cm}^{-1}$ yields $\tau_{TR} = 2.7\,\mathrm{ps}$, $\tau_{rgs} = 311\,\mathrm{ps}$, Fig. 5.3 (grey line). The latter time scales are characteristic for dyad 2 (10 double bonds), although global analysis indicates three time scales: 1 ps, 8 ps and 300 ps. Here, we make an assumption that the actual rate most probably has the value between $(1\,\mathrm{ps})^{-1}$ and $(8\,\mathrm{ps})^{-1}$, because both processes have relatively small amplitudes. A further shift in energy, $\Delta\varepsilon^0 = -1100\,\mathrm{cm}^{-1}$, yields time scales $\tau_{TR} = 2.7\,\mathrm{ps}$, $\tau_{rgs} = 2.7\,\mathrm{ns}$, which resemble those of dyad 1 (9 double bonds): 1.25 ps, 3 ns. The time scale τ_{TR} almost coincides with the previous value due to approximate symmetry of the non-Markovian rate function $\tau_{TR}(\Delta\varepsilon)$. What is important, the value of τ_{rgs} illustrates the highly nonlinear dependence $\tau_{rgs}(\Delta\varepsilon)$ in the region of negative energy gaps, Fig. 5.4. These results are summarized in Table 5.1.

Before formulating the general conclusion from these findings we would like to note that in dyad 3, the rise at $> 550\,\mathrm{nm}$ on the 3.8 ps time scale has been previously attributed to the inverted kinetics behaviour. However, the rise of the mentioned component could in principle be due to the initial under-population (with respect to the equilibrium) of the optically dark state $|2\rangle$ as discussed above. In Fig. 5.3 we can see the initial rise of ρ_{22} on the time scale τ_{TR}, and the amplitude is decreasing upon the increase of $\Delta\varepsilon^0$, which correlates with the experimental observations. Therefore we can suggest that in the the carbonyl-linked dyads in THF, the Car S_1 state approaches Pc Q_y state from above upon increasing the conjugation length of the carotenoid from 9 double bonds (no significant quenching; S_1 state "too high") to 11 double bonds (S_1 state right above the Q_y state; significant quenching). The modelling presented here demonstrates how the so-called

Table 5.2 Comparison of experimentally detected and theoretically obtained time scales for phenylamino-linked dyads in toluene. Notation is the same as in Table 5.1; the experimental data is taken from Fig. 2 from Ref. [37]

	Experiment		Theory		
DB	τ_{1st} (ps)	τ_{2nd} (ps)	$\Delta\varepsilon^0$ (cm^{-1})	τ_{TR} (ps)	τ_{rgs} (ps)
10	0.4	67	-300	0.42	52
11	0.5	29	-150	0.53	31

"molecular gear shift mechanism" [85] could function in the presence of a small resonance coupling and *without* switching of the states due to addition of a single double bond.

5.4. Phenylamino-linked carotenoid–phthalocyanine dyads

Let us now consider the phenylamino-linked dyads in toluene and THF [37]. Since the evolutions have a strikingly different character depending on the solvent, we start with Dyad-10 and Dyad-11 (10 and 11 double bonds, accordingly) in toluene, and the corresponding decay times are presented in Table 5.2. Again, the first two time scales resemble those of thermalization and relaxation: 0.4 ps and 67 ps for Dyad-10, 0.5 ps and 29 ps for Dyad-11. The TR on the time scale of several hundreds of femtoseconds points to larger resonance coupling than previously. The RGS time scale suggests that the quenching state is again above the donor state. On the assumption that the dyads are similar to those of Ref. [35], we keep all parameters the same only setting the resonance coupling to $J = 80\,cm^{-1}$. Varying the energy gap we find that $\Delta\varepsilon^0 = -150\,cm^{-1}$ yields $\tau_{TR} = 530$ fs, $\tau_{rgs} = 31$ ps, and $\Delta\varepsilon^0 = -300\,cm^{-1}$ yields $\tau_{TR} = 420$ fs, $\tau_{rgs} = 52$ ps. The results are summarized in Table 5.2. Both the time scales and the amplitudes correlate with the observed Pc Q_y signal, except that experimentally no rising component in the excited state absorption of Car S_1 was detected. It has been suggested [37] that this could be due to excitonic mixing of the states which would instantaneously populate the state $|2\rangle$ as well as $|1\rangle$ and therefore only the decay would be observed. In our calculations this is not the case, because despite rather large J, the difference in reorganization energy $\Delta\lambda$ makes the energy gap $\Delta\varepsilon$ too broad to yield detectable excitonic mixing. This introduces a discrepancy between our model and the spectroscopic data, unless the Car S_1 contribution to the signal is overwhelmed by the decay of the components from other participating states.

The same dyads evolve on entirely different time scales in THF. The thermalization time scale $(k_{12} + k_{21})^{-1}$ varies from 8.7 ps to 5.6 ps (Dyads -8 to -11), which is again indicative of the Förster regime. Such a drastic drop in the transfer rates suggests that some other state than S_1 should be responsible for the quenching. Yet if we consider the lifetime of this quencher to be similar to the one of the Car S_1, we can notice, that $\tau_{\mathrm{rgs}} < 2\tau_{\mathrm{Q}}$, which means that the excitation energy of the quencher is now below the one of the donor. There are two more arguments that would support this hypothesis. Firstly, the decrease of the signal at 700 nm proceeds in two steps of comparable amplitudes (conf., Fig. 5.2(a)). Secondly, there is no significant energy gap dependence on τ_{rgs} (conf., Fig. 5.4). What weakens the hypothesis is the absence of a rising counterpart component in the spectra.

Our treatment thus leads to a unified picture of processes within a range of different dyads. As an important result we have demonstrated that a significant decrease in the quenching time for Pc in the dyads for longer Cars does not necessarily indicates that the Car S_1 state is below the Pc Q_{y}, although such an argument is sometimes given. At this point it is interesting to note that if our assignment of the rates ξ_1 and ξ_2 to the observed time scales is correct, the experiments on the dyads provide a direct proof of an energy gap dependent speed-up of the TR due to non-Markovian bath. We would like to note that by the modelling discussed above we did not intend to actually pinpoint the parameters yielding the experimentally detected time scales. For instance, we did not include the variation of τ_{Q} with the length of the Car backbone. At this stage we also do not consider whether the quenching state is actually the S_1 or S^*, or a charge transfer state. Instead, our goal was to provide insights into the evolution of the donor–quencher system, especially focusing on the role of the system–bath interaction which is usually neglected.

Calculations with different resonance couplings show that there is no significant difference in the quenching mechanism while changing from the incoherent energy transfer (Förster) regime to the coherent one. Although the excitations are localized in our current scheme due to large energy gap $\Delta\varepsilon$, in our previous work [81] we have taken into consideration a finite delocalization (as due to $\Delta\varepsilon = J$, $J \approx \lambda$). We have demonstrated therein that the excitation decays with a single rate because the joint system of excitonically mixed states is kept in a dynamical equilibrium. The time scale of the decay is governed by the same law, Eq. (5.9). This discloses a common misconception associated with the role of excitonic mixing in the quenching

of excitation energy. Namely, it has been implied that the efficient quenching might arise as a consequence of the excitonic mixing of lifetimes [86]. As can be seen, when the excitation decay is rigorously included into the quantum dissipative dynamics, Eq. (5.1), the rates $\kappa \cos^2\theta$ and $\kappa \sin^2\theta$ are *not* the true rates of the global energy dissipation. Instead, the exciton–phonon interaction leads to the Master equation of the type given by Eq. (5.2), thus the actual rate of the RGS is ξ_1, and $\xi_1 > \kappa \sin^2\theta$ for all $\Delta\varepsilon \neq 0$. Hence, from our unified perspective it does not seem that the quenching mechanisms termed as "energy transfer" and "excitonic coupling" [36, 37] would really be distinct from one another.

6. Summary of the results and conclusions

In the dissertation, the excitation energy transfer was studied in an excitonic dimer under various conditions of inter-chromophore resonance interaction and in different regimes of the system–bath coupling. In order to capture the coherence effects in the limit of weak resonance interaction a novel technique has been presented. While it is based on the perturbative expansion in terms of the resonance coupling in apparent similarity to the FRET theory, unlike in the FRET approach, we are able to reproduce the coherence effects in the simulation of both static and dynamic spectroscopic experiments. Namely, we can reproduce the excitonic splitting and dipole strength redistribution in the linear absorption and early TRF spectra, as well as the coherent oscillations in the evolution of the TRF spectra. The coherent component of the population evolution of the RDO can be reproduced at early times in a good agreement with the results from HEOM, which is a non-perturbative method. Thus, we are able to capture the excitonic effects while working in the base of the monomeric, i.e. localized, states. The drawback of the perturbative treatment of the resonance coupling is that the system is driven towards the equilibrium with respect to the monomeric states, and the overall dynamics is best described in short times, approximately as $J \cdot t \leq 1$.

The study of an excitonic heterodimer under various system–bath coupling conditions revealed both coherent and incoherent excitation evolutions. The dynamics in the case of the hetero-dimer are rich in non-trivial effects, several of which are distinguished. Perhaps the most prominent effect arising in the situation of different reorganization energies, in the case of strong excitonic mixing, is the swapping of the vibrationally relaxed excited state energy levels with respect to the monomeric counterparts. The novel results regarding the influence of the bath upon the system dynamics are the following. Firstly, in the case of non-Markovian bath correlations, there exists a non-zero optimal energy gap for the excitation energy transfer both in the weak and the intermediate resonance coupling regimes. Secondly, the bath acts upon the system reducing the energy gap that defined the thermal equilibrium. This effect is recognized as the formation of an "excitonic polaron", a state different than the conventional Frenkel exciton, and can be

quantitatively described by introducing an effective resonance coupling.

Lastly, the study of the relaxation of the excitonic dimer to the ground state revealed that the resonant coupling strength and the energy gap between the states — the parameters, which determine the excitonic mixing — only control the rate of the process but not the character. This demonstrates that there is no substantial difference in the relaxation mechanism in the coherent and incoherent regimes. By the same token, it is demonstrated that a short-lived state can efficiently quench the excitation within the dimer even if it is above the long-lived state. This finding helped us explain the dissipation mechanism and time scales in the artificial carotenoid–pthalocyanine dyads, and may be helpful in determining the mechanism(s) of the non-photochemical quenching in photosynthesis.

Bibliography

[1] A. Davydov, *A Theory of Molecular Excitions* (McGraw-Hill, New York, 1962).

[2] T. Kobayashi (ed.), *J-Aggregates* (World Scientific, Singapore, 1996).

[3] R. E. Blankenship, *Molecular Mechanisms of Photosynthesis* (Wiley-Blackwell, Oxford, UK, 2002).

[4] H. van Amerongen, L. Valkunas, R. van Grondelle, *Photosynthetic Excitons* (World Scientific, Singapore, 2000).

[5] T. Förster, Zwischenmolekulare energiewanderung und fluoreszenz, Ann. Phys. **437**, 55–75 (1948).

[6] M. Cho, H. M. Vaswani, T. Brixner, J. Stenger, G. R. Fleming, Exciton analysis in 2D electronic spectroscopy, J. Phys. Chem. B **109**, 10542–10556 (2005).

[7] T. Mančal, L. Valkunas, E. L. Read, G. S. Engel, T. R. Calhoun, G. R. Fleming, Electronic coherence transfer in photosynthetic complexes and its signatures in optical spectroscopy, Spectroscopy **22**, 199–211 (2008).

[8] M. Cho, *Two-Dimensional Optical Spectroscopy* (CRC Press, Boca Raton, 2009).

[9] L. Valkunas, D. Abramavicius, T. Mančal, *Molecular Excitation Dynamics and Relaxation* (Wiley-VCH, Weinheim, 2013).

[10] G. D. Scholes, G. R. Fleming, A. Olaya-Castro, R. van Grondelle, Nature Chem. **3**, 763–722 (2011).

[11] G. S. Schlau-Cohen, A. Ishizaki, G. R. Fleming, Two-dimensional electronic spectroscopy and photosynthesis: Fundamentals and applications to photosynthetic light-harvesting, Chem. Phys. **386**, 1–22 (2011).

[12] E. Harel, G. S. Engel, Quantum coherence spectroscopy reveals complex dynamics in bacterial light-harvesting complex 2 (LH2), Proc. Nat. Acad. Sci. USA **109**, 706–711 (2012).

[13] D. Zigmantas, E. L. Read, T. Mančal, T. Brixner, A. T. Gardiner, R. J. Cogdell, G. R. Fleming, Two-dimensional electronic spectroscopy of the B800-B820 light-harvesting complex, Proc. Nat. Acad. Sci. USA **103**, 12672–12677 (2006).

[14] G. S. Engel, T. R. Calhoun, E. L. Read, T. K. Ahn, T. Mančal, Y. C. Cheng, R. E. Blankenship, G. R. Fleming, Evidence for wavelike energy transfer through quantum coherence in photosynthetic systems, Nature **446**, 782–786 (2007).

[15] G. S. Schlau-Cohen, T. R. Calhoun, N. S. Ginsberg, E. L. Read, M. Ballottari, R. Bassi, R. van Grondelle, G. R. Fleming, Pathways of energy flow in LHCII from two-dimensional electronic spectroscopy, J. Phys. Chem. B **113**, 15352–15363 (2009).

[16] H. Lee, Y.-C. Cheng, G. R. Fleming, Coherence dynamics in photosynthesis: Protein protection of excitonic coherence, Science **316**, 1462–1465 (2007).

[17] E. Collini, G. D. Scholes, Coherent intrachain energy migration in a conjugated polymer at room temperature, Science **323**, 369–373 (2009).

[18] F. Milota, J. Sperling, A. Nemeth, H. Kauffmann, Two-dimensional electronic photon echoes of a double band J-aggregate: Quantum oscillatory motion versus exciton relaxation, Chem. Phys. **357**, 45–53 (2009).

[19] F. Caruso, A. W. Chin, A. Datta, S. F. Huelga, M. B. Plenio, Highly efficient energy excitation transfer in light harvesting complexes: the fundamental role of noise-assisted transport, J. Chem. Phys. **131**, 105106 (2009).

[20] P. Rebentrost, M. Mohseni, A. Aspuru-Guzik, Role of quantum coherence and environmental fluctuations in chromophoric energy transport, J. Phys. Chem. B **113**, 9942–9947 (2009).

[21] F. Fassioli, A. Nazir, A. Olaya-Castro, Quantum state tuning of energy transfer in a correlated environment, J. Phys. Chem. Lett. **1**, 2139–2143 (2010).

[22] P. Nalbach, J. Eckel, M. Thorwart, Quantum coherent biomolecular energy transfer with spatially correlated fluctuations, New. J. Phys. **12**, 065043 (2010).

[23] G. R. Fleming, S. F. Huelga, M. B. Plenio, Focus of quantum effects and noise in biomolecules, New. J. Phys. **12**, 065002 (2010).

[24] M. Sarovar, A. Ishizaki, G. R. Fleming, Quantum entanglement in photosynthetic light-harvesting complexes, Nat. Phys. **6**, 462 (2010).

[25] A. G. Redfield, On the theory of relaxation processes, IBM J. Res. Dev. **1**, 19–31 (1957).

[26] D. Abramavicius, L. Valkunas, S. Mukamel, Transport and correlated fluctuations in the nonlinear optical response of excitons, Europhys. Lett. **80**, 17005 (2007).

[27] P. Kjellberg, B. Brüggemann, T. Pullerits, Two-dimensional electronic spectroscopy of an excitonically coupled dimer, Phys. Rev. B **74**(2), 024303 (2006).

[28] A. V. Pisliakov, T. Mančal, G. R. Fleming, Two-dimensional optical three-pulse photon echo spectroscopy. ii. signatures of coherent electronic motion and exciton population transfer in dimer two-dimensional spectra, J. Chem. Phys. **124**, 234505 (2006).

[29] A. Ishizaki, G. R. Fleming, Unified treatment of quantum coherent and incoherent hopping dynamics in electronic energy transfer: Reduced hierarchy equation approach, J. Chem. Phys. **130**(23), 234111 (2009).

[30] A. Gelzinis, D. Abramavicius, L. Valkunas, Non-Markovian effects in time-resolved fluorescence spectrum of molecular aggregates: Tracing polaron formation, Phys. Rev. B **84**, 245430 (2011).

[31] M. Cho, G. R. Fleming, The Integrated Photon Echo and Solvation Dynamics. II. Peak Shifts and 2D Photon Echo of a Coupled Chromophore, J. Chem. Phys. **123**, 114506 (2005).

[32] D. Abramavicius, V. Butkus, J. Bujokas, L. Valkunas, Manipulation of two-dimensional spectra of excitonically coupled molecules by narrow-bandwidth laser pulses, Chem. Phys. **372**, 22–32 (2010).

[33] T. Renger, Theory of optical spectra involving charge transfer states: Dynamic localization predicts a temperature dependent optical band shift, Phys. Rev. Lett. **93**, 188101 (2004).

[34] T. Mančal, L. Valkunas, G. R. Fleming, Theory of exciton–charge transfer state coupled systems, Chem. Phys. Lett. **432**, 301–305 (2006).

[35] R. Berera, C. Herrero, I. H. M. van Stokkum, M. Vengris, G. Kodis, R. E. Palacios, H. van Amerogen, R. van Grondelle, D. Gust, T. A. Moore, A. L. Moore, J. T. M. Kennis, A simple artificial light-harvesting dyad as a model of excess energy dissipation in oxygenic photosynthesis, Proc. Nat. Acad. Sci. USA **103**, 5343–5348 (2006).

[36] P.-N. Liao, S. Pillai, D. Gust, T. A. Moore, A. L. Moore, P. J. Walla, Two-photon study on the electronic interactions between the first excited singlet states in carotenoid-tetrapyrrole dyads, J. Phys. Chem. A **115**, 4082–4091 (2011).

[37] M. Kloz, S. Pillai, G. Kodis, D. Gust, T. A. Moore, A. L. Moore, R. van Grondelle, J. T. M. Kennis, Carotenoid photoprotection in artificial photosynthetic antennas, J. Am. Chem. Soc. **133**, 7007–7015 (2011).

[38] D. Abramavicius, B. Palmieri, S. Mukamel, Extracting single and two-exciton couplings in photosynthetic complexes by coherent two-dimensional electronic spectra, Chem. Phys. **357**, 79–84 (2008).

[39] V. May, O. Kühn, *Charge and Energy Transfer in Molecular Systems* (Wiley-VCH Verlag GmbH, Weinheim, 2004).

[40] S. Mukamel, *Principles of Nonlinear Optical Spectroscopy* (Oxford University Press, New York, 1995).

[41] M. Wendling, T. Pullerits, M. A. Przyjalgowski, S. I. E. Vulto, T. J. Aartsma, R. van Grondelle, H. van Amerongen, Electron-vibrational coupling in the Fenna-Matthews-Olson complex of Prosthecochloris aestuarii determined by temperature-dependent absorption and fluorescence line-narrowing measurements, J. Phys. Chem. B **104**, 5825–5831 (2000).

[42] T. Renger, R. A. Marcus, On the relation of protein dynamics and exciton relaxation in pigment-protein complexes: an estimation of the spectral density and a theory for the calculation of optical spectra, J. Chem. Phys. **116**, 9997–10018 (2002).

[43] J. Adolphs, T. Renger, How proteins trigger excitation energy transfer in the FMO complex of green sulfur bacteria, Biophys. J. **91**, 2778–2797 (2006).

[44] V. Butkus, L. Valkunas, D. Abramavicius, Molecular vibrations-induced quantum beats in two-dimensional electronic spectroscopy, J. Chem. Phys. **137**(4), 044513 (2012).

[45] A. Ishizaki, Y. Tanimura, Quantum dynamics of system strongly coupled to low-temperature colored noise bath: Reduced hierarchy equations approach, J. Phys. Soc. Jpn. **74**, 3131–3134 (2005).

[46] Y. Tanimura, Stochastic Liouville, Langevin, Fokker–Planck, and Master equation approaches to quantum dissipative systems, J. Phys. Soc. Jpn. **75**(8), 082001 (2006).

[47] T. Mančal, J. V. Balevičius, L. Valkunas, Decoherence in weakly coupled excitonic complexes, J. Phys. Chem. A **115**, 3845–3858 (2011).

[48] J. Strumpfer, K. Schulten, Light Harvesting Complex II B850 excitation dynamics, J. Chem. Phys. **131**, 225101 (2009).

[49] Q. Shi, L. Chen, G. Nan, R.-X. Xu, Y. J. Yan, Efficient hierarchical Liouville space propagator to quantum dissipative dynamics, J. Chem. Phys. **130**, 084105 (2009).

[50] C. Kreisbeck, T. Kramer, M. Rodriguez, B. Hein, High-performance solution of hierarchical equations of motion for studying energy transfer in light-harvesting complexes, J. Chem. Theory Comput. **7**, 2166–2174 (2011).

[51] U. Weiss, *Quantum Dissipative Systems* (World Scientific, Singapore, 1999).

[52] J. Hu, R.-X. Xu, Y. J. Yan, Communication: Padé spectrum decomposition of Fermi function and Bose function, J. Chem. Phys. **133**, 101106 (2010).

[53] J. Hu, M. Luo, F. Jiang, R.-X. Xu, Y. J. Yan, Padé spectrum decompositions of quantum distribution functions and optimal hierarchical equations of motion construction for quantum open systems, J. Chem. Phys. **134**, 244106 (2011).

[54] V. Balevičius Jr., A. Gelzinis, D. Abramavicius, L. Valkunas, Excitation energy transfer and quenching in a heterodimer: Applications to the carotenoid–phthalocyanine dyads, J. Phys. Chem. B **117**, 11031–11041 (2013).

[55] R.-X. Xu, B.-L. Tian, J. Xu, Q. Shi, Y. Yan, Hierarchical quantum master equation with semiclassical Drude dissipation, J. Chem. Phys. **131**, 214111 (2009).

[56] R. X. Xu, P. Cui, X. Q. Li, Y. Mo, Y. J. Yan, Exact quantum master equation via the calculus on path integrals, J. Chem. Phys. **122**, 041103 (2005).

[57] R. T. Carter, J. R. Huber, Quantum beat spectroscopy in chemistry, Chem. Soc. Rev. **29**, 305–314 (2000).

[58] A. Ishizaki, G. R. Fleming, On the adequacy of the Redfield equation and related approaches to the study of quantum dynamics in electronic energy transfer, J. Chem. Phys. **130**(23), 234110 (2009).

[59] J. Olšina, T. Mančal, Electronic coherence dephasing in excitonic molecular complexes: Role of Markov and secular approximations, J. Mol. Model. **16**, 1765 (2010).

[60] M. Schlosshauer, *Decoherence and the Quantum-to-Classical Transition* (Springer-Verlag, Berlin, 2007).

[61] Y.-C. Cheng, G. R. Fleming, Coherence quantum beats in two-dimensional electronic spectroscopy, J. Phys. Chem. A **112**(18), 4254–4260 (2008).

[62] A. H. Romero, D. W. Brown, K. Lindenberg, Polaron effective mass, band distortion, and self-trapping in the holstein molecular-crystal model, Phys. Rev. B **59**(21), 13728–13740 (1999).

[63] M. Yang, G. R. Fleming, Influence of phonons on exciton transfer dynamics: Comparison of the Redfield, Förster, and modified Redfield equations, Chem. Phys. **275**, 355–372 (2002).

[64] S. Jang, Y. Jung, R. J. Silbey, Nonequilibrium generalization of Förster–Dexter theory for excitation energy transfer, Chem. Phys. **275**, 319–332 (2002).

[65] G. Lindblad, On the generator of quantum dynamical semigroups, Commun. Math. Phys. **48**, 119–130 (1976).

[66] B. Palmieri, D. Abramavicius, S. Mukamel, Lindblad equations for strongly coupled populations and coherences in photosynthetic complexes, J. Chem. Phys. **130**, 204512 (2009).

[67] D. Abramavicius, S. Mukamel, Quantum oscillatory exciton migration in photosynthetic reaction centers, J. Chem. Phys. **133**, 064510 (2010).

[68] J. Prior, A. W. Chin, S. F. Huelga, M. B. Plenio, Efficient simulation of strong system-environment interactions, Phys. Rev. Lett. **105**(050404) (2010).

[69] G. Ritschel, J. Roden, W. T. Strunz, A. Eisfeld, An efficient method to calculate excitation energy transfer in light-harvesting systems: application to the Fenna–Matthews–Olson complex, New J. Phys. **13**, 113034 (2011).

[70] A. V. Ruban, M. P. Johnson, C. D. Duffy, The photoprotective molecular switch in the Photosystem II antenna, Biochim. Biophys. Acta **1817**, 167–181 (2012).

[71] H. A. Frank, R. J. Cogdell, *Carotenoids in Photosynthesis* (Chapman & Hall, London, 1993).

[72] V. Barzda, M. Vengris, L. Valkunas, R. van Grondelle, H. van Amerongen, Generation of fluorescence quenchers from the triplet states of chlorophylls in the major light-harvesting complex II from green plants, Biochemistry **39**, 10468–10477 (2000).

[73] A. Dreuw, G. R. Fleming, M. Head-Gordon, Chlorophyll fluorescence quenching by xanthophylls, Phys. Chem. Chem. Phys. **5**, 3247–3256 (2003).

[74] N. E. Holt, D. Zigmantas, L. Valkunas, X.-P. Li, K. K. Niyogi, G. R. Fleming, Carotenoid cation formation and the regulation of photosynthetic light harvesting, Science **307**, 433–436 (2005).

[75] A. V. Ruban, R. Berera, C. Ilioaia, I. H. M. van Stokkum, J. T. M. Kennis, A. A. Pascal, H. van Amerongen, B. Robert, P. Horton, R. van Grondelle, Identification of a mechanism of photoprotective energy dissipation in higher plants, Nature **450**, 575–578 (2007).

[76] M. Wahadoszamen, R. Berera, A. M. Ara, E. Romero, R. van Grondelle, Identification of two emitting sites in the dissipative state of the major light harvesting antenna, Phys. Chem. Chem. Phys. **14**, 759–766 (2012).

[77] L. Valkunas, G. Trinkunas, J. Chmeliov, A. V. Ruban, Modeling of exciton quenching in Photosystem II, Phys. Chem. Chem. Phys. **11**, 7576–7584 (2009).

[78] S. S. Lampoura, V. Barzda, G. M. Owen, A. J. Hoff, H. van Amerongen, Aggregation of LHC II leads to a redistribution of the triplets over the central xanthophylls in LHC II, Biochemistry **41**, 9139–9144 (2002).

[79] S. Bode, C. C. Quentmeier, P.-N. Liao, N. Hafi, T. Barros, L. Wilk, F. Bittner, P. J. Walla, On the regulation of photosynthesis by excitonic interactions between carotenoids and chlorophylls, Proc. Nat. Acad. Sci. USA **106**, 12311–12316 (2009).

[80] P.-N. Liao, S. Bode, L. Wilk, N. Hafi, P. J. Walla, Correlation of electronic carotenoid-chlorophyll interactions and fluorescence quenching with the aggregation of native LHC II and chlorophyll deficient mutants, Chem. Phys. **373**, 50–55 (2010).

[81] V. Balevičius Jr., A. Gelzinis, D. Abramavicius, T. Mančal, L. Valkunas, Excitation dynamics and relaxation in a molecular heterodimer, Chem. Phys. **404**, 94–102 (2012).

[82] I. H. M. van Stokkum, D. S. Larsen, R. van Grondelle, Global and target analysis of time-resolved spectra, Biochim. Biophys. Acta **1657**, 82–104 (2004).

[83] T. Polívka, V. Sunström, Dark excited states of carotenoids: Consensus and controversy, Chem. Phys. Lett. **477**, 1–11 (2009).

[84] A. Dreuw, Influence of geometry relaxation on the energies of the S1 and S2 states of violaxanthin, zeaxanthin, and lutein, J. Phys. Chem. A **110**, 4592–4599 (2006).

[85] H. A. Frank, A. Cua, V. Chynwat, A. Young, D. Gosztola, M. R. Wasielewski, Photophysics of the carotenoids associated with the xanthophyll cycle in photosynthesis, Photosynth. Res. **41**, 389–395 (1994).

[86] H. van Amerongen, R. van Grondelle, Understanding the energy transfer function of LHCII, the major light-harvesting complex of green plants, J. Phys. Chem. B **105**, 604–617 (2001).